Instabilities in Reactive and Deformable Two Phase Media

Luiza Angheluta

Thesis submitted for the degree of Philosophiae Doctor
Department of Physics, University of Oslo, Norway
September, 2009

Series of dissertations submitted to the
Faculty of Mathematics and Natural Sciences, University of Oslo
No. 910

ISSN 1501-7710

Cover: Inger Sandved Anfinsen.
Printed in Norway: AiT e-dit AS, Oslo, 2009.

Produced in co-operation with Unipub AS.
The thesis is produced by Unipub AS merely in connection with the
thesis defence. Kindly direct all inquiries regarding the thesis to the copyright
holder or the unit which grants the doctorate.

Unipub AS is owned by
The University Foundation for Student Life (SiO)

Scientific advisors:
Prof. Joachim Mathiesen
Prof. Bjørn Jamtveit

Acknowledgments

This PhD project was completed at the Center of Excellence for Physics of Geological Processes from the University of Oslo, under the scientific guidance of Prof. Joachim Mathiesen and Prof. Bjørn Jamtveit.

First of all, Prof. Joachim Mathiesen is greatly acknowledged for his outstanding supervision and inspiring collaboration all the way during the PhD years. I have benefited greatly from his insights and theoretical expertise.

Many scientific discussions and interactions with colleagues at PGP have provided useful knowledge and insights into geological processes. I am grateful to Prof. Francois Renard for his collaboration and warm hospitality at the University of Grenoble. I am thankful to Espen Jettestuen for his substantial contribution with the implementation of the level set method. My thanks to Prof. Yuri Podladchikov for useful discussions and Prof. Torgeir Andersen for the geological field trip to Atløy, Sunnfjord. Prof. Mogens Jensen and Prof. Kim Sneppen have always welcomed me happily during my visits to the Niels Bohr Institute. I am grateful to Prof. Paul Meakin for helping us improve the readability of the manuscripts with his useful comments and suggestions. Among the PGP-colleagues, I am particularly grateful to Marta Adamuszek, Anders Nermoen and Simon De Villiers for cheering me up with their friendship, interesting discussions and outdoors activities.

Oslo Guitar Ensemble (OGE) conducted by Petter Richter has played an important part over the past two years since I have joined it, and hearby a heartfelt thanks to all the members for sharing their passion for music and classical guitar. Finally, but not the least, I am in debt to my family for their steady emotional support.

Oslo, September 2009

Luiza Angheluta

List of symbols used in the chapters

(x, y, z)	Cartesian coordinates
t	time
$\partial_x = \frac{\partial}{\partial x}$	partial derivative with respect to x
$\nabla = (\partial_x, \partial_y)$	gradient operator
$\Delta = \partial_x^2 + \partial_y^2$	Laplace operator
$\mathbf{v} = (\mathbf{v_x}, \mathbf{v_y}, \mathbf{v_z})$	velocity field
$p(x, y, z)$	pressure field
ρ	mass density
g	gravitational acceleration field
H	width of a Hele-Shaw cell
Ψ	Laplacian field in the Safmann-Taylor instability
μ	fluid viscosity
$h(x, t)$	interface undulation
$V^{(0)}$	velocity of a flat interface
ϵ	expansion parameter in the perturbation analysis
$h^{(1)}(x, t)$	first order term in the morphological perturbation
$h_k^{(1)}(t)$	Fourier coefficient of the perturbation
ω	growth rate
k	wavenumber
$\exp(ikx)$	Fourier mode
γ	surface tension
κ	interface curvature
$\mu[x, h(x)]$	chemical potential at a stressed surface
$\mathcal{F}$	Helmholtz free energy per unit volume
$\mathcal{V}$	molar volume

σ_{ij}	elastic stress components
ϵ_{ij}	elastic strain components
$\mathbf{u} = (\mathbf{u_x}, \mathbf{u_y})$	elastic displacement field
J	interface mass flux
V_n	normal interface velocity
$U(x, y)$	BiLaplace field
(n_x, n_y)	normal vector at an interface point
M	positive mobility coefficient
τ_0	constant shear stress
P_0	hydrostatic pressure
G	elastic shear modulus
E	Young's modulus
ν	Poisson's ratio
σ_∞	normal load at infinity
$\epsilon_{kk} = \sum_{k=x,y,z} \epsilon_{kk}$	trace of strain
$H_i(x, y)$	linear shape functions for triangular elements
N	$(2, 6)$-array with the shape functions
$\mathcal{D}$	$(3, 2)$-array with differentials operating on shape functions
D	$(3, 3)$-array with the elastic coefficient for in-plane stress
$B = \mathcal{D}N$	$3, 6$-array with the spacial derivatives of the shape functions
$\hat{u}$	displacement field at the nodes of the finite elements
$\hat{f}$	body force in the finite element
$\varphi(x, y, t)$	level set function
W	surface velocity of the level set
f	Helmoltz free energy per unit mole
σ^e	effective contact stress
c	concentration of the soluble component
T	temperature
$\phi(x, t)$	porosity field
μ	fluid bulk viscosity
$k(\phi)$	permeability
η	solid bulk viscosity
$\tau = z - Vt$	comoving coordinate

List of symbols used in the papers

Hereby, only the symbols which are additional to the previous list, or have a different meaning are listed.

Paper I

Γ	interface boundary
$\tilde{\mathcal{F}}$	interfacial free energy per unit area
σ_0	normal load at infinity

Paper II

$\phi(x, y, t)$	level set
e	specific internal energy
Q	reaction rate at the interface
s	specific entropy
Π_s	entropy production at the interface
K	mobility coefficient
W	normal velocity at the interface
$\mathcal{K}$	curvature
L	length of a 1D elastic bar
g	specific Gibbs energy at the stressed interface
$\mathcal{W}$	work done on the interface by the normal stress
$\varphi(z), \chi(x)$	Goursat's complex functions
$\psi(z) = \chi'(z)$	z-derivative of the $\chi(z)$ complex function
$\Phi(z), \Psi(z)$	perturbation fields to the Goursat's functions

Paper IV

$F(t)$	stochastic force field
ϵ^*	energy dissipation rate
$\Delta r(t)$	pair-distance between two advected particles at time t
ν	kinematic viscosity
f	random forcing in the shell models

Contents

1 Introduction **11**

2 Stability of moving interfaces **19**
2.1 Viscous fingering 20
2.2 Liquid-solid interface 23
2.2.1 Flat interface: Zero order 27
2.2.2 Perturbed interface: First order 28
2.2.3 Linear stability analysis 29
2.3 Solid-solid interface 31
2.3.1 Wet interface 31
2.3.2 Dry interface 33
2.3.3 First and second order phase transitions 37
2.3.4 Nonlinear regime 39
2.4 Discussions 46

3 Porosity evolution by pressure solution **49**
3.1 Pressure solution at the grain scale 49
3.2 Pressure solution in porous media 53
3.2.1 Mass balance 55
3.2.2 Momentum balance 56
3.3 Dimensional analysis 58
3.4 Linear stability analysis 59
3.5 Stationary traveling waves 61
3.6 Non-stationary porosity evolution 63

Appendices **74**

A Paper I **i**

B Paper II **iii**

C Paper III **v**

D Paper IV **vii**

Chapter 1

Introduction

Pattern formation in multiphase systems is a central subject in research on nonlinear dynamics. In geoscience, the interest has been sparked by the ubiquitous appearance of spectacular patterns on all scales in nature, ranging from molecular levels to the scale of the Earth. A common goal for research on pattern formation has been to illuminate the fundamental physical mechanisms and the coupling between them. Here we shall demonstrate in a few model systems how basic physical principles can explain complex morphologies observed in deformable and reactive materials.

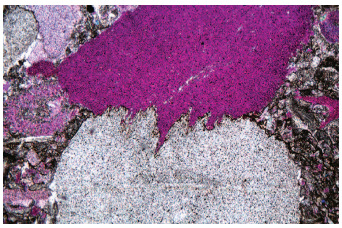

Figure 1.1: Grain-grain rough interface in a limestone from Mons, Belgium. Picture supplied by courtesy of Francois Renard.

The evolution of grains and grain surfaces is usually governed by stress or/and thermally activated physical processes. It involves mechanical deformation often coupled with chemical alteration e.g. surface growth by dissolution and precipitation. An aggregate of crystals may evolve by local recrystallization, where one crystal can grow at the expense of another in order to minimize the total (Gibbs) free energy. When identical crystals in contact have different crystallographic orientations, the one in the more energetically favorable state tends to grow at the expense of the other. This growth imposes a lattice preferred orientation of the individual grains and leads to a large scale anisotropy. It is common to observe such an anisotropy, for example in flowing ice [28] or in mineral

olivine in the Earth's upper mantle [15].

Surface instabilities triggered by evaporation and condensation in heated polycrystal were first analyzed in a seminal work on thermal grooving in [43]. Here we shall consider a similar instability in systems where mass is transported by surface diffusion along gradients of chemical potentials. In stressed systems, the surface diffusion is typically controlled by mass transported from regions of relatively high stress (high chemical potential) to regions of low stress (low chemical potential). This process corrodes the surface and gives rise to an instability which has been extensively studied and is also known as the Asaro-Tiller-Grinfeld instability [2, 25]. Often the mass transport is mediated by an interstitial fluid via dissolution in stressed regions and the subsequent precipitation at free sites, a process also known as 'pressure solution' [65, 61]. The phenomenon of sutured grain boundaries in sandstone [62] is one example where undulating surfaces are believed to be generated by pressure solution (see Fig. 1 for an example of grain-grain rough boundary). Stress-induced grooves due to ATG instability have been observed in laboratory experiments on salt crystals [13, 7] or on helium crystals [63]. In general, however, the effect of pressure solution on surface morphology can be very case dependent and other mechanisms may prevail, such as dislocation induced dynamics.

A fundamental problem in formulating a theory of large scale dynamics of rock deformation is to establish a link between large scale properties and the small scale structures, or how to make the transition from a discrete to a continuum formulation. In porous solids, such as sedimentary rocks, a continuum formulation is often based on a porosity field which represents the volume fraction of the rock occupied by fluids. The fluids are assumed to form a percolating and connected network and provide pathways for the migration of the dissolved material. On the large scale, the pressure solution is manifested in an effective viscous deformation mechanism by which the overall porosity decreases [1, 18, 54, 51].

In compacted sedimentary rocks intricate localized patterns are commonly observed. One ubiquitous example is stylolites, which appear as spontaneously generated seams formed perpendicular to the direction of compaction. The seams form a characteristic irregular surface with columnar or teeth like structures typically filled with a residual material such as clay (see Fig. 1). A morphological analysis of the stylolite surface has revealed a self-affine structure over at least two decades where small scale features reoccur on larger scales [56]. Despite intensive field studies on stylolites from the

micro to the meters scales, little is known about the detailed mechanisms controlling their formation. In fact only initial stages of stylolite formation have been reproduced in experiments, e.g. from indentation experiments [24]. Also from a modeling point of view there seems to be little consensus on the origin and roughening of the stylolites. In [17] it was argued that the dissolution surfaces nucleate from small heterogeneities or inclusions that grow in a direction normal to the compaction, i.e. they act as 'anti-cracks'. It has also been proposed, that the roughening is formed from local heterogeneities that are pinning an initially flat seam [32]. Other models suggest that clay may play an active role by enhancing the diffusion and transport along the chemical potential gradient [65].

In the subsequent sections, we shall here treat in detail several fundamental questions related to the topics outlined above. One question relates to the physical mechanism in the roughening of an interface in a stressed heterogenous solid, and, in particular, whether this alone could explain the columnar irregularities of stylolites. The other question is concerned with the formation of localized patterns in a porous material and whether these could emerge as a self-organization due to a nonlinear evolution of porosity.

The thesis comprises two chapters and four articles. The first chapter is intended as the groundwork for the first three appended articles. The second chapter elaborates on compaction by pressure solution and provides a one dimensional analysis for the evolution of porosity. The first steps made in this chapter are the basis for future work.

In the first chapter, we analyze several model setups of a moving interface separating two dissimilar phases, namely a liquid-liquid, liquid-solid and solid-solid interface. Analytical calculations for an infinitesimally perturbed interface are combined with numerical simulations in order to study the evolution of the interfacial morphology in the linear and nonlinear regimes respectively. The analytical part is formulated as a BiLaplacian growth problem, which can be solved for a linearly perturbed interface. To study the nonlinear growth regime, we developed a numerical scheme based on finite element methods coupled with a level set method for tracking the evolution of the interface.

The second chapter deals with reactive transport in porous materials and the local evolution in porosity. The reaction by pressure solution is localized at the grain-to-grain contacts and is manifested by the dissolution and transport along the grain contacts and precipitation at the pore walls, away from the contact. At the continuum scale, the pressure solution induces

a viscous rheological response to stress. In this study, we investigated the solitary solutions of the corresponding equation of porosity evolution.

In the first article, we study the evolution of a solid-solid coherent interface driven by a stressed-induced mass exchange between two solid phases. We show that for a coherent interface, which preserves the continuity of the displacement field and the stress vector, the normal propagation velocity is controlled by the jump in the Helmholtz free energy. In the limit where the interfacial thickness goes to zero (sharp limit), the interface develops a finger-like instability which propagates from the phase with higher Young's modulus (harder) into the phase with lower Young's modulus (softer). The fingers grow in the direction of the principal compaction direction unlike in the ATG instability.

The second article provides a detailed analysis of the setup presented in the first paper. Here we derived, from basic conservation laws and thermodynamics of irreversible processes, the governing equation of motion of a coherent interface. We arrived at an expression which related the normal velocity with the jump in the specific Gibbs energy. A linear stability analysis of small morphological perturbations revealed that the roughening of the interface depends on the Poisson's ratios or the degree of incompressibility of each phase. Typically, the interface propagates from the harder phase into the softer phase. However, when the mass densities in the unstressed state are the same and the Poisson's ratios sufficiently large, we found that the direction of propagation can be reversed.

The stability of fluid-solid contacts under both shear and normal loads has been studied in the third article. The fluid flow past an undulating solid surface induces a mass transport of diffusion along the surface from regions with higher chemical potential to regions with lower chemical potential. The shear flow has a stabilizing effect, whereas the hydrostatic pressure tends to destabilize the interface. In the presence of both shear and normal stresses, we found that the morphological stability depends on the Poisson's ratio. We applied this analysis to the stability of faults and established a relationship between the static friction coefficient and the Poisson's ratio, which remains to be tested by field observations.

On a seemingly different topic, the fourth article is about turbulence and superdiffusion of passively advected pair particles. The implicit linkage to the previously mentioned topics becomes more apparent on a larger frame where the inertial, nonlinear effects are added to an otherwise viscous flow. Many hard to solve problems are posed once the flow is dominated by non-

linear interactions across scales. Thus, the mainstream of turbulence studies are mainly applied to a homogenous single phase. Multiphase turbulent flow is to a large extent in its infancy. Broadly speaking, turbulence is a dynamical regime characterized by chaotic flow patterns and cascades across inertial scales. Classical turbulence is usually described by the Navier Stokes equation when the advection term dominates over the momentum diffusion term. The strength of the inertial advection versus the dissipative forces is measured by a dimensionless number called the Reynolds number, $Re = \frac{UL}{\nu}$, where U and L are characteristic velocity and length scales respectively and ν is the kinematic viscosity. As the Re number tends to infinity, the inertial motion becomes dominant over a wide range of scales above a dissipative lengthscale. Within the inertial range of a three dimensional turbulence, the energy is cascading from the large scale where it is injected all the way down to the dissipative molecular scale. The cascade is a self similar process and follows the Kolmogorov scaling [33], $\langle |v(x+r,t) - v(x)|^2 \rangle \sim \epsilon^{2/3} r^{2/3}$, where ϵ is the constant energy flux or the energy dissipation rate. In the Kolmogorov theory, the rate of energy being cascaded stepwise from one scale to the next one is kept constant and thus equal to the energy dissipation rate. In this case, the scaling of the statistical quantities, i.e. structure functions or correlation functions, can be deduced by dimensional analysis. However, the statistics for a turbulent flow is known to deviate from the Kolmogorov theory and this has to do with intermittent high amplitude bursts and long range correlations across scales. Two-dimensional turbulence has its own particularities because of the existence of a second quantity, namely enstrophy, which is cascaded downscale while the energy is transported in the opposite direction. One fundamental problem in turbulence is to determine the corrections to Kolmogorov scaling from the first principles, e.g. [39]. Particles advected by a turbulent flow follow chaotic trajectories [16]. The pair particles are known to follow the Richardson dispersion law [52], by which their relative distance scales with time as $\langle R^2 \rangle \sim \epsilon t^3$. In the article, we advanced the idea that random uncorrelated force fields can generate turbulence motion consistent with the classical Kolmogorov scaling and Richardson dispersion. Multiscaling and intermittency in the turbulent velocity have to do with the long range correlation and extreme events in the force field.

The thesis chapers are based on the papers and provide additional explanatory material. However, the notation used in the chapters is not entirely the same as the notation adopted in each paper. Therefore, a list of symbols is attached at the beginning of the thesis. The relation between chapters and

papers is emphasized in the table below.

Chapter sections	**Papers and sections**
2.2 Liquid-solid	III
2.2.1 Flat interface	III, sec. 3.2
2.2.2 Perturbed interface	III, sec. 3.3
2.2.3 Linear stability	III, sec. 3.4
2.3 Solid-solid	III, II, I
2.3.1 Wet interface	III, sec. 4
2.3.2 Dry interface	II, sec. II A
2.3.3 1st and 2nd order	II, sec. II, sec. III
2.3.4 Nonlinear regime	II, sec. IV, sec. V

a)

b)

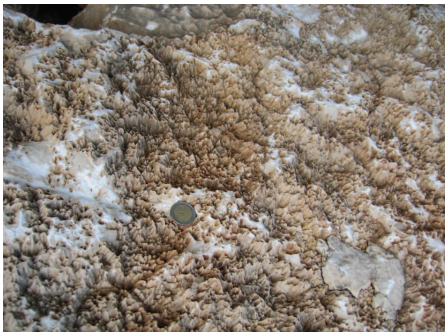

Figure 1.2: a) Sample of stylolite interface in sandstone in Spitsbergen, Svalbard. b) 3D view of a stylolitic surface in limestone in Northern Israel (coin for the scale). Pictures supplied by courtesy of Francois Renard.

Chapter 2

Stability of moving interfaces

Interfaces are transition regions over which material properties (densities, rheological properties, stress, velocity) undergo steep gradients. In the limit where their thickness is much smaller then the system size, one may idealize their internal structure and represent them as discontinuity surfaces or sharp interfaces. When the velocity or displacement field is continuous across a sharp interface, we say that the interface is material. In contrast, a non-material interface moves with a velocity which is different from the material velocity field, as in the case of a reactive surface. Interfaces are omnipresent in nature and their dynamics is intrinsically related to the large dynamics of multiphase materials.

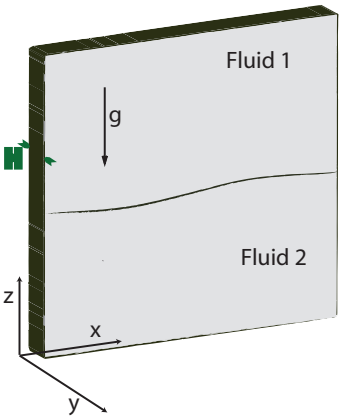

Figure 2.1: Sketch of the setup for Saffman-Taylor instability of a two-phase Hele-Shaw flow.

In this chapter, we shall present in details the stability analysis of various reactive sharp interfaces in two-phase systems. We find that the interfacial stability is related to material discontinuties, state of stress and its rheological response to stress (viscous, elastic).

We start by reviewing the classical analysis of viscous fingering, where the stability of a material interface depends on the direction of the flow

with respect to their relative density and viscosity. The subsequent sections are devoted to study the interfacial dynamics due to stress-induced mass transport. The linear stability analysis leads to a dispersion relation which determines the criteria for the development of rough surfaces. For a solid-solid interface, the onset of instability is validated in the finite amplitude regime by numerical simulations. The numerical modeling combines finite elements method for solving the bulk elastostatic equations with level set method for tracking the moving interface.

2.1 Viscous fingering

Morphological instabilities develop not only along reactive interfaces, but also material interfaces separating immiscible phases. The well-known example for this is the viscous fingering instability in multiphase fluids.

When two immiscible fluids are transported by a pressure gradient through a pipe, the stability of their interface depends on the direction of the flow. Namely, a less viscous fluid (like water) migrates into a more viscous fluid (like oil) by developing fingers which move ahead of the interface at various speeds. Contrarily, the interface remains planar when the water is ahead in the pipe and pushed by the oil. This instability is known as Saffman-Taylor instability [55] or viscous fingering and is typically developed in other setting as well where the interfacial dynamics is controlled by a Laplacian field, such as in diffusion limited aggregation (DLA) and dendritic growth [36].

The governing equations for an incompressible viscous flow are given by Stokes equations combined with the continuity equation,

$$\mu\nabla^2\mathbf{v} - \nabla(p+\rho g z) = 0 \tag{2.1}$$

$$\nabla^2(p+\rho g z) = 0, \tag{2.2}$$

where $\mathbf{v} = (v_x, v_y, v_z)$ is the velocity vector field. For incompressible fluids, mass conservation imposes that the velocity is a solenoidal field, $\nabla \cdot v = 0$. The fluid density is denoted by ρ assumed to be constant, and μ is the kinematic fluid viscosity. The gravitational field g is pointing downwards opposite with respect to the vertical z-axis. When the flow is confined between two parallel plates in the (x, z)-plane, the velocity in the y-direction vanishes (see Fig. 2). For a single phase flow, we can assume a homogenous flow in the x-direction and therefore obtain essentially an uniaxial flow in the z-direction with $v_z(y, t)$. The usual boundary conditions are given by the no-slip velocity

at the boundary with the plates, $v_z(0) = v_z(H) = 0$ and a constant pressure drop between inlet and outlet. The solution of the above equations for this setup is given by a quadratic profile across the y-axis, namely

$$v_z = -\frac{\partial(p + \rho g z)}{\partial z}\frac{1}{2\mu} y(y - H), \tag{2.3}$$

with constant pressure gradient. A linear flow law between the pressure drop and the mass flux, also known as Darcy's law, is obtained from the mean velocity, $Hv = \int_0^H v_z(y)dy$, and given as $v = \partial_z \Psi$ where $\Psi = -\frac{H^2}{12\mu}(p + \rho g z)$ is the potential field which satisfies the Laplace equation,

$$\nabla^2 \Psi(x, z) = 0. \tag{2.4}$$

As illustrated in Fig. 2, an interface between two viscous fluids extends along the x-axis and is situated at $z = z_I$. Fluid 1 occupies the upper half-plane with $z > z_I$ and fluid 2 is below at $z < z_I$. When the interface is flat, i.e. $z_I = 0$, the mean velocity v for each fluid is constant along the x-axis and equal to a uniform translation velocity $V^{(0)}$, where the upper index 0 refers to a flat interface. $V^{(0)}$ is positive when pointing upwards and negative otherwise. The interfacial velocity, however, may vary along an undulating interface. This is seen for instance when we consider a small undulation along the interface such as $z_I = h(x, t)$. Then the material velocity at the interface is $V^{(0)} + \partial_t h(x, t)$. The evolution of the interface is determined by solving the Laplace equation Eq. (2.4) for each domain and matching the two solutions through the interface boundary conditions given by the continuity of velocity field and pressure (in the absence of surface tension), namely

$$\left.\frac{\partial \Psi_j}{\partial z}\right|_{z=h} = V^{(0)} + \partial_t h \tag{2.5}$$

$$\frac{12\mu_1}{H^2}\Psi_1(x, h) + \rho_1 g h = \frac{12\mu_2}{H^2}\Psi_2(x, h) + \rho_2 g h, \tag{2.6}$$

where the lower index $j = 1, 2$ refers to the upper and lower fluid phases.

A simple solution can be obtained for a small morphological perturbations where $h(x, t) = \epsilon h^{(1)}(x, t)$ with $\epsilon \ll 1$ and $h^{(1)}$ is the morphological amplitude to linear order. In the linear regime, the potential fields can be expanded in terms of ϵ as $\Psi_j(x, z) = \Psi_j^{(0)}(x, z) + \epsilon \Psi_j^{(1)}(x, z)$, where $j = 1, 2$ is the fluid phase index, and the upper index 0 and 1 relates to

order of the expansion. For an infinite extension in the x-direction, the interfacial shape can be decomposed into a superposition of Fourier modes $h^{(1)}(x,t) = \int dk h_k(t) \exp(ikx)$, which may grow or decay at an exponential rate as $h_k(t) = \exp(\omega t)$. The growth rate ω, which may depend on the wavenumber k, determines the morphological stability of the interface.

The perturbed fields $\Psi_j^{(1)}(x,z)$ satisfing $\Delta\Psi_j^{(1)}(x,z) = 0$ admit a generic solution on the form

$$\Psi_j^{(1)}(x,z) = \int dk A_{j,k} \exp(\mp kz + ikx), \tag{2.7}$$

with an exponential decay at z-direction for each domain. The coefficients $A_{j,k}$ for $j = 1, 2$ are determined by the interfacial boundary conditions (see Eqs. (2.5)-(2.6)), which to a linear order become

$$\left.\frac{\partial \Psi_j^{(1)}}{\partial z}\right|_{z=0} = \omega h^{(1)} \tag{2.8}$$

$$\left[\frac{12\mu_1}{H^2}\Psi_1^{(1)} - \frac{12\mu_2}{H^2}\Psi_2^{(1)}\right]_{z=0} = \left[\frac{12(\mu_2-\mu_1)}{H^2}V^{(0)} + (\rho_2-\rho_1)g\right] h^{(1)} \tag{2.9}$$

Solving the above system using Eq. (2.7) and the Fourier transform of $h^{(1)}$, it follows that $A_{1,k} = -A_{2,k} = -\omega/k$, and

$$\frac{\omega}{k} = \frac{gH^2}{12}\frac{\rho_1-\rho_2}{\mu_1+\mu_2} + V^{(0)}\frac{\mu_1-\mu_2}{\mu_1+\mu_2}. \tag{2.10}$$

From the above relation, we see that the stability of the interface depends on the direction of the flow (by the sign of $V^{(0)}$), the relative density $\rho_1 - \rho_2$ and relative viscosity $\mu_1 - \mu_2$. The interface becomes unstable when the flow is under gravity with the denser fluid on the top of a lighter fluid or when the flow is upwards with a positive $V^{(0)}$ and the less viscous fluid at the bottom is migrating into the more viscous fluid above it. The growth rate is linearly proportional to the wavenumber, and therefore there is no mode selection, e.g. the interface is either stable or unstable at all lengthscales. In the presence of surface tension, there will be an additional term in the growth rate related to the curvature and surface tension. It can be shown that this term is stabilizing the interface perturbations with wavelengths smaller than a critical value equal to $2\pi H\sqrt{\gamma}[12V^{(0)}(\mu_1-\mu_2) + (\rho_1-\rho_2)gH^2]^{-1/2}$, with γ being the surface tension [55]. At finite morphological amplitude, the nonlinear interactions give rise to tip-splitting and side-branching instabilities [30],

in addition to the coarsening of fingers into a single dominant finger spanning the system size (e.g. [36]).

A similar perturbation analysis technique is applied to study the morphological instability of reactive interfaces where mass is being transported along or across the interface. When one phase is replaced by an elastic solid, the field equation in the corresponding domain is relapled by a BiLaplace equation.

2.2 Liquid-solid interface

Multiphase systems subjected to non-hydrostatic stresses often undergo morphological or structural changes. As the simplest multiphase system, we consider a two-phase body with an interface and a chemical component which is able to migrate between phases. The far-field applied stresses induce bulk deformations or creep and may activate interfacial processes such as chemical transport along a stress-dependent chemical potential gradient. It is known that ripples and grooves are developed along a liquid-solid interface, when the system is laterally compressed, such that the liquid is kept at rest and the solid deforms elastically [63, 19, 58, 29]. The interfacial instability, commonly referred to as Grinfeld or ATG instability [2, 25], is driven by surface gradients in a stress-dependent chemical potential. At an undulating interface, the material tends to dissolve in the troughs (from the solid side) with higher chemical potential, diffuse along the interface and precipitate on the crests with lower chemical potential. This positive feedback leads to surface roughening up to the scale where the stabilizing curvature effects become important. The theory of stress-induced chemical transport was developed similarly with that of thermal grooving [43] or solidification fronts due to thermal gradients as in Mullins-Sekerka instabil-

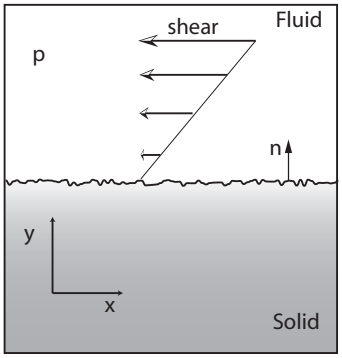

Figure 2.2: Illustration of a fluid-solid interface, when the fluid above is under uniform shear with the far field shear stress τ_0.

ity [44]. In stressed solids, surface diffusion may occur due to a gradient in the normal stress vector. The stability of a surface under stress corrosion was performed [25, 60] and found to be linearly unstable.

When a stressed solid is in contact with a saturated fluid, the chemical potential along the interface has the form [50, 58]

$$\mu[x, h(x)] = \mathcal{F}[x, h(x)]\mathcal{V} - \sigma_{nn}[x, h(x)]\mathcal{V}, \tag{2.11}$$

where $h(x)$ is the interface coordinate and $\mathcal{V}$ is the specific molar volume of the soluble component at the solid surface. The Helmholtz free energy per unit volume is denoted by $\mathcal{F}$. In this formulation, we assume that the elastic deformations as well as the interfacial mass transport occur at a constant temperature. The thermodynamics of linear elastic deformations in isothermal conditions is described by the Helmholtz free energy $\mathcal{F}$ equal to the elastic strain energy [35]

$$\mathcal{F} = \frac{1}{2}\sigma_{ij}\epsilon_{ij}, \tag{2.12}$$

with σ_{ij} being the elastic stresses are linearly related to the elastic strains ϵ_{ij} by the Hook's law. We treat the limit where the temperature effects can be decoupled from the mechanical and chemical effects. The normal stress vector at the interface is denoted by σ_{nn} relates to the interfacial traction on moving an atom along the interface. For a free surface $\sigma_{nn} = 0$, while if the surface is in contact with the fluid then $\sigma_{nn} = -p$, with p being the hydrostatic pressure in the fluid.

An explicit evaluation of the chemical potential involves the solution of the elasticity problem associated with a moving boundary. Namely, the interface is moving due to mass diffusion along its surface. The dynamical equation describing its motion is derived below.

The force acting on atoms along the interface is given as $-\partial\mu/\partial s$, where s is the interfacial arc length. Assuming a Fick's law, the atomic flux along the interface can be written as [43]

$$J = -\frac{D}{kT\mathcal{V}}\frac{\partial\mu}{\partial s}, \tag{2.13}$$

where $[D_s] = m^2 \cdot s^{-1}$ is the mass diffusivity involved in the surface diffusion process, $[kT] = Pa \cdot m^3$ is the thermal energy, $[\mathcal{V}] = m^3 \cdot mol^{-1}$ is the molar

volume. The conservation of mass requires a kinematic constraint such that the normal velocity of the interface is

$$V_n = -\mathcal{V}^2 a \frac{\partial J}{\partial s} = M \frac{\partial^2 \mu}{\partial s^2}, \tag{2.14}$$

where $[a] = mol \cdot m^{-2}$ is the surface density of atoms and $M = D_s a \mathcal{V}/kT$ is a positive mobility coefficients measured in units of $[M] = Pa^{-1}s^{-1}$.

Since mass diffusion is a slow processes, the interfacial velocity is much smaller than the speed of sound. Hence, it is reasonable to assume that, on the timescale of the interfacial process, the bulk phases are quasistatic. Hence, the solid phase is in elastostatics and satisfies

$$\nabla \cdot \sigma = 0, \tag{2.15}$$

where σ_{ij} are the tensorial elastic stress components. Hereby, the analysis will be carried out for two dimensional systems. In-plane elastostatics can be described by the Airy's stress field $U(x, y)$ which satisfies the biLaplace equation [45]

$$\frac{\partial^4 U}{\partial x^4} + 2\frac{\partial^4 U}{\partial x^2 \partial y^2} + \frac{\partial^4 U}{\partial y^4} = 0, \tag{2.16}$$

and from which the stresses are defined as

$$\sigma_{yy} = \frac{\partial^2 U}{\partial x^2}, \quad \sigma_{xx} = \frac{\partial^2 U}{\partial y^2}, \quad \sigma_{xy} = -\frac{\partial^2 U}{\partial x \partial y}. \tag{2.17}$$

The mechanical equilibrium translates into a set of two equations for stresses or displacements in x, respectively y direction, which are often harder to solve analytically. Representing the stresses in terms of a scalar field $U(x, y)$ makes the problem sometimes more tractable. The analytical solvability depends to a large extent on the boundary conditions and the geometry of the solid.

Linear stability analyses were carried out for free surfaces in [60] or for surfaces in contact with a hydrostatic fluid [19, 10]. The nonlinear morphological evolution leads to cusp-like singularities in finite time [68, 67]. When the solid phase is subjected to biaxial stress, where the applied stress is tensile in one direction and compressive in the other, there is a pattern selection from stripes to diamond-like morphology depending on the nonlinear interactions and the ratio between the compressive strength and the tensile strength [6, 49]. Previous analyzes considered the case of no shear forces present at the interface in the assumption that the fluid is at rest. We

hereby expand on the previous studies and consider a setup where we allow for shear forces at the fluid-solid interface due to fluid flow. The generic setup is sketched in Fig. 2.2 and its relevance to geological interfaces (such as fault planes, grain boundaries) is discussed in Paper III.

Hereby, the solid is in contact with a fluid which is able to flow due to a constant shear at infinity τ_0. We assume a Newtonian fluid with a linear viscous rheology, namely $\sigma_{ij}^{\text{fl}} = -p\delta_{ij} + \mu(\partial_i v_j + \partial_j v_i)$, where μ is the kinematic fluid viscosity, $p(x,y)$ is the fluid pressure, $v_x(x,y)$ and $v_y(x,y)$ are the horizontal, respectively vertical fluid velocities. At low Reynolds number, the fluid flow is dominated by the viscous effects and thus satisfies Stokes equations given as

$$\mu\left(\frac{\partial^2 v_x}{\partial x^2} + \frac{\partial^2 v_x}{\partial y^2}\right) = \frac{\partial p}{\partial x} \tag{2.18}$$

$$\mu\left(\frac{\partial^2 v_y}{\partial x^2} + \frac{\partial^2 v_y}{\partial y^2}\right) = \frac{\partial p}{\partial y} \tag{2.19}$$

$$\frac{\partial^2 p}{\partial x^2} + \frac{\partial^2 p}{\partial y^2} = 0. \tag{2.20}$$

The solution of the elastic deformations coupled with the viscous flow is determined by the conditions at the fluid-solid interface positioned at $h(x,t)$ and the far field boundary condition at $y = -\infty$.

At interface, we assume the continuity of the stress vector and the no-slip velocity (because the inertial effects in the solid are disregarded), namely

$$\sigma_{nn}(x,h) = -p(x,h) + 2\mu\frac{\partial v_n(x,h)}{\partial n} \tag{2.21}$$

$$\sigma_{nt}(x,h) = \mu\left[\frac{\partial v_t(x,h)}{\partial n} + \frac{\partial v_n(x,h)}{\partial t}\right] \tag{2.22}$$

$$v_n(x,h) = v_t(x,h) = 0, \tag{2.23}$$

where $(n_x, n_y) = (-\partial_x h, 1)/\sqrt{1+(\partial_x h)^2}$ and $(t_x, t_y) = (1, \partial_x h)/\sqrt{1+(\partial_x h)^2}$ are the normal, respectively the tangent vector at a point on the interface and h is a short hand notation for $h(x,t)$. Hereby, the normal vector points into the fluid phase.

The evolution of the elastic solid described by the BiLaplace equation requires two extra boundary conditions in addition to the force balance at the interface. Here, we consider that the solid phase is loaded at infinity as

$\sigma_{yy}(x,-\infty) = -P_0$ and $\sigma_{xx}(x,-\infty) = 0$. A more general treatment with a non-zero lateral compression is analyzed in Paper III.

The problem is solved using the perturbation technique in a similar manner as in the Saffman-Taylor instability, described in the previous section. That is, we treat the regime where the interface amplitudes are small enough, so that only the linear terms in the expansions are kept. We linearize the interface around a flat profile centered at the origin $h(x) = \epsilon h^{(1)}(x)$, where $\epsilon \ll 1$ is the expansion parameter and $h^{(1)}(x)$ is the local deviation from flatness. The upper index refers to the order of the expansion. In this limit the gradient along the interfacial arc length can be approximated by $\partial_s = [1 + \epsilon^2(\partial_x h^{(1)})^2]^{-1/2}\partial_x \sim \partial_x$. Also, the field variables are expanded around the reference state associated with a flat interface, namely

$$F(x,y) = F^{(0)}(x,y) + \epsilon F^{(1)}(x,y), \tag{2.24}$$

where $F(x,y)$ denotes any of the field variables $U(x,y)$, $p(x,y)$, $\mathbf{v}(x,y)$ and $F^{(1)}(x,y)$ is the contribution due to the interfacial morphological perturbation. For a point on the interface the fields are expanded as follows

$$F(x,\epsilon h^{(1)}) = F^{(0)}(x,0) + \epsilon\left[h^{(1)}\partial_y F^{(0)}(x,0) + F^{(1)}(x,0)\right]. \tag{2.25}$$

Thus, chemical potential at the perturbed surface takes the form

$$\mu(x,\epsilon h^{(1)}) = \mu^{(0)} + \epsilon\mu^{(1)}(x,0), \tag{2.26}$$

where the second term from the expansion disappeared because, in the reference state, $\mu^{(0)}$ is independent of the x-coordinate. The evolution of the interfacial perturbation is captured in the linearized version of Eq. (2.14), namely

$$\frac{\partial}{\partial t}h^{(1)}(x,t) = M\frac{\partial^2}{\partial x^2}\mu^{(1)}(x,0). \tag{2.27}$$

The absence of spacial gradients at a flat interface implies that the reference state is given by a stationary fluid-solid interface.

2.2.1 Flat interface: Zero order

To the zeroth order, the fluid flow is decoupled from the elastic deformations. The solution is, therefore, the same as for a shear flow past a planar wall,

namely

$$v_x^{(0)}(x,y) = \frac{\tau_0}{\mu} y \tag{2.28}$$

$$v_y^{(0)}(x,y) = 0 \tag{2.29}$$

$$p^{(0)}(x,y) = P_0. \tag{2.30}$$

The stress boundary conditions for the solid are therefore

$$\sigma_{yy}^{(0)}(x,0) = -P_0 \tag{2.31}$$

$$\sigma_{xy}^{(0)}(x,0) = \tau_0, \tag{2.32}$$

and the Airy's stress function satisfying these boundary conditions is given by

$$U^{(0)}(x,y) = -P_0 \frac{x^2}{2} - \tau_0 xy. \tag{2.33}$$

The reference state is given by a homogenous solution, where the elastic stresses are constant and equal to the boundary values.

2.2.2 Perturbed interface: First order

The stress at a perturbed interface is evaluated by an expansion around its value at a planar interface following Eq. (2.25), as

$$\sigma_{ij}(x, \epsilon h^{(1)}) = \sigma_{ij}^{(0)}(x,0) + \epsilon \sigma_{ij}^{(1)}(x,0). \tag{2.34}$$

The term dependent on surface gradients vanishes since the reference stresses are constant. Computing the normal stress vector using the zeroth order solution, we find that

$$\sigma_{nn}(x, \epsilon h^{(1)}) = -P_0 + \epsilon \left[-2\tau_0 \partial_x h^{(1)} + \sigma_{yy}^{(1)}(x,0) \right] \tag{2.35}$$

$$\sigma_{nt}(x, \epsilon h^{(1)}) = \tau_0 + \epsilon \left[-P_0 + \sigma_{xy}^{(1)}(x,0) \right]. \tag{2.36}$$

Similarly, the normal stress vector evaluated from the fluid phase becomes

$$\sigma_{nn}^{\mathrm{fl}}(x, \epsilon h^{(1)}) = -P_0(x,0) + \epsilon \left[-p^{(1)}(x,0) - 2\tau_0 \partial_x h^{(1)} + 2\mu \partial_y v_y^{(1)}(x,0) \right]$$

$$\sigma_{nt}^{\mathrm{fl}}(x, \epsilon h^{(1)}) = \tau_0 + \epsilon \left[\partial_x v_y^{(1)}(x,0) + \partial_y v_x^{(1)}(x,0) \right].$$

Inserting these perturbations into the interfacial conditions from Eqs. (2.21)-(2.23) and retaining the first order terms, we obtain the following relations

$$\begin{aligned}
\sigma_{yy}^{(1)}(x,0) &= -p^{(1)}(x,0) + 2\mu\partial_y v_y^{(1)}(x,0) && (2.37)\\
-\partial_x h^{(1)} P_0 + \sigma_{xy}^{(1)}(x,0) &= \mu\left[\partial_x v_y^{(1)}(x,0) + \partial_y v_x^{(1)}(x,0)\right] && (2.38)\\
v_y^{(1)}(x,0) &= 0 && (2.39)\\
v_x^{(1)}(x,0) + h^{(1)}\frac{\tau_0}{\mu} &= 0. && (2.40)
\end{aligned}$$

The perturbation fields satisfy Eq. (2.16) and Eqs. (2.18)-(2.20), combined with the above interfacial conditions. Assuming periodic boundary conditions in the x-direction or that the interface has an infinite extension, we can then use the Fourier analysis by decomposing the perturbation amplitudes as a superposition of Fourier modes, namely $h^{(1)}(x) = \int dk h_k^{(1)} \exp(ikx)$ and $F^{(1)}(x,y) = \int dk F_k^{(1)}(y)\exp(ikx)$. The problem can be solved in the Fourier space and has the following solution

$$\begin{aligned}
U_k^{(1)}(y) &= h_k\left(-P_0 + 2i\tau_0\right) y e^{ky} && (2.41)\\
p_k^{(1)}(y) &= 2ih_k\tau_0 k e^{-ky} && (2.42)\\
v_{x,k}^{(1)}(y) &= \frac{h_k\tau_0(ky-1)}{\mu}e^{-ky} && (2.43)\\
v_{y,k}^{(1)}(y) &= \frac{ikh_k\tau_0 y}{\mu}e^{-ky}. && (2.44)
\end{aligned}$$

The fields are computed in the real space by integrating up all the Fourier modes,

$$F(x,y) = F^{(0)}(x,y) + \epsilon\int dk F_k^{(1)}(y)\exp(ikx). \qquad (2.45)$$

2.2.3 Linear stability analysis

Recalling the definition of the surface chemical potential from Eq. (2.11) and retaining the first order term, we have that

$$\mu^{(1)}(x,0) = [\mathcal{F}^{(1)}(x,0) - \sigma_{nn}^{(1)}(x,0)]\mathcal{V}. \qquad (2.46)$$

The normal stress vector is calculated from the Airy's stress function given in Eq. (2.41) and projected to the interface with the normal vector $n \approx$

$(-\epsilon\partial_x h^{(1)}, 1)$. From Eq. (2.35), we have that the Fourier coefficient of the perturbed normal stress is given by

$$\sigma^{(1)}_{nn,k} = \sigma^{(1)}_{yy,k} - 2ikh_k\tau_0 = -2ik\tau_0 h_k. \tag{2.47}$$

Hereby, we consider the stability for in-plane strain elasticity, where the elastic energy density is defined as

$$\mathcal{F}(x,y) = \frac{1}{4G}\left[(1-\nu)(\sigma^2_{xx}+\sigma^2_{yy}) - 2\nu\sigma_{xx}\sigma_{yy} + 2\sigma^2_{xy}\right], \tag{2.48}$$

where G is the shear modulus and ν is the Poisson ratio. A similar analysis can be done in the in-plane stress assumption. Evaluating it at the interface and linearising the expression, we therefore obtain that

$$\mathcal{F}(x,\epsilon h) = \mathcal{F}^{(0)}(x,0) + \epsilon\mathcal{F}^{(1)}(x,0), \tag{2.49}$$

where,

$$\mathcal{F}^{(0)} = \frac{1}{4G}\left[(1-\nu)P_0^2 + 2\tau_0^2\right], \tag{2.50}$$

$$\mathcal{F}^{(1)} = \frac{1}{2G}\left\{[\nu\sigma^{(1)}_{xx} - (1-\nu)\sigma^{(1)}_{yy}]P_0 + 2\tau_0\sigma^{(1)}_{xy}\right\}. \tag{2.51}$$

The energy perturbation is decomposed into Fourier modes as the other field variables, $\mathcal{F}^{(1)}(x,0) = \int dk\mathcal{F}^{(1)}_k \exp(ikx)$. Using the expressions for the stress perturbations calculated from the Airy's stress function from Eq. (2.41) and Eq. (2.17), we obtain that

$$\mathcal{F}^{(1)}_k = \alpha k h_k, \tag{2.52}$$

where $\alpha = [i(1+2\nu)\tau_0 P_0 - P_0^2\nu + 2\tau_0^2]/G$.

Now, inserting the expressions for normal stress and elastic energy density into chemical potential and using Eq. (2.27) for the evolution of the interface, we arrive at

$$\int dk \frac{\partial h_k}{\partial t}\exp(ikx) = -M\mathcal{V}\int dk(\alpha - 2i\tau_0)k^3\exp(ikx). \tag{2.53}$$

For an exponentially growing mode $h_k = exp(\omega t)$, the above expression yields a dispersion relation given by

$$\omega = -M\mathcal{V}(\alpha - 2i\tau)k^3. \tag{2.54}$$

The linear stability is determined by the sign of the real part in the growth rate which, using the definition of α, is given by

$$\Re(\omega) = M\mathcal{V}(\nu P_0^2 - 2\tau_0^2)k^3. \qquad (2.55)$$

We notice that the interface becomes unstable if the following inequality between stresses is satisfied

$$\frac{\tau_0}{P_0} < \sqrt{\frac{\nu}{2}}. \qquad (2.56)$$

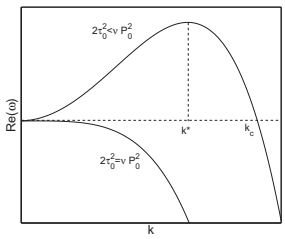

Figure 2.3: The growth rate as a function of the perturbation wavenumber k when curvature effects are considered. The curvature effect restricts the unstable domain to a finite value of wavenumbers with a maximum growth at $k^* = 27/128 \cdot k_c^3(\nu P_o^2 - 2\tau_0^2)$.

The linear stability thus depends on the competition between the magnitude of the shear stress τ_0 and the hydrostatic pressure P_0. Namely, the interface is linearly unstable if the pressure/normal load P_0 dominates over the shear stress and stable otherwise. So far, the interfacial energy or curvature has not appeared into the equations. Generally, the interfacial structure has a stabilizing role on the morphological evolution. In Paper III, we also include the effect of an isotropic surface tension and advance a discussion on the dependence of the friction coefficient at the onset of slip on the Poisson's ratio with its implications to geological interfaces. In Fig. 2.2.3, we show the dependence of the growth rate on the wavenumber, the the surface tension effect is taken into account.

2.3 Solid-solid interface

2.3.1 Wet interface

The stability of a thin fluid film between two elastic half-planes can be obtained using the previous analysis for a solid-liquid interface. When the fluid is at rest, we can take the limit of a fluid film thickness going to zero. In this limit, the presence of fluid is required only through the interfacial condition that the normal stress from both sides equals the fluid pressure p. Let

us assume for simplicity that the two elastic parts have the same material properties.

If the interface was a material surface, it would sustain shear stresses and would not be visible in a homogenous solid. However, we assume that, at the interface, the fluid film is at rest and therefore the shear stresses must vanish. The interfacial conditions translate into the continuity of the stress vector, with the normal component being equal to the hydrostatic pressure and the tangential component set to zero, namely

$$\sigma_{nn,j} = -P_0 \quad (2.57)$$
$$\sigma_{nt,j} = 0, \quad (2.58)$$

for each phase denoted by the lower index $j = 1, 2$ (see Fig. 2.3.1). In this case, we need to solve the BiLaplace equation in each domain and match the solutions through the above interfacial boundary conditions. Like in the previous analysis, we emply a perturbation scheme to first order and Fourier transform the linear term. The solution to the Fourier modes of the Airy's stress function perturbations are given as

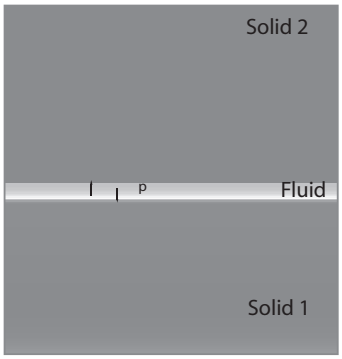

Figure 2.4: Illustration of a solid-fluid-solid interface, when the thickness of the fluid film is much smaller than the system size. The fluid is at rest with hydrostatic pressure p acting upon each solid boundary.

$$U^{(1)}_{1,k}(y) = -h_k P_0 y e^{ky} \quad (2.59)$$
$$U^{(1)}_{2,k}(y) = h_k P_0 y e^{-ky}, \quad (2.60)$$

and the corresponding stress components follow directly by using Eq. (2.17). The elastic energy density at the interface becomes equal to

$$\mathcal{F}(x, \epsilon h) = \frac{1-\nu}{4G} P_0^2 - \epsilon \frac{\nu}{G} P_0^2 \int dk h^{(1)}_k k \exp(ikx). \quad (2.61)$$

From Eq. (2.47), we see that the normal stress perturbation vanishes to linear order when the shear stress is set to zero, thus the chemical potential at the interface is determined by the elastic energy contribution. For an

exponentially growing mode at a rate ω, the dispersion relation is therefore given by

$$\omega = \frac{\nu}{G} k^3 M \mathcal{V} P_0^2, \tag{2.62}$$

which suggests that all modes are linearly unstable up to a cutoff introduced by surface tension effect. A similar setup with finite size elastic parts has been studied recently in [8], where the minimum energy criteria and the variational calculus for shape perturbations were employed to show that the interface is linearly unstable.

2.3.2 Dry interface

In this section, we discuss the kinetics of stress-induced phase transformations at a dry solid-solid interface. The two solid phases may have different mass densities ρ and elastic properties (ν, G). We consider the limit where the values of the material properties are discontinuous across the phase boundary. This discontinuity surface defines the sharp interface. We subject the system to a far field compression load $\sigma_\infty < 0$ transversal to the interface as sketched in Fig. 2.3.2. This brings the two stressed solids out of equilibrium with each other. Due to a mismatch in the material properties, the solids deform differently to the applied stress, such that one solid is in a higher energy state than the other. As a relaxation to equilibrium, the metastable solid phase tends to transform into the stable solid phase. We consider the particular case where no third phase is nucleated. Consequently, the interface is a phase transformation front which moves into the unstable solid at a nomal speed which can be determined from the reaction kinetics at the interface. A thermodynamical derivation for the normal growth is proposed in Paper II, where we assume entropy production at the interface and linear response regime with thermodynamic fluxes being proportional to thermodynamic forces. The driving force of phase transformation kinetics is given by the jump in the chemical potential at the interface and the mass flux is related to the normal velocity. Thus, we have that the interfacial velocity is given by

$$V_n = M \left[\!\!\left[\frac{\mathcal{F}}{\rho} - \frac{\sigma_{nn}}{\rho} \right]\!\!\right], \tag{2.63}$$

where $M > 0$ is a positive defined mobility coefficient. Here we introduce the jump in a quantity a from one phase to another $[\![a]\!] := a_1 - a_2$, where a_j is the evaluated from phase $j = 1, 2$ in the limit of approaching the

interface. We allow for volumetric changes in the mass densities due to elastic deformation. Thus, the mass density in the deformed state is related to the mass density in the referential state by $\rho \approx \rho_0/(1+\epsilon_{kk})$, where ϵ_{kk} is the trace of the strain equal to the relative volume change. For in-plane stress, $\epsilon_{kk} = \frac{1-2\nu}{2G(1+\nu)}(\sigma_{xx}+\sigma_{yy})$. Inserting this expansion into Eq. (2.63), we obtain an equivalent expression given by

$$V_n = M\left[\!\!\left[\frac{\mathcal{F}}{\rho_0} - \frac{\sigma_{nn}}{\rho_0}\left(1+\frac{1-2\nu}{2G(1+\nu)}(\sigma_{xx}+\sigma_{yy})\right)\right]\!\!\right]. \tag{2.64}$$

Similar to the diffusive transport at a liquid-solid interface, the interfacial kinetics can be explicitly evaluated by solving the corresponding elastic problem. This translates into finding the Airy's stress functions $U_j(x,y)$ as solutions to the BiLaplace equation in the corresponding solid phase $j=1,2$. The solutions are then matched at the interface from the continuity of the stress vector and displacement field expressed as

$$[\![n\cdot\sigma]\!] = 0, \qquad [\![\mathbf{u}]\!] = 0, \tag{2.65}$$

where $\mathbf{u} = (u_x, u_y)$ is the elastic displacement field related to the strain by $\epsilon_{ij} = 1/2(\partial_i u_j + \partial_j u_i)$. The Helmholtz free energy per unit volume $\mathcal{F}$, and the normal stress σ_{nn}, are calculated directly from the Airy's stress functions $U_j(x,y)$ using Eq. (2.17).

In Paper II, we solve the two-phase elasticity problem for in-plane stress, but the same tehnique works also for in-plane strain approximation. The Airy stress function is obtained using Goursat's formalism [45], where the BiLaplace equation in the complex plane, $z = x+iy$, has a generic solution given as $U(z,\overline{z}) = \Re\{\overline{z}\phi(z)+\chi(z)\}$ where $\overline{z} = x-iy$. The two complex fields $\phi(z)$ and $\chi(z)$ are defined in each phase domain and determined from the far field and interfacial conditions [1]. The same morphological perturbation technique as for a liquid-solid system is employed here. The calculation is presented in the Appendix of Paper II.

The reference solution corresponds to a flat interface moving with a uniform translational velocity given by

$$V^{(0)} = M\left[\!\!\left[\frac{|\sigma_\infty|}{\rho_0} - \frac{|\sigma_\infty|^2}{4}\frac{1-3\nu}{\rho_0 G}\right]\!\!\right]. \tag{2.66}$$

[1] In the appendix of Paper II, there is a misprint below Eq. (B_2). The new field $\psi(z)$ is defined as $\psi(z) = \chi'(z)$.

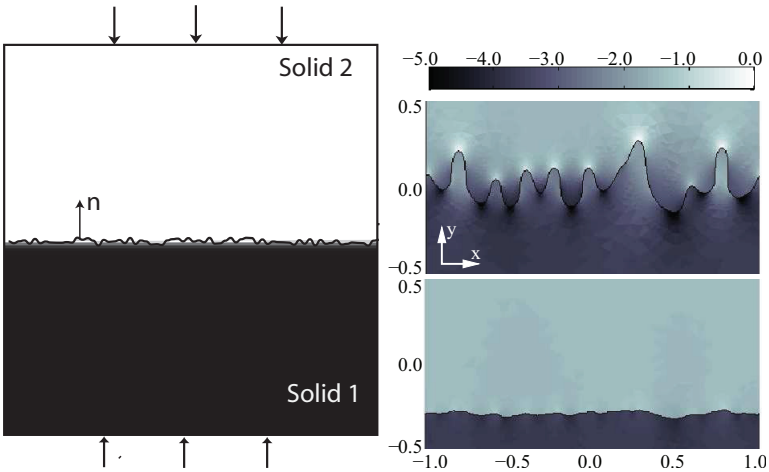

Figure 2.5: (Right) Illustration of a solid-solid interface with continuous stress vector and displacement field. The system is under normal far-field stress. (Left) Numerical simulations of the interfacial evolution in the regime of finite size amplitudes. The bottom figure shows the initial interface with a random perturbation and the top figure depicts an evolving interface. In both figures we have plotted the elastic energy density in logarithmic scale. The lighter color corresponds to a higher elastic energy density and that is localized at the peaks of the interface on the softer side.

The direction of propagation depends on the jump in the material properties, in a similar way as in the Saffman-Taylor instability of viscous fingering. When the referential densities are different, the above expression is dominated by the first term and predicts that the phase transformation is directed from the denser phase into the lighter phase. In the case where the referential densities are the same $\rho_{0,1} = \rho_{0,2}$, the second term becomes the leading order and, for $\nu < 1/3$, it gives a reverse propagation from the softer phase (higher G) into the harder phase (lower G).

The stress field around an undulating interface is calculated by following the perturbation scheme proposed in [20]. We consider a cosine perturbation of the interface as $h(x,t) = \epsilon h^{(1)}(t)\cos(kx)$ with $\epsilon \ll 1$, wavenumber k and an exponentially growing mode $h^{(1)}(t) = \exp(\omega t)$ where ω is the growth rate.

To the first order expansion, the Airy's stress functions can be written as a superposition of the reference solution (flat interface) and a small correction due to surface undulation, $U_j(x,y) = U_j^{(0)}(x,y) + \epsilon U_j^{(1)}(x,y)$ for each phase $j = 1, 2$. The perturbation fields $U_j^{(1)}(x,y)$ decay to zero away from the interface and are determined from the interfacial conditions Eq. (2.65). For a wavenumber k much smaller than the cutoff introduced by the surface tension, the solution of the perturbation can be expressed as

$$\begin{aligned} U_1^{(1)}(x,y) &= \frac{-|\sigma_\infty| h^{(1)}(\alpha_1 y + \beta)}{k(G_2\kappa_1 + G_1)(G_1\kappa_2 + G_2)} e^{-ky}\cos(kx) \\ U_2^{(2)}(x,y) &= \frac{|\sigma_\infty| h^{(1)}(\alpha_2 y - \beta)}{k(G_2\kappa_1 + G_1)(G_1\kappa_2 + G_2)} e^{ky}\cos(kx) \end{aligned} \tag{2.67}$$

where $\kappa_j = \frac{3-\nu_j}{1+\nu_j}$ and the material specific constants defined as [2]

$$\begin{aligned} \alpha_1 &= -k(1-\nu_1)(G_2 - G_1)(G_1\kappa_2 + G_1) \\ \alpha_2 &= k(1-\nu_1)(G_1 - G_2)(G_2\kappa_1 + G_1) \end{aligned}$$

and

$$\beta = 2G_1^2\frac{1-\nu_2}{1+\nu_2} - 2G_2^2\frac{1-\nu_1}{1+\nu_1} + 4G_1G_2\frac{\nu_1 - \nu_2}{(1+\nu_2)(1+\nu_1)}.$$

From the Airy stress functions, we calculate the stress components and evaluate the elatic energy density at the interface. By expanding to linear order in Eq. (2.64), and using an exponential growing mode $h^{(1)} = \exp(\omega t)$, we obtain a linear dispersion relation given as follow

$$\omega h^{(1)} = M\left[\!\!\left[\frac{\mathcal{F}^{(1)}}{\rho_0} - \frac{\sigma_{yy}^{(1)}}{\rho_0}\left(1 + \frac{1-2\nu}{2G(1+\nu)}\sigma_\infty\right) - \frac{\sigma_\infty}{\rho_0}\frac{1-2\nu}{2G(1+\nu)}(\sigma_{yy}^{(1)} + \sigma_{xx}^{(1)})\right]\!\!\right].$$

The growth rate is a function of the six material parameters (ν_j, μ_j, ρ_j) with $j = 1, 2$ and the external stress σ_∞. However, the stability of the growing interface is invariant under the interchange of the solid phases, thus the controlling parameters for stability are reduced. To further simplify the expression, we normalized the stress at infinity as $\sigma_\infty = -1$ in arbitrary units and have the shear modulus measured in the units of it.

[2] In Paper II, there is a misprint in the equation defining α_1, namely that there is a minus sign missing. This has been correct in the thesis.

2.3.3 First and second order phase transitions

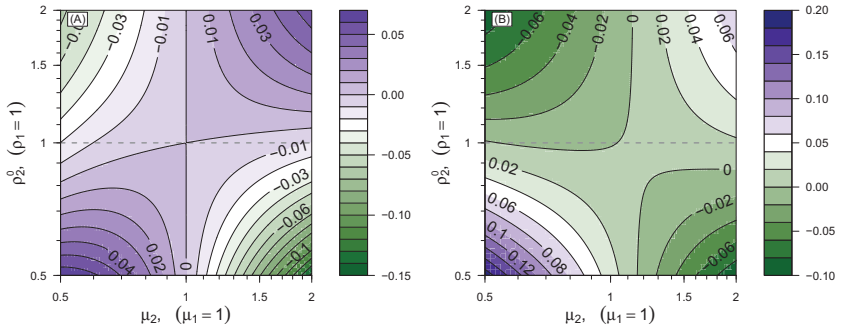

Figure 2.6: Panel (A), stability diagram for two solids materials with identical Poisson's ratio of $\nu = 0.25$. Panel (B), diagram for solids with Poisson's ratios of $\nu_1 = 0.45$ and $\nu_2 = 0.40$.

Whenever the system is stressed, only one of the two phases will be stable, i.e. the two phase system will evolve to a global equilibrium state consisting of a single phase. In the absence of stress it is possible for two phases to coexist without any phase transformation taking place at their interface. In Paper II, we propose an analog 1d model, where the specific Gibbs energy relates to the stress applied to the system σ by

$$g(\sigma) = \frac{\sigma^2}{2E\rho_0} - \frac{\sigma}{\rho_0}\left(1 + \frac{\sigma}{E}\right), \tag{2.68}$$

where E is the Young's modulus. Hereby we adopt the Ehrenfest classification of the phase transitions, namely that the nth order phase transition has a finite discontinuity in the nth derivative of the free energy with respect to any of its arguments at the critical point[3]. We define a first order phase transformation process when the first derivative of the specific Gibbs energy with respect to σ is discontinuous at $\sigma = 0$. From the above relation, we see

[3]Note that the Ehrenfest classification of the phase transitions assumes that the singularities at the critical point are only discontinuities. In general, this is not true in continuous phase transitions where the second order derivative of the free energy, e.g. specific heat, diverges at the critical point [23].

that this happens when the two phases have different referential mass densities. By a second order phase transition, we mean that the first derivative exists at $\sigma = 0$ and that there is a finite jump in the second order derivative, which is related to the discontinuity of the Young modulus, E. We adopt the same terminology for the interfacial phase transformation in two dimensions.

For second order phase transition where both solids have the same referential densities $\rho_{0,1} = \rho_{0,2} = \rho_0$. When the Poisson's ratios $\nu_1 = \nu_2 = \nu$ are identical, the dispersion relation assumes a simple form given by

$$\frac{\omega}{kM} = \frac{(3\nu - 1)(1 - \nu)(G_1 + G_2)(G_2 - G_1)^2}{\rho_0 G_1 G_2 (G_1 + G_2\kappa)(G_2 + G_1\kappa)(1 + \nu)} \tag{2.69}$$

where κ is the fraction introduced above and k the wavenumber of the perturbation. The expression reveals an interesting behavior where the interface is stable for Poisson's ratio less than 1/3 and is unstable for Poisson's ratio larger than 1/3. Fig. 2.6 shows stability diagrams for the specific case where $G_1 = 1$ and $\rho_{0,1} = 1$ (in arbitrary units). In panel (A) the diagram is calculated for two solids that have the same Poisson's ratio and with a value $\nu = 1/4$. The second order phase transition occurs along the horizontal cut $\rho_{0,2} = 1$ and is marked by a dashed grey line. We observe that ω/k is negative along this line and the interface is therefore stable. For ν larger than 1/3 (not shown in the figure) the horizontal zero level curve will flip around and the grey dashed line will then be covered with unstable regions. In order to see this flip, we expand Eq. (2.3.2) around the point (1,1), i.e. in terms of $\rho_{0,2} - 1$ and $G_2 - 1$, and achieve the following expression for the zero curve

$$\rho_{0,2} \approx 1 + \frac{(1 - 2\nu - 3\nu^2)(G_2 - 1)}{\nu(7 + \nu)}. \tag{2.70}$$

Note that the right hand side is in units of $\rho_{0,1}$. We directly observe that the horizontal zero curve flips around at the critical point $\nu = 1/3$. In the case when the two solids are identical, i.e. at the point (1,1) in the stability diagram, all modes will as expected remain unchanged and the interface therefore remains unaltered. The other parts of the zero levels lead to marginal stability but will in general induce a motion of the interface with a constant velocity.

We now consider a cut in the stability diagram where the two solids have the same shear modules, $G_1 = G_2 = G$, but different densities (first order phase transition) and Poisson's ratios. For different Poisson's ratios

the dispersion relation Eq. (2.3.2) becomes

$$\frac{\omega}{Mk} = \frac{(\nu_2 - \nu_1)(\nu_1\rho_{0,2} - \nu_2\rho_{0,1} + 2(\rho_{0,2} - \rho_{0,1})G)}{4\rho_{0,1}\rho_{0,2}G}. \tag{2.71}$$

From this expression we see that the vertical zero line observed in Eq. (2.69) and in Fig. 2.6 panel (A) only exists for identical Poisson's ratios. When the solids have different Poisson's ratios, the separatrix or intersection of the two zero curves located at (1,1) in panel (A) will split into two non-intersecting zero curves. In panel (B) we show a stability diagram for solids with Poisson's ratios $\nu_1 = 0.45$ and $\nu_2 = 0.40$.

In general the stability diagram is characterized by four quadrants, two stable and two unstable, delimited by neutral zero curves. The physical regions would typically correspond to the quadrants I and III under the assumption that higher density implies higher shear modulus. In these quadrants the growth rate is typically positive (i.e. the interface is unstable) except for a thin region at the borderline between a first and second order phase transition, i.e. when $\rho_2 \simeq \rho_1$.

2.3.4 Nonlinear regime

Linear stability theory is able to predict the critical values of the parameters for the onset of instability, such that an infinitesimal perturbation of a certain wavelength will initially grow exponentially in time. Fig. 2.6 shows the stable versus unstable domains in the parameter space predicted from the linear stability analysis. We find that the morphological stability of a flat interface depends non-trivially on the jumps in the material properties of the solids.

From the dispersion relation in Eq. (2.71), we can infer about a preferred wavelength selection by searching for the critical wavelength with the maximum growth rate. In the absence of surface tension, the growth rate is linearly proportional with the wavenumber, thus there is no k-dependent maximum growth, i.e. no wavelength selection in the linear regime. This is not surprising since the interfacial dynamics is driven by the stresses determined in the linear elasticity theory where there is no intrinsic lengthscale. However, a finite surface tension brings a quadratic k-dependence of the growth rate. The lengthscale at which the elastic contribution balances the surface tension is related to any selected wavelength in the dynamics.

To investigate the interfacial dynamics beyond the instability threshold, the nonlinear effects need to be included. There are in fact two approaches.

One way is to determine the nature of bifurcation, signaled by the change in the stability of the planar front, by studying the stability in the weakly nonlinear regime where the next order terms in the perturbation expansion are taken into account. This type of analysis has been carried out in the finite amplitude regime of a liquid-solid interface dynamics driven by mass diffusion due to stress gradients (ATG instability) [48], or temperature gradients (MS instability) [44, 10]. It is known that up to the third order expansion, the ATG bifurcation is subcritical [48], whereas the MS bifurcation changes from a subcritical to a supercritical branching depending on the front velocity and the mobility coefficient [66]. The fact that the bifurcation is subcritical implies that the interface can be unstable at finite amplitude undulations when the linear theory predicts stability to infinitesimal perturbations. This is closely related to cusp-like singularities developed at finite amplitudes in the ATG instability [48, 68] and dendritic growth and cellular structures in the directional solidification [41, 10].

The alternative approach is to solve the problem numerically without any prior expansions. In this work, we have adopted this later approach by employing numerical methods to explore the validity of the linear stability for finite size amplitudes. That is, we select a point in the parameter space which is predicted to be either linearly stable or unstable. For this particular configuration we integrate numerically the interfacial dynamics and follow the evolution of the interface into its nonlinear regime. We find that the linearly stable domains in the parameter space are also stable in the nonlinear regime, whereas in the linearly unstable domains, the interface evolves into finger-like patterns.

Numerical approach

The moving boundary problem is solved numerically in two stages at each time step. At time t, each phase occupies a domain delimited by the fixed outer boundaries and the moving interface. First, we compute the stress components in each phase domain by solving the elastostatic equations. Then, we advance the interface from t to $t + dt$ with a normal velocity, which is determined by the jump in the chemical potential. Thus, at time $t + dt$, the solid phases occupy slightly different domains, and, consequently, the stress is differently distributed. This would affect the normal velocity for the next time step.

The domain occupied by each solid phase is discretized into a set of trian-

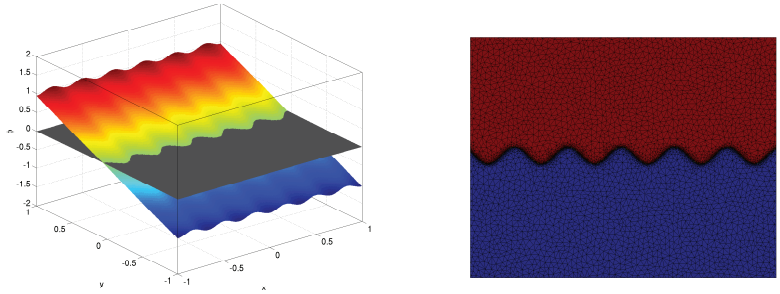

Figure 2.7: (Left) Level set function $\varphi(x, y, t)$ for tracking an interface with periodic undulations. (Right) A triangularization of the 2D domain with an unstructured grid.

gular elements of variable sizes and orientations, which form the underlying unstructured grid. This type of meshing is particularly helpful for a good representation of irregular boundaries. To improve the accuracy of the interface shape, we use a local grid refinement on a thin band surrounding it. The triangularization is performed using an open source routine, called "triangle.c" [4]. An illustration of the triangular meshing is shown in Fig. 2.7 (Right). The domain is remeshed after each time step in the dynamics of the interface.

We solve the elastic problem by using the Galerkin finite element method (see for e.g. [34]). Our finite elements are triangles characterized by linear shape functions, $H_i(x, y)$ and $i = 1, \ldots 3$ nodes. The shape functions represent a set of basis functions in which the field variables are decomposed. Namely, the displacement field is decomposed into

$$u_x(x, y) = \sum_{i=1}^{3} H_i(x, y) a_i \tag{2.72}$$

$$u_y(x, y) = \sum_{i=1}^{3} H_i(x, y) b_i, \tag{2.73}$$

where a_i and b_i correspond to discrete displacements at the nodes of a tri-

[4]The source file can be downloaded from http://www.cs.cmu.edu/ quake/triangle.html

angular element. The two degrees of freedom per node can be collected into a $(6,1)$-vector as $\hat{u} = [a_1, b_1, a_2, b_2, a_3, b_3]^T$, which stores the values of the displacements at the nodes of a triangle. In a matrix formulation, it is convenient to arrange the shape functions into a $(2,6)$-array as

$$N = \begin{bmatrix} H_1 & 0 & H_2 & 0 & H_3 & 0 \\ 0 & H_1 & 0 & H_2 & 0 & H_3 \end{bmatrix}, \tag{2.74}$$

and define a $(3,2)$-differential operator $\mathcal{D}$ as

$$\mathcal{D}^T = \begin{bmatrix} \frac{\partial}{\partial x} & 0 & \frac{\partial}{\partial y} \\ 0 & \frac{\partial}{\partial y} & \frac{\partial}{\partial x} \end{bmatrix}. \tag{2.75}$$

For the in-plane stress, the strains and stresses are denoted as

$$\sigma = [\sigma_{xx}, \sigma_{yy}, \sigma_{xy}]^T \tag{2.76}$$
$$e = [\epsilon_{xx}, \epsilon_{yy}, 2\epsilon_{xy}]^T, \tag{2.77}$$

and $\epsilon_{zz} = -\frac{\nu}{2G(1+\nu)}(\sigma_{xx} + \sigma_{yy})$. The Hooke's law relating them, can then be expressed as $\sigma = De$, where D is a $(3,3)$-matrix given by

$$D = \frac{2G}{1-\nu} \begin{bmatrix} 1 & \nu & 0 \\ \nu & 1 & 0 \\ 0 & 0 & \frac{1-\nu}{2} \end{bmatrix}. \tag{2.78}$$

The strains can be computed from the nodal displacement variables as $e = B\hat{u}$, where B is a $(3,6)$-array obtained by differentiating the shape functions, namely $B = \mathcal{D}N$. Thus, the stresses can also be determined from the nodal displacement vectors as $\sigma = DB\hat{u}$. The weak formulation of the elastostatic equation, $\nabla \cdot \sigma = 0$, reduces to the following matrix equation [34],

$$\left[\int_V B^T D B d\Omega\right] \hat{u} = \oint_{\partial V} N \hat{f} d\Gamma, \tag{2.79}$$

where $d\Omega$ is the area element, V is the volume of the integration domain and dl is the line element for the contour surface ∂V. The boundary conditions are incoded as body forces acting on the inner or outer boundaries, thus defining the rhs of the above equation. On the horizontal outer boundaries parallel to the interface we apply a constant normal force, thus $\hat{f}_{2i} = \sigma_\infty$, for $i = 1 \ldots 3$. The surface tension acting along the interface is converted into a

body force in a narrow band surrounding the interface [9]. Thus, for elements within the band, $\hat{f}_{2i-1} = \gamma\kappa n_x$, $\hat{f}_{2i} = \gamma\kappa n_y$, where $i = 1 \dots 3$, γ is the isotropic surface tension and κ is the local curvature of the interface obtained from the mean curvature of the level set, presented below. We impose lateral periodic boundary conditions to minimize the possible influence of the finite system size in the x-direction. The solution of Eq. (2.79) gives us the displacement vector at the nodes of each element. From that, we can then evaluate the stresses and strains everywhere in the domain. The discontinuous jumps appearing in the normal interfacial velocity are computed at the outer border of the band. The next step is to propagate the interface with a normal velocity that depends on the normal stress vector and elastic energy jump.

Various front tracking methods have been developed to solving specific moving boundary problems. One of the difficulties in having a universal solver for moving interfaces is the topological changes, i.e. merging or breaking of surfaces. Another troublesome issue is how to properly resolve the internal structure of a diffuse interface and its singular limit when it becomes sharp. Dendritic growth and solidification problems have been studied numerically using phase-fields methods for the propagation of diffuse interfaces (e.g. [31]). Phase field modeling has also been applied to stress induced instabilities and surface diffusion at liquid-solid interfaces [29], [69]. These methods are able to resolve the topological changes of interfaces with a small finite thickness. However they become more troublesome in the limit of a sharp interface, where an asymptotic analysis is required to match the phase-field equations with the sharp-interface equations [31]. The level set method is a computational approach which is able to handle both the topological changes as well as the propagation of sharp interfaces [59]. It is conceptually similar with the phase-field models in that the interface is represented as the zero level of a function $\varphi(x, y, t)$, which has its own equation of motion. The level-set function evolves through an advection equation. Unlike in the phase field models, the interface is not required to have a finite thickness or width, and thus acts as a discontinuity surface across which the material properties may have finite jumps.

We have implemented a level set method for tracking the solid-solid interface and coupled it with the finite element solver. The level set function

$\varphi(x, y, t)$ is a phase indicator which satisfies that

$$\varphi(x,y,t)\begin{cases} > 0, \text{ if } (x,y) \text{ belongs to Solid 1} \\ < 0, \text{ if } (x,y) \text{ belongs to Solid 2} \\ = 0, \text{ if } (x,y) \text{ is on the interface} \end{cases}, \tag{2.80}$$

as shown in Fig. 2.7 (Left). The normal propagation of the interface is captured by the evolution of the zero level of $\varphi(x, y, t)$. This is achieved with a passive advection of the entire level set according to

$$\frac{\partial \varphi}{\partial t} + W|\nabla \varphi| = 0, \tag{2.81}$$

where W is the extension velocity on $\varphi(x, y, t)$ and is required to match the normal velocity given by Eq. (2.63) on the interface itself where $\varphi(x, y, t) = 0$. Any function satisfying Eq. (3.29) is a potential candidate for a level set function. However, numerically the level set is often a signed distance function defined as the shortest distance from a point on the surface to the interface with the property that $|\nabla \varphi| = 1$. The advection velocity in Eq. (2.63) can be reconstructed from the interfacial velocity by solving [59]

$$\nabla W \cdot \nabla \varphi = 0, \tag{2.82}$$

with the prescribed boundary condition for the velocity at the interface. The level set is updated by iterating Eq. (2.81) on a rectangular grid. A point on the unstructured grid is located on the regular grid by local interpolation.

Numerical results

In the numerical simulations, we have explored the long time dynamics for various regions in the parameters space. Numerical results validate the stability domains in the parameter space. That is, for a set of parameter values where the interface is predicted to be linearly stable, the numerical simulations show that the interface will flatten also when we start with a finite size perturbation. For a set of parameter values in the unstable domain, the interface evolves into a finger-like pattern in the non-linear regime.

In Figs. 2.8-2.9, we present numerical simulations using parameter regions where the interface is either stable or unstable. Fig. 2.8 shows the time evolution of an initial cosine morphological pertubation. In the left panel, we apply a normal load, whereas in the right panel the load is tilted at an angle

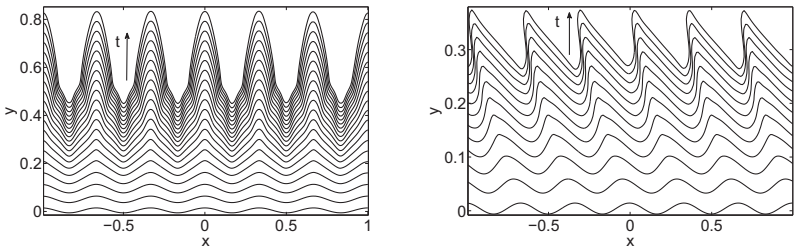

Figure 2.8: Simulations of the temporal evolution of a solid-solid interface in the parameter space where the interface is predicted to be unstable. The profile of the interface is plotted at different times and the time arrow suggests the direction of propagation into the upper domain. We have used $(\rho_{0,1}, \rho_{0,2}) = (2, 1)$, $(\nu_1, \nu_2) = (0.35, 0.35)$, $(G_1, G_2) = (6.75, 1.35) \times 10^3$ and $\sigma_\infty = -1$. We start with an initial cosine perturbation. (Left) The system is loaded only in the normal direction. (Right) The system is sheared on the horizontal boundary with $\sigma_{xy} = 0.5$, so that the principal compaction direction is at an angle with the normal. As a consequence, the fingers become tilted and aligned with the loading direction.

with respect to the vertical direction. The principal compression direction determines the orientation of the fingers as shown in the two panels. In both cases, the interface propagates into the lighter (softer) phase at a uniform speed. At the same time, the initial undulations grow into fingers that have smoother tips (seen when the normal points into the upper solid) and steeper valley sides.

Fig. 2.9 (Left) panel illustrates the evolution of a random morphological perturbation. The interface front develops fingers which grow at different rates depending on their amplitude. In the transitory period, the small scale irregularities grow at an exponential rate with a growth rate predicted by the linear stability analysis. After they reach a certain amplitude, the bumps start interacting with each other. During their competition, some bumps may overshadow the growth of their neighbours and eventually assimilate the smaller ones. In this regime, we see a crossover, from an exponential growth to a power-low growth. The mearging of fingers leads to a coarsening effect in the long time behaviour. Asymptotically, one would expect to observe only the largest fingers spanning the system size. In the right panel, we show

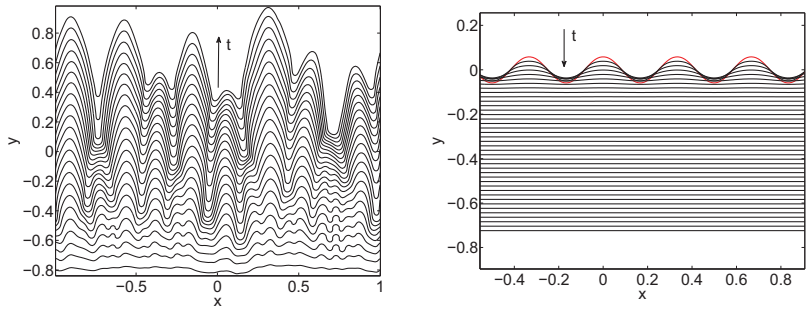

Figure 2.9: Simulations of the temporal evolution of a solid-solid interface in the parameter space where the interface is predicted to be unstable (Left) or stable (Right). The profile of the interface is plotted at different times and the time arrow suggests the direction of propagation. (Left) We have used $(\rho_{0,1}, \rho_{0,2}) = (2, 1)$, $(\nu_1, \nu_2) = (0.35, 0.35)$, $(G_1, G_2) = (6.75, 1.35) \times 10^3$ and $\sigma_\infty = -1$. We start with an initial random perturbation. The fingers grow in amplitude at different rates depending on the wavenumber. The competition between fingers leads to overshadowing and merging that have a coarsening effect on the long term evolution.(Right) We have used $(\rho_{0,1}, \rho_{0,2}) = (1, 1)$, $(\nu_1, \nu_2) = (0.25, 0.25)$, $(G_1, G_2) = (6.75, 1.35) \times 10^3$ and $\sigma_\infty = -1$. We start with an initial cosine undulation (red line). This decays to a flat interface.

the morphological evolution in a stable parameter region. In this case, the initial undulations are flatten out and in the long time the flat interface is propagating with a uniform velocity into the metastable phase.

2.4 Discussions

We have provided a study of mass transport at an interface between two phases with a single mobile component. We analyzed the morphological dynamics in the diffusion limited regime for a liquid-solid interface and in the reaction limited regime for a solid-solid interface. In both cases, the driving force of mass transport is controlled by the spacial variations in normal stress and elastic energy at the interface. The interface properties are incorporated in the theory by assuming an isotropic surface tension and considering the

stabilizing effect of curvature gradients.

Since many active processes in nature are described by the coupling of diffusion mechanisms to mechanical deformations, we believe that our theory is relevant to various situations ranging from nanostructures (e.g. quantum dots [47] or epitaxial growth [21]) to geology (e.g. grain to grain boundaries [24, 7]). However, the thermodynamical conditions for Earth processes are often determined both by stress or pressure and temperature. In the present formulation, we consider the limit where the effect of stress prevails over that of temperature. This assumption is valid at low temperatures below the critical phase transitions values for both phases and in a regime where temperature is continuous across the interface. A normal jump in the temperature gradients induces melting or solidification along the interface and leads to the Mullins Sekerka (MS) instability. The interfacial cellular pattern due to this instability occurs at a scale which is roughly estimated from thermal diffusion length and chemical capillary length given as $\gamma T_m/L\Delta T$ where L is the latent heat, ΔT is the temperature jump (miscibility gap), T_m is the melting temperature and γ is the surface tension. The selected lengthscale λ_{MS} is typically in the $10-100$ μm range. On the other hand, the ATG grooves can occur either in the range of $10-100$ nm scales if the elastic energies are balanced by the surface tension $\lambda_{ATG} \sim \gamma E/\sigma_\infty^2$ or in the range of $0.1-1$ cm when the preferred scale is calculated by balancing the elastic force with the gravitational force $\lambda_{ATG} \sim \sqrt{\gamma/g\delta\rho}$, where g is the gravitational acceleration and $\Delta\rho$ is the jump in the mass density. As the two instabilities occur on well-separated lengthscales, one may think that the two effects can be decoupled. However, previous studies in [14, 10] suggest a strong coupling between thermal and stress induced instabilities in directional solidification fronts. The temperature gradients effectively increases the effective gravity such that it brings down the ATG instability in the same range as the MS instability. The coexistence of the two effects is predicted to change the bifurcation stability condition and the selected pattern.

Future work is required to refine our models by considering thermal gradients and thermoelastic effects on the morphological instability.

Chapter 3

Porosity evolution by pressure solution

In this chapter, we discuss the large-scale effect of stress-enhanced local dissolution at the grain contacts. Fluid assisted dissolution and diffusion along stressed contacts, also known as pressure solution, are taking place at a discrete microscopic level, and induce a viscous creep effect at a macroscopic level of a porous media. In the continuum formulation, we derive the effective viscous creep describing the evolution of the porosity due to pressure solution. For a one dimensional porous column, the equation becomes analytically amenable and is characterized by solitary wave solutions. An analogy with the KdV equation is provided and numerical simulations are used to complement the analysis.

3.1 Pressure solution at the grain scale

Pressure solution refers to a mechanism by which compressed grains may dissolve at their stressed contact surfaces, diffuse along the contact in a thin fluid film and precipitate on the free surfaces [65]. Compared to other mass transport mechanisms driven by stress (Coble creep [11], Nabarro-Herring creep [46, 26]), pressure solution is assisted by a thin fluid film present in the contact between grains. The picture one has in mind when discussing the pressure solution operating at the grain scale is depicted in Fig 3.1.

The macroscopic effect of pressure solution is an overall compaction and deformation by viscous creep of a grain aggregate under stress [65, 54, 53].

Geological evidences support the idea that pressure solution is an active process in the formation of sedimentary rocks under compaction and that it may lead to localized patterns, such as stylolites and dissolution seams [61].

A thermodynamical formulation of pressure solution calls for an appropriate definition and use of the thermodynamics concepts associated with stressed solids. The thermodynamics of a stressed solid in contact with a fluid was fundamentally laid out by Gibbs [22], and refined by later works in [64, 28, 50] etc. The local chemical equilibrium in a heterogenous system requires that the chemical potential for each component is constant across interfaces. Here we shall treat the case of two phases which can exchange one component where the chemical potential equals the specific Gibbs free energy. It has been argued that the chemical potential at a stressed solid surface can be defined as [58]

$$\mu = f - \sigma_{nn}\mathcal{V}, \tag{3.1}$$

where σ_{nn} is the normal stress vector at the interface, and f is the Helmholtz free energy per mole and $\mathcal{V}$ is the molar volume of the component in the stressed state. When the solid is stressed hydrostatically with the surrounding fluid pressure p, the chemical potential at its surface is given by $\mu_0 = f_0 + p\mathcal{V}_0$, where the subindex refers to the hydrostatic state. Eq. (3.1) can be written relative to the hydrostatic reference state as [53]

$$\Delta\mu = \Delta f - \sigma_{nn}\Delta\mathcal{V} - \sigma^e_{nn}\mathcal{V}_0, \tag{3.2}$$

where $\Delta f = f - f_0$, $\Delta\mathcal{V} = \mathcal{V} - \mathcal{V}_0$ and $\sigma^e_{nn} = \sigma_{nn} - (-p)$ is the effective stress acting along the solid contact. $\Delta\mu$ is the work per atom needed for a reversible exchange of matter between the stressed solid surface and the fluid film. The chemical equilibrium in the contact channel is achieved when there is no jump in the Helmholtz free energy, the molar volume of the dissolved component is the same as in the solid state and the contact stress equals the pore fluid pressure (no exceeding stress at the contact).

Pressure solution, as an out-of-equilibrium process, is associated with the dissolution in the grain contact, subsequent mass transport by diffusion along the contact and precipitation to the surface at the pore fluid pressure. Even though the change in Helmholtz free energy as well as the volumetric changes suffice to drive a chemical reaction process, it can be shown that the effective contact stress σ^e_{nn} is the leading term and therefore the other contributions are of higher order, $\Delta\mu \approx -\sigma^e_{nn}\mathcal{V}_0$. The mass transport is confined along the

grain contact and is mediated by diffusion in a thin fluid film with a mass flux proportional to the chemical potential gradient, namely

$$J = -\mathcal{M}\frac{\partial}{\partial x}\Delta\mu = \mathcal{M}\mathcal{V}_0\frac{\partial\sigma^e_{nn}}{\partial x}, \tag{3.3}$$

where $\mathcal{M}$ is a positive defined mobility coefficient. In the steady state regime with no transport by fluid advection, the diffusion along the grain boundary balances the dissolution rate Q (Q being positive valued for dissolution and negative valued for precipitation) and this implies therefore that

$$\mathcal{M}\mathcal{V}_0\frac{\partial^2\sigma^e_{nn}}{\partial x^2} = Q. \tag{3.4}$$

The above equation can be easily integrated in the assumption that Q is constant along the grain boundary to obtain a solution for the effective stress given by

$$\sigma^e_{nn} = \frac{Q}{\mathcal{M}\mathcal{V}_0}(x^2 - a^2), \tag{3.5}$$

with the boundary conditions that the effective stress vanishes at the contact edges. We see that the contact stress is maximum, in its absolute value, at the middle of the grain-to-grain contact and relaxes to the hydrostatic pressure at the edges. Integrating out the spatial dependence, we then obtain a relation for the average effective stress at the contact given by

$$\bar{\sigma}^e_{nn} = -\frac{2a^2}{3\mathcal{M}\mathcal{V}_0}Q. \tag{3.6}$$

The dissolution rate Q can be associated with the amount of surface removal per unit time and, thus, is proportional to the normal velocity with which the grains converge to each other. The normal velocity at the contact is related to the normal strain rate $\dot{\epsilon}_{nn} = \partial_n v_n$, and therefore the dissolution rate can be expressed as proposed in [54] as $Q = -2a\dot{\epsilon}_{nn}/d$. With this definition of the reaction rate in mind, we rewrite the original Eq. (3.6) as

$$\bar{\sigma}^e_{nn} = \frac{4a^3}{3d\mathcal{M}\mathcal{V}_0}\dot{\epsilon}_{nn}. \tag{3.7}$$

Eq. (3.7) refers to an overall viscous creep of an aggregate of grains subjected to a compressional load. The pressure solution creep is controlled by the diffusional mass transport along the grain contact and this is reflected in the

dependence of the bulk viscosity on the mobility coefficient and the geometry of the grain-to-grain contact, $\eta = \frac{4a^3}{3d\mathcal{M}\mathcal{V}_0}$.

In principle, a similar derivation may be carried out for stress induced precipitation, when the material tends to be deposited where the stress is high. The enhanced stress at the grain contact acts as a force of crystallization [65].

The above analysis is worked out in the limit where the fluid film is at chemical equilibrium with the pore fluid and its neighboring solid surface. The classical scenario of pressure solution applies thus for closed pores with a pore fluid acting as a "chemical bath" for the contact fluid film. The other crucial assumption is that the pore fluid is at equilibrium with the grain surface surrounding it. In other words, the fluid flows through the pore network at a pace that will allow for chemical equilibration with the pore walls. Thus, the walls are not corroded by the flow. The picture that we have in mind is the following. Imagine a set of thin channels, representing the fluid film at the grain contacts, which end into a set of pores. The pore fluid is at equilibrium with its walls and with the fluid channel, but the later can corrode its straight walls which represent the contact boundary between the grains. In this picture, the channels are neutral with respect to each other and hence it is enough to study just a single channel. One can relax the equilibrium assumption between the contact fluid and the pore fluid by allowing for supersaturation or undersaturation in the contact relative to the pore space. This will induce a relative concentration gradient between the channels, and thus a coupling between them through the pore space. The pore fluid is still in equilibrium with the surrounding grains which implies that the chemical potential in the fluid is the same as at the grain surface,

$$\mu_0 = RT \ln c_0 = f_0 + p\mathcal{V}_0. \tag{3.8}$$

However, the contact fluid may not be in equilibrium with the pore fluid, thus its chemical potential

$$\mu_c = RT \ln c, \tag{3.9}$$

may differ from that in the pore fluid μ_0.

Mass transport by diffusion along the grain-to-grain contact is now controlled by the difference in the chemical potential between the contact fluid and the fluid film, namely

$$\mu - \mu_c = (\mu - \mu_0) - (\mu_c - \mu_0) = -\sigma^e_{nn}\mathcal{V}_0 - RT\frac{\Delta c}{c_0}, \tag{3.10}$$

where we have used the dilute approximation for $\ln(c/c_0) \approx \Delta c/c_0$. The reaction-diffusion equation in the steady state along the grain contact is then given by

$$\mathcal{M}\mathcal{V}_0 \frac{\partial^2 \sigma^e_{nn}}{\partial x^2} + RT\mathcal{M}\frac{1}{c_0}\frac{\partial^2 \Delta c}{\partial x^2} = Q. \tag{3.11}$$

We solve it with the additional boundary conditions that the concentration at the contact edges matches the pore concentration, i.e. $c(a) = c(-a) = c_0$. By averaging the solution over the contact, we obtain therefore an effective grain rheology given as

$$\mathcal{M}\mathcal{V}_0 \bar{\sigma}^e_{nn} + RT\mathcal{M}\frac{\Delta \bar{c}}{c_0} = \frac{4a^3}{d}\dot{\epsilon}_{nn}. \tag{3.12}$$

From the above expression we see that the grains will be compressed when the grain-to-grain stress is higher than the pore fluid pressure or when the fluid film is supersaturated compared to the pore fluid.

In the subsequent section, we show that the local grain boundary migration due to pressure solution amounts to a large scale creep law. We derive the continuum equations for the porous media from the local conservation laws of mass and momentum. The pressure solution creep comes in as a constitutive law.

3.2 Pressure solution in porous media

In the continuum hypothesis of a porous medium, the smallest element we are looking at is an arbitrary volume element, also called representative volume element or RVE, which is represented by a point at position $\mathbf{x}$ and time t (see Fig. 3.1 for a sketch of the RVE). However, in a physical sense, the RVE must be large enough to incorporate a significant collection of pores and grains, so that the statistical averages are well-defined. On the other hand, its volume size is sufficiently small, such that the field fluctuations and gradients across it can be neglected. In each RVE we distinguish two phases each occupying a certain volume fraction. One phase corresponds to the fluid in the pores and the other phase is given by a collection of grains, the constituents of the solid skeleton. The local volume fraction of pores is a continuous field described by the porosity density $\phi(\mathbf{x}, t)$. In the following analysis, we treat the particular case of fully saturated and connected pores (see e.g. Schrefler [57] for a recent review on the mechanics

and thermodynamics of (un)saturated porous media). By full saturation we mean that the pores are filled up entirely by a single phase which is different from the porous medium. Therefore, the porosity is also a direct measure of the volume fraction of the hosted phase. If we take a sponge as an example of a porous medium, then a fully saturated sponge is obtained by immersing it into water until all its pores are completely filled up. However, the sponge is partially saturated if some of its pores contain both air and water. The pore network is said to be connected when the contained phase is able to migrate from one pore region to another one. This is opposite to having a set of separated inclusions imbedded into a matrix. As a matter of notation, we denote the quantities associated with the solid matrix by the index s and those related to the fluid pore phase by the index f.

The two-phase continuum formulation is similar to the classical field description for homogenous media (see e.g. Malvern's textbook [40] for an introduction to the mechanics of homogenous continuum media). At the pore scale the two phases are well separated by the pore walls and the grain contacts, but this may not be the case at the continuum scale.

The porous material is set in a uniform gravitational field g or may be subjected to additional external stress fields. One of the main questions raised in this setup is related to how the material compacts as a response to gravitational forces and its internal stresses. There are several plausible mechanisms of compaction that have been proposed. One mechanism is due to the fluid expulsion and pore collapse due to the relative motion between phases. Thermal gradient or stress induced dissolution and precipitation may be active agents in the solid deformation. These mechanisms may coexist and contribute in different proportions to the overall compaction. However, the complexity of the equations emerged from their coupling makes it difficult to understand the behaviour of the solutions. Therefore, the numerous oversimplified models dealing with these mechanisms separately. The other question that is often raised concerns the type of dynamic instabilities developed during compaction, namely the existence of localized dissolution bands and their stability.

Hereby, we try to provide a theoretical framework for compaction in a porous material undergoing pressure solution. Previous analyses targeted the porosity evolution during a viscous creep by pressure solution in a closed porous solid [12] and an open system under sedimentation [18]. Our approach is to combine the continuum balance laws of mass and momentum with the thermodynamical formalism of pressure solution. Balance laws for porous

materials have been derived and studied previously in various setting and using various homogenization techniques like in modeling of compaction of partially molten rocks [42] or a more general viscous compaction [5]. We use a similar homogenization technique as proposed in [38] to derive the macroscopic effective grain boundary stress in relation to the grain shortening or strain rate.

3.2.1 Mass balance

The total mass of a porous rock with fluid emersed into its pores is assumed to be constant. Equivalently, the rock is treated as a closed system, i.e. there is no mass exchange between the rock and its environment nor any fluid can enter or escape through the rock boundaries. However, the fluid may be expelled from one rock region to another, as a result of compaction. We assume that the compaction is slow enough to allow for dissolution at the grain contacts and precipitation at the pore walls. To simplify things, we decouple the thermal effects from the chemical effects by having a temperature well below the critical melting temperature. Henceforth, the discussion is focussed on the chemical effects on the overall compaction.

The evolution of a mass element that occupies a certain volume fraction, namely ϕ for the fluid phase and $1-\phi$ for the solid phase, has been derived, for example, in [5, 42] based on phase averaging over the RVE. The differential forms for the mass balance of the phase averaged quantities are given as

$$\frac{\partial}{\partial t}[(1-\phi)\rho_s] + \nabla \cdot [(1-\phi)\rho_s v_s] = 0 \tag{3.13}$$

$$\frac{\partial}{\partial t}(\phi\rho_f) + \nabla \cdot (\phi\rho_f v_f) = 0 \tag{3.14}$$

where $v_f = \frac{1}{\delta V}\int_{\delta V_f} \bar{v}_f dv$ and $v_s = \frac{1}{\delta V}\int_{\delta V_s} \bar{v}_s dv$ denote the fluid velocity, respectively solid velocity averaged over the phase volume occupied in the RVE. The variables with a bar above represent microscopic quantities defined inside a RVE. A generic balance law relates the rate of change of a quantity contained in an arbitrary volume (in this case the mass of each phase) with its flux through the surface of the control volume and the leaking or income due to interactions. The mass densities ρ_f and ρ_s are defined with respect to the volume occupied by each phase inside the control volume. Upon summation, we obtain the continuity equation of a closed systems with a mass density $\rho_t = \phi\rho_f + (1-\phi)\rho_s$. Mass balance equations take a simpler form if we

assume constant mass densities. This implies that the phase constituents, i.e. grains and interstitial fluid, are intrinsically incompressible, and therefore their microscopic velocities, $\bar{v}_f$ and $\bar{v}_s$, are solenoidal. However, since the pore density changes locally with time, the phase averaged velocities, i.e. v_s, v_f, cease to be solenoidal [5]. Upon dividing in Eq. (3.13) by ρ_1 and Eq. (3.13) by ρ_2, and summing up the resulting equations we obtain the following constrain between the phase velocities,

$$\nabla \cdot [\phi(v_f - v_s) + v_s] = 0. \tag{3.15}$$

The relative concentration $\Delta\bar{c}$ represents the oversaturation or undersaturation along the grain contacts as compared to the pore fluid. Its averaging is less straightforward since it involves both the pore volume fraction and the total contact surface in a RVE. The evolution of $\Delta\bar{c}$ is influenced by the transport in the pore space, through diffusion and advection, as well as by the interaction between the contact channels. However, we limit our presentation here to the case where $\Delta\bar{c} = 0$ and leave aside this extension to a future study.

3.2.2 Momentum balance

We assume that the pore fluid is moving relative to the solid skeleton according to the Darcy's law [5]

$$\phi(v_f - v_s) = -\frac{k(\phi)}{\mu}\left(\nabla p_f - \rho_f g\hat{z}\right), \tag{3.16}$$

where μ is the fluid bulk viscosity and $k(\phi)$ is the matrix permeability determined by measuring the average velocity of a fluid moving through a permeable solid. Theoretical calculations of spherical grain packing suggest that the permeability is a monotonously increasing function with porosity and in the low porosity limit can be approximated by $k(\phi) = k_0(\phi/\phi_0)^n$, where $n \approx 3$. k_0 is typically of the order of $10^{-17} - 10^{-16}$ in dense limestone and $10^{-14} - 10^{-16}$ in sandstone [37]. The permeability is usually measured as the averaged velocity over a given volume and, therefore, the relative velocity is multiplied by the volume fraction of pores in that volume.

The stress sustained by each grain σ_{ij} satisfies the equilibrium condition $\partial_i\sigma_{ij} = 0$ (in the absence of external forces and negligible inertia effects)

and, by averaging it over the volume V_s inside the RVE, it upscales to a macroscopic stress given by

$$\langle \sigma_{ij} \rangle = \frac{1}{V} \int_{V_s} \sigma_{ij} dv = \frac{1}{V} \int_{\partial V_s} \sigma_{ik} n_k x_j dA, \tag{3.17}$$

where ∂V_s is the surface of the grain aggregate which is made of the total contact surface S_{gb} and the surface exposed to the pore fluid S_{fs}. The stress at S_{fs} is matched by the pore fluid pressure. By writing the contact stress relative to the hydrostatic pressure, we can express the averaged stress in relation to the effective grain-to-grain stress as [38]

$$\langle \sigma_{ij} \rangle = -\frac{1}{V} \int_{\partial V_s} p n_i x_j dA + \frac{1}{V} \int_{S_{gb}} \sigma^e_{ik} n_k x_j dA. \tag{3.18}$$

The first term amounts to the pore pressure averaged over the volume occupied by the grains and thus equals to $p(1-\phi)$, where ϕ is pore volume fraction. In the previous section, we found that the effective contact stress is related to the grains creep for vanishing supersaturation in concentration as

$$\bar{\sigma}^e_{nn} = \eta \dot{\epsilon}_{nn}, \tag{3.19}$$

with η being the viscosity coefficient. Upon inserting into the above equation, we therefore obtain that the macroscopic effective stress is given by

$$\langle \sigma^e_{ij} \rangle = \langle \sigma_{ij} \rangle + (1-\phi)p = \gamma \eta \langle \dot{\epsilon}_{ij} \rangle, \tag{3.20}$$

where γ is a measure of the total grain contact area relative to the control volume. Since we can not resolve this contact area because of the difficulty in tracking all possible contacts in a grain aggregate, we choose to eliminate it by redefining $\eta \to \gamma\eta$. The mean strain rate is related to the macroscopic solid velocity by $\langle \dot{\epsilon}_{ij} \rangle = 1/2(\nabla_j v_i + \nabla_i v_j)$.

The total macroscopic stress defined as $\langle \sigma_{ij} \rangle_t = \langle \sigma_{ij} \rangle - \phi p \delta_{ij}$ balances the gravitational forces $\nabla \cdot \langle \sigma_{ij} \rangle_t = -\rho_t g \delta_{i,3} \delta_{j,3}$. As a consequence, the effective stress is related to the pore fluid pressure by

$$\langle \sigma^e_{ij} \rangle = -\rho_t g z \delta_{i,z} \delta_{j,z} + p \delta_{ij}. \tag{3.21}$$

For the sake of simplicity we reduce our calculations to a one dimensional setup where we look at the porous solid in the z-direction along the gravitational field. The pore pressure p can be eliminated from the momentum

equations by substituting Eqs. (3.21) and (3.20) into Eq. (3.16), and therefore

$$\phi(v_f - v_s) = -\frac{k(\phi)}{\mu}\left(\eta\frac{\partial^2 v_s}{\partial z^2} + (1-\phi)\Delta\rho g\right), \tag{3.22}$$

where $\Delta\rho = \rho_s - \rho_f$. Furthermore, we can eliminate the fluid velocity v_f by combining the above equation with Eq. (3.15) to obtain

$$\frac{\partial v_s}{\partial z} = \frac{\partial}{\partial z}\left[\frac{k(\phi)}{\mu}\left(\eta\frac{\partial^2 v_s}{\partial z^2} + (1-\phi)\Delta\rho g\right)\right]. \tag{3.23}$$

For a one dimensional column, the above equation can be integrated once when additional boundaries conditions are known. In particular, we consider the case where at the top surface $z = 0$, the porosity is constant ϕ_0 and the fluid can reach the top surface due to buoyancy. The Darcy's flow driven by the density contrast balances the solid velocity by Eq. (3.15), thus at the surface $v_s(0) = k(\phi_0)(1-\phi_0)\Delta\rho g/\mu$ and $\frac{\partial^2 v_s}{\partial z^2} = 0$. Under these conditions, we find that

$$v_s = \frac{k(\phi)}{\mu}\left(\eta\frac{\partial^2 v_s}{\partial z^2} + (1-\phi)\Delta\rho g\right). \tag{3.24}$$

3.3 Dimensional analysis

In summary, the mass and momentum balance combined with a pressure solution creep law leads to the following set of coupled equations in (ϕ, v_s) variables,

$$\frac{\partial\phi}{\partial t} = \frac{\partial}{\partial z}[(1-\phi)v_s] \tag{3.25}$$

$$v_s = \frac{k(\phi)}{\mu}\left(\eta\frac{\partial^2 v_s}{\partial z^2} + (1-\phi)\Delta\rho g\right) \tag{3.26}$$

Equations are often studied in a dimensionless world by properly rescaling all the dimensional coordinates and variables. To arrive at the non-dimensional form of the original equations, we therefore employ the following scaling laws

$$\phi = \phi_0\hat{\phi}, \qquad v_s = v_0\hat{v} \tag{3.27}$$

$$z = l_c \cdot \hat{z}, \qquad t = t_0\hat{t}, \tag{3.28}$$

and a permeability on the form $k = \left(\frac{\phi}{\phi_0}\right)^n k_0$. The dimensionless variables are denoted by the hat upper symbol. ϕ_0 is a background constant porosity chosen to be equal to the porosity at the top surface, k_0 is a uniform permeability constant, $l_c = \sqrt{k_0\eta/\mu}$ is the typical compaction lengthscale, $v_0 = (1-\phi_0)\Delta\rho g k_0/\mu$ is the typical velocity, $t_0 = \phi_0 l_c/v_0$ is the typical compaction timescale. By inserting these rescalings into the main equations and dropping the hat symbol, we obtain the dimensionless forms given by

$$\frac{\partial\phi}{\partial t} = \frac{\partial}{\partial z}[(1-\phi_0\phi)v] \tag{3.29}$$

$$v = \phi^n\left(\frac{\partial^2 v}{\partial z^2} + \frac{1-\phi_0\phi}{1-\phi_0}\right). \tag{3.30}$$

3.4 Linear stability analysis

The steady state solution of Eqs. (3.29) and (3.30) satisfies

$$v = \frac{1-\phi_0}{1-\phi_0\phi}, \tag{3.31}$$

which is obtained using the boundary condition at $z = 0$ that $v = 1$ and $\phi = 1$. Inserting the steady state velocity into Eq. (3.30), we obtain an equation for the steady state porosity given by

$$\frac{(1-\phi_0\phi)^2}{\phi_0\phi^n} = 2\phi_0\left(\frac{\partial\phi}{\partial z}\right)^2 + (1-\phi_0\phi)\frac{\partial^2\phi}{\partial z^2} + \frac{(1-\phi_0\phi)^4}{\phi_0(1-\phi_0)^2}. \tag{3.32}$$

A solution to this equation is $\phi = 1$, which implies that $v = 1$. This corresponds to a steady state where the top surface boundary conditions apply everywhere, namely the system has a uniform porosity ϕ_0 and velocity v_0, which is due to a uniform Darcy's flux. Hereby we study the stability of this fixed point by analyzing the behavior of infinitesimal perturbations superimposed on it, namely

$$\phi = 1 + \epsilon\phi_1, \qquad v = 1 + \epsilon v_1, \tag{3.33}$$

with $\epsilon \ll 1$. The perturbation scheme compatible with the boundary conditions at the surface $z = 0$ requires that $\phi_1(0) = v_1(0) = 0$. Inserting the

perturbations into Eqs. (3.29)-(3.30) and retaining only the first order terms in ϵ, we obtain

$$\frac{\partial \phi_1}{\partial t} = (1-\phi_0)\frac{\partial v_1}{\partial z} - \phi_0 \frac{\partial \phi_1}{\partial z} \tag{3.34}$$

$$v_1 = \frac{\partial^2 v_1}{\partial z^2} + n\phi_1 - \frac{\phi_0 \phi_1}{1-\phi_0}. \tag{3.35}$$

The velocity perturbation v_1 can be eliminated by inserting the second equation into the first one to obtain

$$\frac{\partial \phi_1}{\partial t} + \phi_0 \frac{\partial \phi_1}{\partial z} = \frac{\partial^2}{\partial z^2}\left[\frac{\partial \phi_1}{\partial t} + \phi_0 \frac{\partial \phi_1}{\partial z}\right] + (n - n\phi_0 - \phi_0)\frac{\partial \phi_1}{\partial z}. \tag{3.36}$$

In the regime where the perturbation amplitude is infinitely smaller than the system size, i.e. $\epsilon \ll 1$, we may take the system as being infinite. When the perturbation decays smoothly to zero at the infinitely stretched boundaries, we can decompose it into a superposition of Fourier modes and study them individually in the regime where the coupling across modes is negligible. Thus, in the linear regime, we consider an arbitrary Fourier mode with the wavenumber k namely $\phi_1 \sim e^{ikz+\omega t}$ and insert it into the above equation. The corresponding dispersion relation is given by

$$\omega = ik\frac{n - 2\phi_0 - n\phi_0 - \phi_0 k^2}{1+k^2} \tag{3.37}$$

The fact that the growth rates are imaginary at all lengthscales implies that the perturbations are linearly neutral, in other words they neither growth or decay, but oscillate. The dependence of the wave velocity on the k-number shows that the waves are dispersive, i.e. the group velocity is different from the individual wave velocity.

Figure 3.2 illustrates the dependence of the wave velocity on the wavelength for different porosity backgrounds ϕ_0 and shows that the maximum wave velocity is attained at $\phi_0 = 0$, while it tends to decrease with increasing reference porosity state.

In the next section, we investigate the persistence of wave-like behaviour at finite amplitudes and in the nonlinear regime. We show that the waves are solitary in the steady state and dispersive in the time dependent evolution.

3.5 Stationary traveling waves

The solitary wave solution at a finite amplitude can be studied in the transitory regime of Eqs. (3.29) and (3.30) by a change of coordinates into the moving frame, namely

$$\tau = z - Vt, \tag{3.38}$$

where V is the constant speed of the traveling wave. In the moving frame, we have that $\phi(z,t) = f(\tau)$, $v(z,t) = g(\tau)$ and their original equations become

$$-V\frac{df}{d\tau} = \frac{d}{d\tau}\left[(1-\phi_0 f)g\right] \tag{3.39}$$

$$gf^{-n} = \frac{d^2 g}{d\tau^2} + \frac{1-\phi_0 f}{1-\phi_0}. \tag{3.40}$$

We can integrate the first equation with the condition at $t = 0$ and $z = 0$ that $f(0) = 1$ and $g(0) = 1$ and arrive at a relation between f and g given by

$$g = \frac{1-\phi_0 - V(f-1)}{1-\phi_0 f}. \tag{3.41}$$

Inserting it into the second equation and taking the limit $\phi_0 \to 0$, we obtain a nonlinear oscillator equation for the porosity on the form

$$V\ddot{f} - \frac{f^n - 1 + V(f-1)}{f^n} = 0, \tag{3.42}$$

where $\dot{f} = \frac{df}{d\tau}$.

The traveling-waves are in general of two kinds [4]. The first kind, such as the shock waves in Burgers equation, have a unique wave speed determined from the conservation laws alone. Namely, the front velocity is independent on the dissipative processes which determine the front internal structure and thickness. In contrast, fronts of the second type, i.e. flames, combustion waves or solutions to the KdV equation [27], propagate at a speed which can not be determined from the conservation laws. Therefore, in practice it is more difficult to calculate the velocity because it involves a refined analysis of the dissipative processes in the transition region. Often, the velocity is found from the spectrum of eigenvalues obtained in the processes of determining the internal structure of the front. The uniqueness of the wave velocity is more case dependent for waves of the second kind.

In our case, the porosity traveling wave is of the second kind and its velocity can be determined from the shape of it as demonstrated in [3] and shown below. By multiplying Eq. (3.42) with $\dot{f}$ and integrating it with the boundary conditions that $\dot{f}(0) = 0$ and $f(0) = 1$, we obtain that

$$\frac{V}{2}(\dot{f})^2 = [V - W(f)] \int_1^f q^{-n}(q-1)dq, \tag{3.43}$$

where

$$W(f) = \frac{\int_1^f (q^{-n} - 1)dq}{\int_1^f q^{-n}(q-1)dq}. \tag{3.44}$$

A possible solitary wave has therefore the speed $V = W(A)$, where A is the amplitude the solitary wave. In particular, for $n = 3$, the wave velocity is linearly proportional to its amplitude, $W(f) = -(2f + 1)$ and therefore $V = -(2A + 1)$. The negative sign in front implies that the wave is moving towards the top surface at $z = 0$. The fact that V is proportional with the amplitude means that the bigger waves move faster than the smaller waves.

The phase portrait of the flow is obtained by reducing Eq. (3.42) to a pair of coupled first order equations, namely

$$\dot{f} = p \tag{3.45}$$

$$\dot{p} = \frac{f^n - 1 + V(f-1)}{V f^n}. \tag{3.46}$$

For $V = -(2A + 1)$, the vector field in the phase space of (f, p) is plotted in Fig. 3.5. The solitary waves correspond to the homoclinic trajectory which passes the saddle point $(1, 0)$ in a loop that intersects the f axis at the maximal amplitude A.

Inserting the wave speed V into Eq. (3.43), we arrive at

$$p^2 = \frac{2(A-f)}{2A+1}\frac{(f-1)^2}{f^2}, \tag{3.47}$$

which, upon integration, gives an implicit solution for the shape of the solitary wave given by

$$\tau = \pm \int_f^A \frac{q}{q-1}\sqrt{\frac{2A+1}{2(A-q)}}dq. \tag{3.48}$$

Notice that the integral diverges as f approaches A. Thus, in order to properly resolve the singular the limit, we integrate up to $A-\epsilon$, expand the result around $\epsilon = 0$ and then take the limit of $\epsilon \to 0$. The integral then becomes equal to,

$$\tau = \sqrt{2(2A+1)}\left(\sqrt{A-1} + \frac{1}{\sqrt{A-1}} \arctan\sqrt{\frac{A-f}{A-1}}\right), \tag{3.49}$$

and represents an implicit expression for the shape of the solitary wave. The formula is evaluated numerically and plotted in Fig. 3.2.

3.6 Non-stationary porosity evolution

In the previous section, we found that the governing equations admit stationary solitary wave solutions, which propagate at a constant speed depending on wave amplitude. We now investigate their stability by starting from a certain porosity distribution and then asking if the solution evolves towards a configuration with separated traveling waves.

In the time dependent formulation, the implicit coupling between solid velocity and porosity in Eqs. (3.29) and (3.30) is much more difficult to deal with analytically. We therefore rely on numerical stability analysis. The evolution of porosity away from a uniform distribution in space can be followed by numerical integrations of Eqs. (3.29) and (3.30). This is done using a finite difference discretization combined with an operator splitting method. The advection part is resolved using a conservative first order Godunov scheme. The numerical result is shown in Figs. 3.4 and 3.5. We start initially either with a localized single Gaussian bell or a discrete set of Gaussian bells superimposed to the uniform background porosity. The initial pulse has not the solitary shape and we found that it disperses into a train of waves that propagate towards the top surface at $z = 0$. The dispersive propagation is expected from the linear stability analysis, where we have seen that the wave velocity is a nonlinear function of the wavenumber. However, the waves do not seem to converge to the stationary shape given by the solitary wave solution. This made us conclude that the solitary wave may actually be unstable. With time, the traveling pulses may overlap due to the interaction between the waves in the wake of one pulse and the head of the next pulse and this leads to a more complex pattern in the porosity evolution as seen in Fig. 3.5.

When solitary waves are colliding their shape does not remain unchanged after the collision and it shows that the waves are not solitons. This has also been emphasized in [3] from the existence of a finite number of conservation laws.

We conclude that the porosity evolution admits solitary traveling waves which can be studied by employing techniques used for other equations with soliton-like solutions, for example the Korteweg De-Vries (KdV) equation. For KdV equation, the soliton solutions are asymptotically stable and an initial condition disperses into a finite number of traveling solitons [27]. Unlike in KdV, we found that the porosity waves are unstable and numerically an initially localized condition tends to evolve towards a train of overlapping waves.

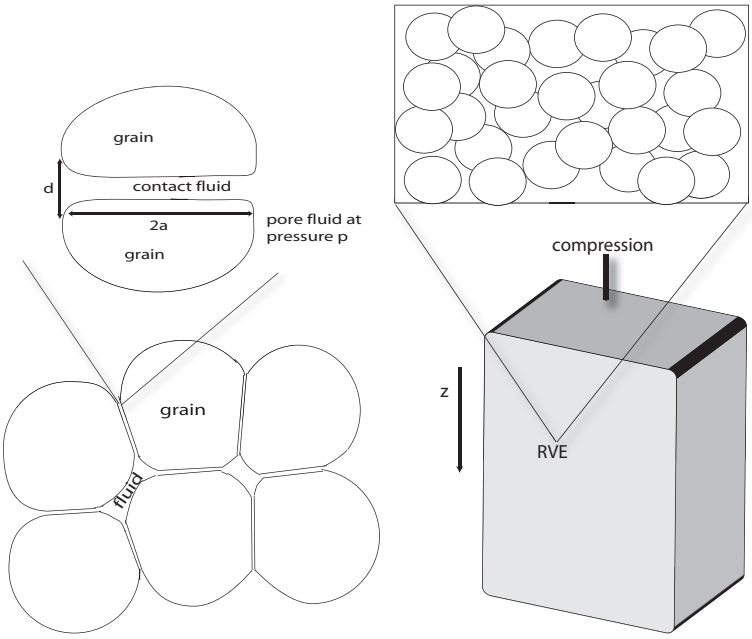

Figure 3.1: (Left) Sketch of the intergranular pressure solution. For spherical grains the contact surface is a disc with the diameter $2d$. Hereby the analysis is done for a 2d transversal cut across the contact area. Therefore, we have that the contact is a straight line stretching from $-a$ to a. Inside the contact there is a thin fluid film with a thickness d much smaller than the grain diameter. At the edges of the contact, the fluid film is connected to the pore fluid. (Right) An illustration of the RVE in a porous solid. The RVE contains a large collection of grains surrounded by a fluid, which at a macroscopic continuum scale is represented by a material point.

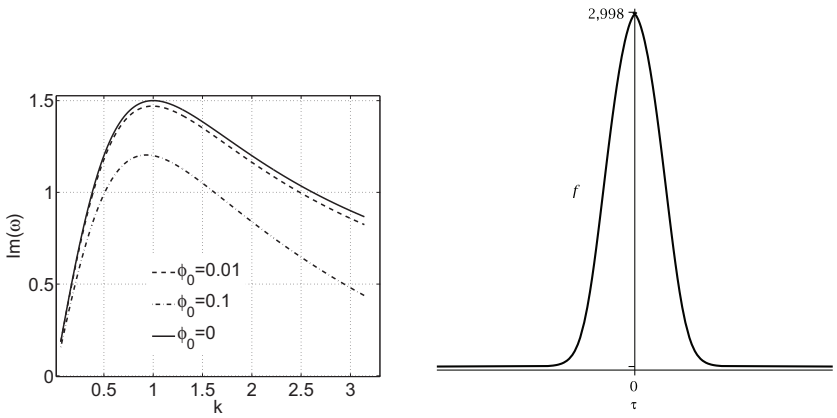

Figure 3.2: (left) Wave speed as a function of wavenumber k for infinitesimal amplitude perturbation in porosity. The maximal wave speed is lowered with increasing the background porosity. (right) The shape of the porosity solitary wave in the comoving frame, $\tau = x + (2A + 1)t$.

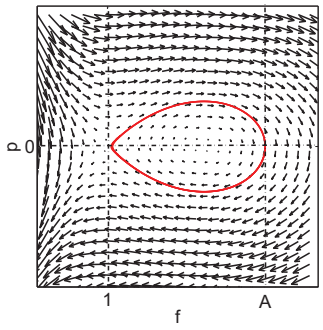

Figure 3.3: The vector field in phase space of (f, p), where $p = \dot{f}$. The red curve represent the separatrix which connects the point $(1, 0)$ with the point $A, 0$.

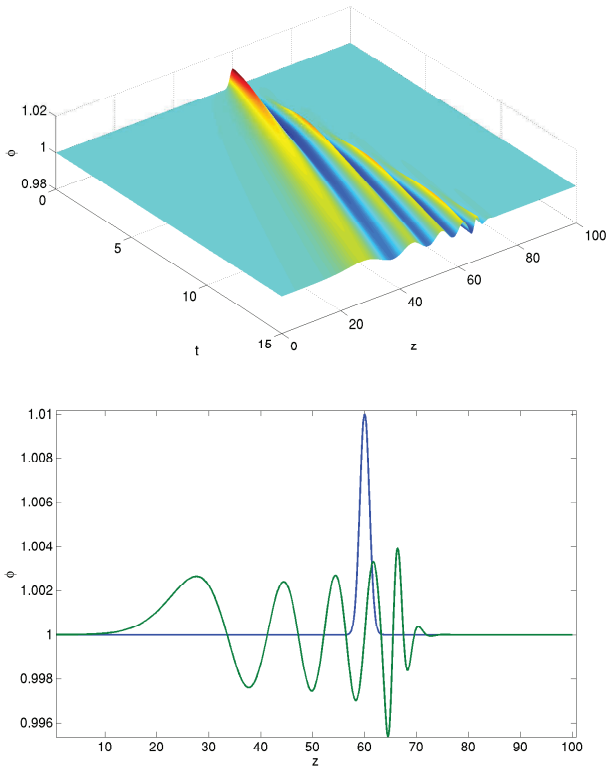

Figure 3.4: Numerical simulation of the porosity evolution. The starting condition is given by a single Gaussian bell superimposed to the constant background porosity. The pulse will propagate upwards leaving behind a train of secondary waves.

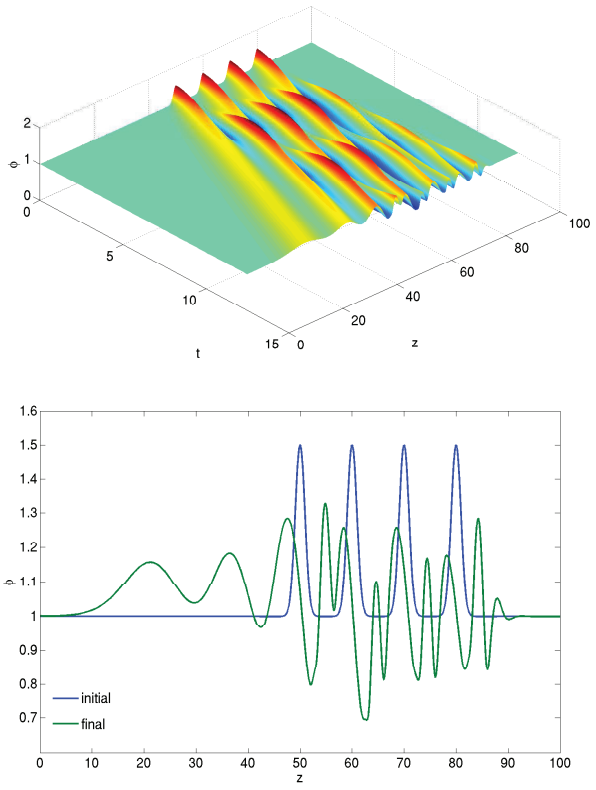

Figure 3.5: Numerical simulation of the porosity evolution. The starting condition is given by few localized pulses in porosity which at later times propagate upwards leaving behind a train of secondary waves.

Bibliography

[1] C. L. Angevine and D. L. Turcotte. Porosity reduction by pressure solution: a theoretical model for quartz arenites. *Geological Society of America Bulletin*, pages 1129–1134, 1983.

[2] R. Asaro and W. Tiller. Interface morphology development during stress corrosion cracking: Part 1. *Met. Trans.*, 3:1789–1796, 1972.

[3] V. Barcilon and F.M. Richter. Nonlinear waves in compaction media. *J. Fluid Mech.*, 164:429–448, 1986.

[4] G.I. Barenblatt. *Scaling, self-similarty, and intermediate asymptotics*. Cambridge University Press, 1996.

[5] D. Bercovici, Y. Ricard, and G. Schubert. A two-phase model for compaction and damage. 1. general theory. *Journal of Geophysical Research*, 106(B5):8887–8906, 2001.

[6] P. Berger, P. Kohlert, K. Kassner, and C. Misbah. Pattern selection in biaxially stressed solids. *Physical Review Letters*, 90, 2003.

[7] J. Bisschop and D. K. Dysthe. Instabilities and coarsening of stressed crystal surfaces in aqueous solution. *Physical Review Letters*, 96, 2006.

[8] E. Bonnetier, C. Misbah, F. Renard, R. Toussaint, and J.-P. Gratier. Does roughening of rock-fluid-rock interfaces emerge from a stress-induced instability? *Eur. Phys. J. B*, 67:121–131, 2009.

[9] J.U. Brackbill, D. B. Kothe, and C. Zemach. A continuum method for modeling surface tension. *Journal of computational physics.*, 100:335–354, 1992.

[10] I. Cantat, K. Kassner, Misbah C., and H.M. Krumbhaar. Directional solidification under stress. *Physical Review E*, 58(5), 1998.

[11] R.L. Coble. A model for boundary diffusion controlled creep in polycrystalline materials. *Journal of Applied Physics*, 34(6), 1963.

[12] J.A.D. Connolly and Y.Y. Podladchikov. Decompaction weakening and channeling instability in ductile porous media: Implications for asthenospheric melt segregation. *Journal of Geophysical Research*, 112(B10205), 2007.

[13] B. Den Brok, J. Morel, and M. Zahid. In situ experimental study of roughness development at a stressed solid/fluid interface. *Geological Society, London, Special Publications*, 200:73–83, 2002.

[14] I. Durand, K. Kassner, Misbah C., and H.M. Krumbhaar. Strong coupling between diffusive and elastic instabilities in directional solidification. *Physical Review Letters*, 76(16), 1996.

[15] L.H. Estey and B.J. Douglas. Upper mantle anisotropy: a preliminary model. *Journal of Geophysical Research*, 91(B11):11393–11406, 1986.

[16] G. Falkovich, K. Gawedzki, and M. Vergassola. Particles and fields in fluid turbulence. *Reviews of Modern Physics*, 73, 2001.

[17] C. R. Fletcher and D.D. Pollard. Anticrack model for pressure solution surfaces. *Geology*, 9:419–429, 1981.

[18] A.C. Fowler and X. Yang. Pressure solution and viscous compaction in sedimentary basins. *Journal of Geophysical Research*, 104(B6):12989–12997, 1999.

[19] D. Gal, A. Nur, and E. Aharonov. Stability analysis of a pressure-solution surface. *Geophysical Research Letters*, 25(8):1237–1240, 1998.

[20] H. Gao. A boundary perturbation analysis for elastic inclusions and interfaces. *Int. J. Solids Struct.*, 28(703), 1991.

[21] H. Gao and W.D. Nix. Surface roughening of heteroepitaxial thin films. *Ann. Rev. Mater. Sci.*, 28:173–209, 1999.

[22] J. W. Gibbs. On the equilibrium of heterogeneous substances. *Transactions of the Connecticut Academy*, III:108–248, 1878.

[23] N. Goldenfeld. *Lectures on Phase Transitions and Renormalization Group*. Addison-Wesley Publishing Company, 1997.

[24] J.P. Gratier, L. Muquet, R. Hassani, and F. Renard. Experimental microstylolites in quartz and moceled application to natural structures. *Journal of Structural Geology*, 27:89–100, 2005.

[25] M.A. Grinfeld. Instability of the separation boundary between a nonhydrostatically stressed elastic body and a melt. *Dokl. Akad. Nauk SSSR*, 290:1358–1363, 1986.

[26] C. Herring. Diffusional viscosity of a polycrystalline solid. *Journal of Applied Physics*, 21, 1963.

[27] A. Jeffrey and T. Kakutani. Weak nonlinear dispersive waves: A discussion centered around the kortweg-de vries equation. *SIAM Review*, 14(4), 1972.

[28] W.B. Kamb. Theory of preferred crystal orientation developed by crystallization under stress. *The Journal of Geology*, 1959.

[29] K. Kassner, C. Misbah, J. Muller, J. Kappey, and P. Kohlert. Phase field modeling of stress-induced instabilities. *Physical Review E*, 63, 2001.

[30] D.A. Kessler, J. Koplik, and H. Levine. Dendritic growth in a channel. *Physical Review A*, 34(6), 1986.

[31] Y.-T. Kim, N. Goldenfeld, and J. Dantzig. Computation of dendritic microstructures using a level set method. *Physical Review E*, 64(2), 2000.

[32] D. Koehn, F. Renard, R. Toussaint, and C.W. Passchier. Growth of stylolite teeth patterns depending on normal stress and inite compaction. *Earth and Planetary Science Letters*, 257:582–595, 2007.

[33] A.N. Kolmogorov. Dissipation of energy in the locally isotropic turbulence. *C.R. Acad. Sci. USSR*, 30, 1941.

[34] Y. W. Kwon and H. Bang. *The finite element method using Matlab. Second Edition*. CRC Press LLC, 2000.

[35] L.D. Landau and E.M. Lifshitz. *Theory of elasticity*. Butterworth Heinemann, 3rd Edition, 1986.

[36] J. S. Langer. Instabilities and pattern formation in crystal growth. *Reviews of Modern Physics*, 52(1), 1980.

[37] A.C. Lasaga. Chemical kinetics of water-rock interactions. *Journal of Geophysical Research*, 89(B6):4009–4025, 1984.

[38] F.K. Lehner. A model for intergranular pressure solution in open systems. *Tectonophysics*, 245:153–170, 1995.

[39] V. L'vov and I. Procaccia. Viscous lengths in hydrodynamic turbulence are anomalous scaling functions. *Phys. Rev. Lett.*, 77, 1996.

[40] Lawrence E. Malvern. *Introduction to the mechanics of a continuum medium*. Prentice-Hall, Inc. Englewood Cliffs, N.J., 1969.

[41] O. Martin and N. Goldenfeld. Origin of sidebranching in dendritic growth. *Physical Review A*, 35(3), 1987.

[42] D. McKenzie. The generation and compaction of partially molten rock. *Journal of Petrology*, 25(3):713–765, 1984.

[43] W. W. Mullins. Theory of thermal grooving. *Journal of Applied Physics*, 28(3), 1957.

[44] W. W. Mullins and R.F. Sekerka. Stability of a planar interface during solidification of a dilute binary alloy. *Journal of Applied Physics*, 35(2), 1964.

[45] N. I. Muskhelishvili. *Some basics preblems of the mathematical theory of elasticity*. P. Noordhoff Ltd, Groningen-Holland, 1953.

[46] F.R.N. Nabarro. Dislocations in a simple cubic lattice. *Proc. Phys. Soc.*, LIX(2), 1946.

[47] R. Notzel, J. Temmyo, and T. Tamamura. Self-organized growth of ingaas quantum disks. *Nature*, 369(131), 1994.

[48] P. Nozieres. Amplitude expansion for the grienfeld instability due to uniaxial stress at a solid surface. *J. Phys. I France*, 3:681–686, 1993.

[49] J. Paret. Long-time dynamics of the three-dimensional biaxial grinfeld instability. *Physical Review E*, 72, 2005.

[50] M.S. Paterson. Nonhydrostatic thermodynamics and its geological applications. *Reviews of Geophysics and Space Physics*, II(2):335–389, 1973.

[51] F. Renard, P. Ortoleva, and J.-P. Gratier. Pressure solution in sandstones: influence of clays and dependence on pressure and stress. *Techtoniphysics*, 280:257–266, 1995.

[52] L.F. Richardson. Atmospheric diffusion shown on a distance-neighbour graph. *Proc. R. Soc. London, Ser. A*, 111(756):709–737, 1926.

[53] P.-Y.F. Robin. Pressure solution at grain-to-grain contacts. *Geochimica et Cosmochimica Acta*, 42:1383–1389, 1978.

[54] E. H. Rutter. Kinetics of rock deformation by pressure solution. *Phil. Trans. R. Soc. Lond. A*, 283:203–219, 1976.

[55] P. G. Saffman and G. Taylor. The penetration of a fluid into a porous medium or hele-shaw cell containing a more viscous liquid. *Proceedings of the Royal Society of London. Series A, Mathematical and Physical Sciences*, 245(1242):312–329, 1958.

[56] J. Schmittbuhl, F. Renard, Gratier J.-P., and R. Toussaint. The roughness of stylolites: Implications of 3d high resolution topography measurements. *Physical Review Letters*, 93, 2004.

[57] B.A. Schrefler. Mechanics and thermodynamics of saturated/unsaturated porous media materials and quantitative solutions. *Appl. Mech. Rev.*, 55(4), 2002.

[58] R.F. Sekerka and J.W. Cahn. Solid-liquid equilibrium for nonhydrostatic stress. *Acta Materialia*, 52:1663–1668, 2004.

[59] J. A. Sethian. *Level set methods and fast marching methods*. Cambridge University Press, 1999.

[60] D. J. Srolovitz. On the stability of surfaces of stressed solids. *Acta Metall.*, 37(2):621–625, 1959.

[61] R. Tada and R. Siever. Pressure solution during diagenesis. *Ann. Rev. Earth Planet. Sci.*, 17:89–118, 1989.

[62] J.M. Taylor. Pore-space reduction in sandstones. *Bulletin of the american association of petroleum geologists*, 34(4):701–716, 1950.

[63] R.H. Torii and S. Balibar. Helium crystals under stress: The grinfeld instability. *Journal of Low Temperature Physics*, 89(1/2), 1992.

[64] J. Verhoogen. The chemical potential of a stressed solid. *Transactions, American Geophysical Union*, 32(2), 1951.

[65] P.K. Weyl. Pressure solution and the force of crystallization. *Journal of Geophysical Research*, 64(11), 1959.

[66] D.J. Wollkind and L.A. Segel. A nonlinear stability analysis of the freezing of a dilute binary alloy. *Philosophical Transactions of the Royal Society of London. Series A. Mathematical and Physical Sciences*, 268(1191):351–380, 1970.

[67] Y. Xiang and W. E. Nonlinear evolution equation for the stress-driven morphological instability. *Journal of Applied Physics*, 91(11), 2002.

[68] W.H. Yang and D.J. Srolovitz. Cracklike surface instabilities in stressed solids. *Physical Review Letters*, 71(10), 1993.

[69] D.-H. Yeon, P.-R. Cha, and M. Grant. Phase field model of stressed-induced surface instabilities: Surface diffusion. *Acta Materialia*, 54, 2006.

Appendices

Appendix A

Paper I

Stress-driven phase transition and the roughening of solid-solid interfaces

---

Physical Review Letters 100 *(2008)*

Stress-Driven Phase Transformation and the Roughening of Solid-Solid Interfaces

L. Angheluta,[1] E. Jettestuen,[1] J. Mathiesen,[1] F. Renard,[1,2] and B. Jamtveit[1]
[1]*Physics of Geological Processes, University of Oslo, Oslo, Norway*
[2]*LGCA-CNRS-OSUG, University of Grenoble, BP 53, F-38041, France*
(Received 13 November 2007; published 7 March 2008)

The application of stress to multiphase solid-liquid systems often results in morphological instabilities. Here we propose a solid-solid phase transformation model for roughening instability in the interface between two porous materials with different porosities under normal compression stresses. This instability is triggered by a finite jump in the free energy density across the interface, and it leads to the formation of fingerlike structures aligned with the principal direction of compaction. The model is proposed as an explanation for the roughening of stylolites—irregular interfaces associated with the compaction of sedimentary rocks that fluctuate about a plane perpendicular to the principal direction of compaction.

DOI: 10.1103/PhysRevLett.100.096105 PACS numbers: 68.35.Ct, 68.35.Rh, 91.60.Hg

Morphological instabilities in systems out of equilibrium are central to most research on pattern formation. A host of processes give rise to such instabilities, and among the most intensively studied are the surface diffusion mediated Asaro-Tiller-Grinfeld instability [1–3] in the surfaces of stressed solids in contact with their melts, surface diffusion mediated thermal grooving, and solidification controlled by thermal diffusion in the bulk melt [4]. In sedimentary rocks and other porous materials local stress variations typically promote morphological changes via dissolution in regions of high stress, transport through the fluid saturated pore space, and precipitation in regions of low stress. This phenomenon is known as pressure solution or chemical compaction. Such processes are often accompanied by the nucleation and growth of thin irregular sheets, interfaces, or seams called stylolites [5]. Stylolites form under a wide range of geological conditions as rough interfaces that fluctuate about a plane perpendicular to the axis of compression. They are common in a variety of rock types, including limestones, dolomites, sandstones, and marbles, and they appear on scales ranging from the mineral grain scale to meters or greater. A common feature of stylolitic surfaces is small scale roughness combined with large vertical steps in the direction of the compression. Residual unsoluble minerals (i.e., clays and oxides) often accumulate at the interface as stylolites evolve. Despite the considerable attention given to the rich morphology of stylolites there is still no consensus on the mechanism(s) controlling their formation [6–9]. Here we demonstrate that even if the stylolite is a consequence of pressure solution alone, porosity or other material property gradients may drive the roughening process. In particular, we demonstrate that a compressional load normal to a no-slip solid-solid phase boundary gives rise to a morphological instability. Our setup differs from the commonly studied solid-melt systems, where stresses are applied in the lateral direction and the melt is in a hydrostatic state (see, e.g., [10]).

Generally, rocks are heterogeneous bodies with spatially variable porosities. The strain energy densities may be larger in regions of high porosity (i.e., low modulus) than in regions of low porosity. Thermodynamically, the total free energy of the system can be reduced by decreasing the porosity variations. In this Letter, a simple model for stylolite formation, in which high porosity rock is transformed into low porosity rock at the interface between the low porosity and high porosity materials, is investigated. This solid-solid "phase transformation" is driven by gradients in the free energy per unit volume of mineral, which can be substantial in regions with large porosity variations. The general approach used in this work could be applied to other solid-solid interface roughening phenomena.

We consider a two-dimensional system divided into elastic regions with different but homogeneous porosities (Fig. 1). Without lack of generality, we limit our consideration to two dissimilar materials separated by a single interface. The stress boundary condition is a uniform compression in the vertical direction applied at the top and bottom boundaries. The two phases are separated by a sharp and coherent boundary; i.e., no defects or voids can form along the interface. This translates into continuity of the displacement vector $\mathbf{u}(\mathbf{r}, t)$ across the interface, $[\mathbf{u}] = 0$. Here and in other equations the brackets denote the jump in the quantity inside the brackets when the interface is approached from above and below. Under given load conditions the displacement field induced by the compression gives rise, in the linear regime, to a strain tensor of the form

$$\epsilon_{ij} = \frac{1}{2}\left(\frac{\partial u_j}{\partial x_i} + \frac{\partial u_i}{\partial x_j}\right). \tag{1}$$

The two solid phases are characterized by their Young's moduli, $E_{1,2}$, and Poisson's ratios, $\nu_{1,2}$. When $E_1 < E_2$, the upper region will be compressed the most and therefore the elastic energy density will be higher in this region. The first step toward a model for the roughening of a solid-solid

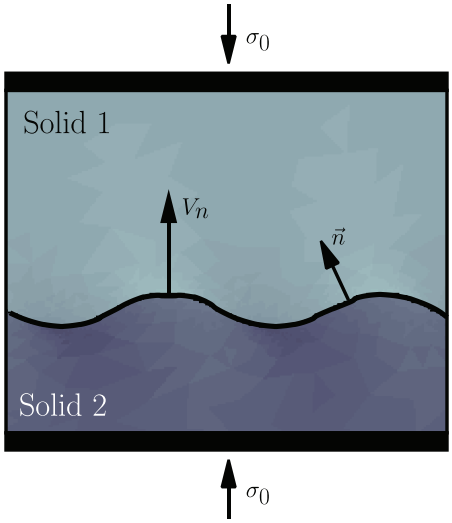

FIG. 1 (color online). Basic setup of the model for a moving interface between two elastic solid phases, characterized by different Young's moduli ($E_2 > E_1$) and Poisson's ratios ν_1, ν_2. The interface boundary propagates with a normal velocity V_n, when the solids are subjected to uniform far-field compressional stresses σ_0 in the vertical direction.

interface is based on this simple observation. First the elastic parameters of the materials are related to their porosities. Luo and Weng [11] proposed a homogenization method relating the effective bulk and shear moduli to the porosity of the solid. Using this approach, the effective Young's modulus decreases monotonically with the porosity. Consequently, a finite jump in porosity across the interface induces a jump in the elastic energy density, which drives the motion of the interface. Thermodynamically, the evolution of the interface corresponds to a phase transformation from a high to a low energy state.

It is assumed that the phase transformation occurs on a time scale that is much longer than the time required for elastic waves to propagate across the system, and the system is therefore always in elastostatic equilibrium. For an isotropic and homogeneous elastic body the elastic equilibrium condition is given by

$$\frac{\partial \sigma_{ij}}{\partial x_j} = 0, \tag{2}$$

together with the uniform uniaxial compression stress boundary condition, $\sigma_{ij}(x, y = \infty) = \sigma_0 \delta_{i,y} \delta_{j,y} < 0$, and the stress jump across the curved interface due to the effective surface tension is given by

$$[\sigma_{ij} n_j] = -\gamma \kappa n_i \text{ at the interface } \Gamma_t, \tag{3}$$

where κ is the curvature and γ is the local surface tension. In the limit of negligible surface tension, the stress vector is continuous across the interface ($[\sigma_{ij} n_j] = 0$).

For completeness, the basic principles used to derive an equation of motion are presented. When the system approaches an equilibrium configuration, the free energy will be a nonincreasing function of time:

$$\frac{d}{dt}\left(\int_V \mathcal{F} dv + \int_{\Gamma_t} \tilde{\mathcal{F}} ds\right) \leq 0, \tag{4}$$

where $\mathcal{F}$ is the free energy per unit volume and $\tilde{\mathcal{F}}$ is the interfacial free energy per unit area. Here, the subscript V indicates a volume integration and Γ_t indicates integration over the interface. The interfacial energy dissipation is obtained by confining the domain of integration to a narrow zone along the interface and taking the zero thickness limit [12]. This gives

$$-\int_{\Gamma_t} [\mathcal{F}] V_n ds + \int_{\Gamma_t} \left(\frac{d\tilde{\mathcal{F}}}{dt} - \kappa \tilde{\mathcal{F}} V_n\right) ds \leq 0, \tag{5}$$

where V_n is the normal velocity and κ is the local curvature of the interface. This implies the differential form given by

$$\frac{d\tilde{\mathcal{F}}}{dt} - (\kappa \tilde{\mathcal{F}} + [\mathcal{F}]) V_n \leq 0, \tag{6}$$

where the first term is the total time derivative of the local interfacial energy density. The local free energy is a function of the surface tension only (like fluid-solid interfaces) and thus, it is independent of time. Therefore, the time derivative can be neglected leading to the inequality

$$-(\kappa \tilde{\mathcal{F}} + [\mathcal{F}]) V_n \leq 0. \tag{7}$$

In the linear response regime, this inequality is satisfied when the velocity (the thermodynamic flux) is a linear function of the driving force, $(\kappa \tilde{\mathcal{F}} + [\mathcal{F}])$, namely,

$$V_n \sim c(\kappa \tilde{\mathcal{F}} + [\mathcal{F}]), \tag{8}$$

with $c \geq 0$. In the absence of surface tension, the normal velocity is simply proportional to the jump in the strain energy, i.e., $V_n \sim [\mathcal{F}]$. While the dynamical law for the interface Eq. (8) is very simple, the implementation in a numerical model is more challenging.

The model (Fig. 1) of the moving solid-solid interface was numerically implemented using the local force balance and energy dissipation equations [Eqs. (3) and (8)]. The stress field is obtained using the Galerkin finite element discretization of the elastostatic equations and the phase boundary is captured using the level set method. The level set method [13] is a powerful and reliable technique for tracking surfaces in any number of dimensions. At any time t, the d-dimensional interface Γ_t may be defined as the zero level cut through a scalar field φ ($d + 1$-dimensional surface), namely, $\varphi(\mathbf{x}, t) = 0$, where $\mathbf{x} \in \Gamma_t$. A change in the zero-level cut in response to a change in the scalar field may then be interpreted as a motion of the interface.

Therefore the change in the scalar field must correspond to motion of the zero-level cut with a given normal velocity **V**; this is done by updating the scalar field using a simple advectionlike equation

$$\frac{\partial \varphi}{\partial t} + V_n |\nabla \varphi| = 0. \quad (9)$$

The advection of the level set function is solved on a separate lattice using an upwind scheme. The full dynamical model of the solid-solid phase transformation front is then given by this equation together with Eq. (8).

In the numerical simulations, we have used periodic boundary conditions in the lateral direction to reduce possible finite size effects. The initial interface was generated by a directed random walk (Fig. 2, lower panel). The temporal evolution of the interface (Fig. 2, upper panel) was then recorded for different external stresses, σ_0, and elastic constants (E, ν). The elastic constants were computed from homogenization relations between elasticity and porosity [11]. As the interface advances increasing lateral stresses may appear behind the tips of the fingerlike structures. While such lateral stress may cause interface instability, it will have only a secondary effect on the overall transversal evolution.

Initially, the roughness of the interface grows exponentially

$$\sqrt{\int_{\Gamma_t} [h(s,t) - \bar{h}(t)]^2 ds} \sim \exp(t/t^*), \quad (10)$$

with a characteristic roughening time t^* that depends on the external stress and the jump in the elastic properties. To estimate the functional dependence of t^*, a set of numerical simulations was performed. First, the external stress σ_0 was systematically varied between 0.005 and 500 MPa for fixed values of the elastic constants ($E_1 = 40$ GPa, $E_2 = 60$ GPa, $\nu_1 = \nu_2 = 0.3$).

The results shown in Fig. 3 suggest that the characteristic time scales as $t^* \sim \sigma_0^{-2}$, and the prefactor depends on the elastic properties. In order to investigate this type of relation, the elastic constants across the interface were varied ($E_2 = 50$ GPa, E_1 in the range 5–16 GPa, $\nu_1 = \nu_2 = 0.3$). The data for the interface roughening collapse onto a curve which is exponential at small time scales with a crossover to a quadratic form at larger times (Fig. 4). Extracting the characteristic time in the exponential growth regime and rescaling it with σ_0^2, the functional dependence with respect to the jump in the elastic constants across the interface was determined (see Fig. 4 inset). The crossover from exponential to algebraic roughening depends on the value of the jump. For large jumps in the elastic energy or porosity, the roughening quickly undergoes a transition from exponential to quadratic growth in time. This crossover time is related to the formation and growth of the fingerlike structures shown in Fig. 2. By a simple dimen-

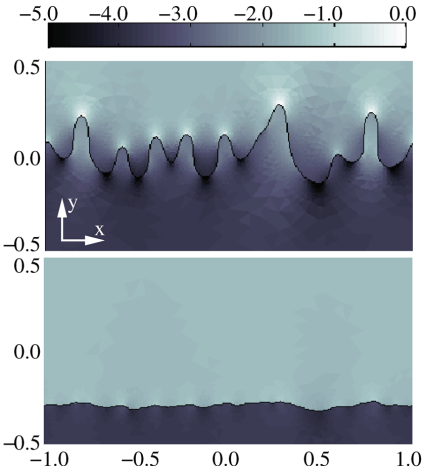

FIG. 2 (color online). Map of the logarithm of the elastic energy in the solids during the roughening process, with $E_1 = 10$ GPa, $E_2 = 60$ GPa, $\nu_1 = \nu_2 = 0.3$, and $\sigma_0 = 0.05$ MPa. Lower panel: initial $h(x)$ at $t = 0$. Upper panel: interface at a later stage of roughening.

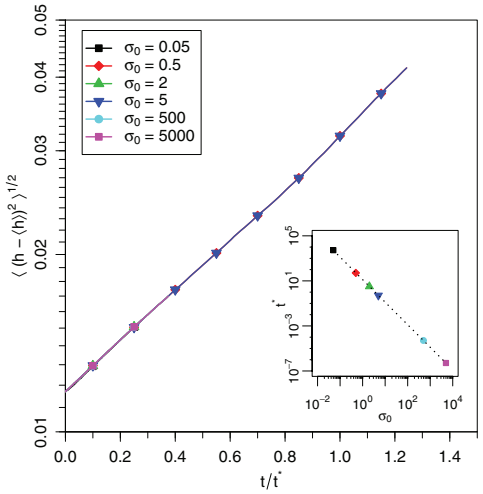

FIG. 3 (color online). Roughness as a function of time for six different external compression stresses σ_0 (in units of 10^5 Pa; see the legend) for a fixed jump in the Young's modulus and zero surface tension. The root means square height is plotted as a function of time, rescaled with the characteristic roughening time t^*, on a semilogarithmic scale. The data collapse shows the exponential roughening of the interface $\exp(t/t^*)$ with a stress independent preexponential factor. Inset: the characteristic time as a function of σ_0 is given by $t^* \sim \sigma_0^{-2}$ (shown by the dashed line).

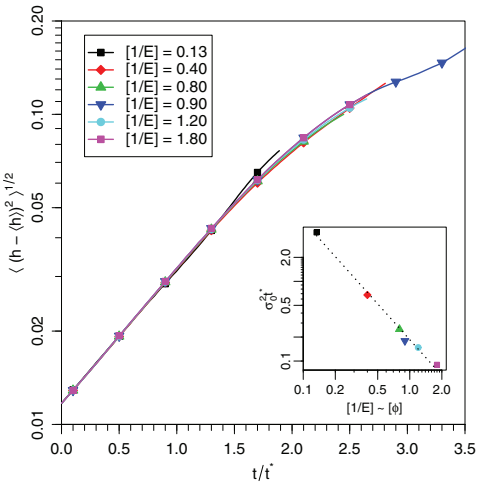

FIG. 4 (color online). Roughness as a function of time for different jumps in the Young's modulus $[1/E] = 1/E_1 - 1/E_2$ (measured in units of 10^{-10} Pa; see the legend) for fixed external stress ($\sigma_0 = 5$ MPa) and zero surface tension. The data are plotted against the time rescaled with t^* estimated numerically from the initial exponential growth. At large times, the roughness grows quadratically with increasing time. Inset: Log-log plot of the characteristic time rescaled with the corresponding external stress $\sigma_0^2 t^*$ as a function of the jump $[1/E]$. $t^* \sim \sigma_0^2 [1/E]^{-\alpha}$. As guide to the eye, we added a dashed line with exponent $\alpha = 3/2$.

sional argument, we also determined that the generic dependence of t^* on the external stress and elastic constants has the form

$$t^* \sim \frac{L}{V_n} \sim \frac{L}{c[\mathcal{F}]} \sim \frac{L}{c} \frac{1}{[(1-\nu^2)/E]} \frac{1}{\sigma_0^2}, \qquad (11)$$

where $[\mathcal{F}] = \mathcal{F}_1 - \mathcal{F}_2$ is the jump in the free energy density across the interface. The scaling relation is consistent with the numerical simulation results. The stress field may be calculated analytically with the same boundary and interface conditions for a straight interface perturbed by a sine function with small amplitude A. In linear perturbative analysis ($A \ll 1$) without surface tension, the solution is obtained using the method of Airy's potentials for 2D elastostatics [14]. The energy jump $[E]$ is proportional to kA^2, where $k = 2\pi/\lambda$ is the wave number. In other words, all the modes are unstable and those with the smaller wavelengths grow faster in the linear regime. The surface tension adds an ultraviolet cutoff resulting in small scale smoothening of the interface. The system was tested with and without surface tension, and in both cases the qualitative behavior was the same—an initial exponential roughening with a crossover to a finger-formation regime. Eventually, these fingers may stabilize due to transport of dissolved minerals and precipitation leading to pore clogging. Stress concentration at the tips is an important characteristic of the system, and the pronounced contrast in the energy density between the two phases leads to an enhanced chemical activity. In stylolites the roughening is often accompanied by small fractures aligned with the direction of compression, and this may be explained by the model if the stress concentration at the fingers exceeds the yield strength of the material.

To summarize, a simple solid-solid phase transformation model that predicts a morphological instability of the interface under uniform compressional stress has been developed and investigated. The instability is triggered by a finite jump in the elastic properties across the interface and a concomitant jump in the free energy density. We also showed that the characteristic time of roughening depends on the external applied stress and the elastic parameters jump, in such a way that a higher external compression load or a larger difference between the elastic properties of the phases shortens the time required to roughen the interface. This result allows the roughening time and formation rate of stylolites to be estimated as a function of burial depth in sedimentary basins.

This project was funded by *Physics of Geological Processes*, a Center of Excellence at the University of Oslo. The authors are grateful to Paul Meakin for fruitful discussions and comments.

[1] R. J. Asaro and W. A. Tiller, Metall. Trans. **3**, 1789 (1972).
[2] M. A. Grinfeld, Dokl. Akad. Nauk SSSR **290**, 1358 (1986).
[3] D. J. Srolovitz, Acta Metall. **37**, No. 2, 621 (1989).
[4] W. Mullins, J. Appl. Phys. **28**, 333 (1957)
[5] P. B. Stockdale, Indiana University Studies **IX**, 1 (1922); M. T. Heald, J. Geol. **63**, 101 (1955); P. K. Weyl, J. Geophys. Res. **64**, 2001 (1959); W. Park and E. Schot, J. Sediment. Petrol. **38**, 175 (1968); R. Bathurst, *Carbonate Sediments and Their Diagenesis* (Elsevier Science, New York, 1971).
[6] E. H. Oelkers, P. A. Bjørkum, and W. M. Murphy, Am. J. Sci. **296**, 420 (1996).
[7] J. Schmittbuhl, F. Renard, J. P. Gratier, and R. Toussaint, Phys. Rev. Lett. **93**, 238501 (2004).
[8] E. Aharonov and R. Katsman, "Modeling Stylolite Formation" (to be published).
[9] D. Koehn, F. Renard, R. Toussaint, and C. W. Passchier, Earth Planet. Sci. Lett. **257**, 582 (2007).
[10] Y. Xiang and W. E, J. Appl. Phys. **91**, 9414 (2002).
[11] H. A. Luo and G. J. Weng, Mech. Mater. **6**, 347 (1987).
[12] M. E. Gurtin, J. App. Math. Phys. **42**, 370 (1991).
[13] J. A. Sethian, *Level Set Methods and Fast Marching Methods* (Cambridge University Press, New York, 1999), 2nd ed.; S. Osher and R. Fedkiw, *Level Set Methods and Dynamic Implicit Surfaces* (Springer, New York, 2003).
[14] H. Gao, Int. J. Solids Struct. **28**, 703 (1991).

Appendix B

Paper II

Thermodynamics and roughening of solid-solid interfaces

Physical Review E 79 *(2009)*

Thermodynamics and roughening of solid-solid interfaces

Luiza Angheluta, Espen Jettestuen, and Joachim Mathiesen
Physics of Geological Processes, University of Oslo, Oslo, Norway
(Received 1 October 2008; revised manuscript received 12 January 2009; published 3 March 2009)

The dynamics of sharp interfaces separating two nonhydrostatically stressed solids is analyzed using the idea that the rate of mass transport across the interface is proportional to the thermodynamic potential difference across the interface. The solids are allowed to exchange mass by transforming one solid into the other, thermodynamic relations for the transformation of a mass element are derived and a linear stability analysis of the interface is carried out. The stability is shown to depend on the order of the phase transition occurring at the interface. Numerical simulations are performed in the nonlinear regime to investigate the evolution and roughening of the interface. It is shown that even small contrasts in the referential densities of the solids may lead to the formation of fingerlike structures aligned with the principal direction of the far field stress.

DOI: 10.1103/PhysRevE.79.031601 PACS number(s): 81.10.−h, 68.35.Ct, 68.35.Rh, 91.60.Hg

I. INTRODUCTION

The formation of complex patterns in stressed multiphase systems is a well-known phenomenon. The important studies of Asaro and Tiller [1] and Grinfeld [2] brought attention to the morphological instability of stressed surfaces in contact with their melts or solutions. In the absence of surface tension, small perturbations of the surface increase in amplitude due to material diffusing along the surface from surface valleys, where the stress and chemical potential is high, to surrounding peaks where the stress and chemical potential is low. Important examples of instabilities at fluid-solid interfaces include defect nucleation and island growth in thin films [3,4], solidification [5], and the formation of dendrites and growth of fractal clusters by aggregation [6]. The surface energy increases the chemical potential at regions of high curvature (convex with respect to the solution or melt, at the peaks) and reduces the chemical potential at region of low curvature (at the valleys) and this introduces a characteristic scale below which the interface is stabilized.

In systems where the fluid phase is replaced by another solid phase, i.e., solid-solid systems, the interface constraints alter the local equilibrium conditions. Here we study a general model for a propagating interface between nonhydrostatically stressed solids. The interface propagates by mass transformation from one phase into the other. The phase transformation is assumed to be local, i.e., the distance over which the solid is transported via surface diffusion or solvent mediated diffusion is negligible compared to other relevant scales of the system. Although the derivations apply to a diffuse interface, we shall here treat only coherent interfaces, where there is no nucleation of new phases or formation of gaps between the two solids [7,8], in the sharp interface limit. For example, in rocks such processes appear at the grain scale in "dry recrystallization" [9,10]. Common examples of coherent interfaces that migrate under the influence of stress include the surfaces of coherent precipitates (stressed inclusion embedded in a crystal matrix) [7] and interfaces associated with isochemical transformations. Most studies of solid-solid phase transformations have been limited to the calculation of chemical potentials in equilibrium and have provided little insight into the kinetics. Here we investigate the out of equilibrium dynamics of mass exchange between two distinct solid phases separated by a sharp interface. We expand on the recent work presented in Ref. [11] where we studied the phase transformation kinetics controlled by the Helmholtz free energy. It was shown that a morphological instability is triggered by a finite jump in the free energy density across the interface, and in the nonlinear regime this leads to the formation of fingerlike structures aligned with the principal direction of the applied stress.

In the majority of solid-solid phase transformation processes, the propagation of the interface is accompanied by a change in density. For this reason the density is an important order parameter that quantitatively characterizes the difference between the two phases. We consider two types of phase transitions underlying the kinetics, first order and second order, which result in fundamentally different behaviors at the phase boundary. A first-order phase transition occurs when the two phases have different referential densities and it typically results in morphological instability along the boundary whereas a second-order phase transition may either stabilize or destabilize the interface depending on Poisson's ratios of the two phases. A simple sketch of the stability diagram is outlined in Fig. 1 for relative values of density and shear modulus of the two phases.

The article consists of five sections. In Sec. II we derive a general equation for the kinetics for mass exchange at a solid-solid phase boundary separating two linear elastic solids. We utilize the derived equations on a simple one dimensional example and offer a short discussion of the order of the phase transition underlying the kinetics. We proceed in

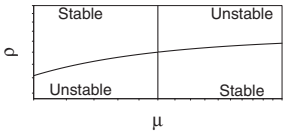

FIG. 1. Sketch of a stability diagram for the growth rate of a sharp interface separating two solid materials. The axes show relative values of the shear modulus and density of the phases. As will be shown in Sec. III, the symmetry of the diagram is broken by the values of Poisson's ratios.

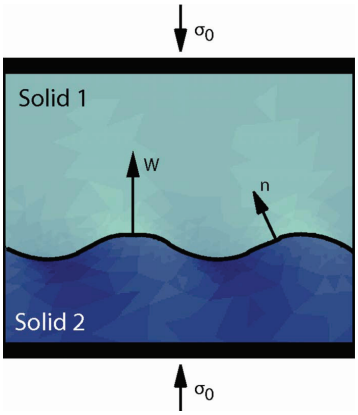

FIG. 2. (Color online) Two solids separated by a sharp interface. A compressional force is applied at the margins in the vertical direction

Sec. III with a linear stability analysis of the full two-dimensional problem. In two dimensions, the phase transformation kinetics gives rise to the development of complex patterns along the phase boundary. While we solve the problem analytically for small perturbations of a flat interface, things become more complicated in the non-linear regime, and we resort to numerical simulations based on the combination of a Galerkin finite element discretization with a level-set method for tracking the phase boundary. In Sec. IV, numerical results are presented together with discussions. Finally in Sec. V we offer concluding remarks.

II. GENERAL PHASE TRANSFORMATION KINETICS

Although the equations that we derive for the exchange of a mass element between two solid phases in a nonhydrostatically stressed system apply to more general settings, we limit ourselves to the study of two solids separated by a single sharp interface. The solids are stressed by an external uniaxial load as illustrated in Fig. 2. In the referential configuration, a solid phase is assumed to have a homogenous mass density, ρ^0, defined per unit undeformed volume occupied by that phase. After the deformation, the densities are functions of space x and time t, i.e., $\rho_1(x,t)$ and $\rho_2(x,t)$. The average density of the two-phase system is denoted by $\rho(x,t)$. Finally, the mass fraction for phase 1 is denoted by c. In this notation, the mass fraction of phase 2 becomes $1-c$.

For nonvanishing densities, the mass-averaged velocity is defined as

$$\bar{v} = cv_1 + (1-c)v_2. \tag{1}$$

Throughout the text, the mass average of any quantity is indicated by a bar. Similarly, the average specific free energy density is given by

$$\bar{f} = cf_1 + (1-c)f_2. \tag{2}$$

The total specific volume is related to the real densities in the deformed state $\rho_1(x,t)$ and $\rho_2(x,t)$ by

$$\rho^{-1} = c\rho_1^{-1} + (1-c)\rho_2^{-1}. \tag{3}$$

The interface separating the two phases is tracked by the zero level of a scalar field $\phi(x,t)$ passively advected according to the equation

$$\frac{\partial \phi}{\partial t} + W|\nabla \phi| = 0, \tag{4}$$

where W is the normal velocity of the surface. It follows that the interface is given by the zero level set

$$\Gamma = \{x | \phi(x,t) = 0, \text{for all } t\}. \tag{5}$$

The scalar field is constructed such that phase 1 occupies the domain in which $\phi(x,t) > 0$ and phase 2 occupies the domain in which $\phi(x,t) < 0$, see Fig. 2. In this notation, the mass fraction may be expressed as the characteristic function of the scalar field

$$c(x,t) = H[\phi(x,t)] = \begin{cases} 1, & \text{if } \phi(x,t) > 0, \\ \frac{1}{2}, & \text{if } \phi(x,t) = 0, \\ 0, & \text{otherwise.} \end{cases} \tag{6}$$

In the subsequent analysis, we make use of the following relations (see, e.g., Ref. [12])

$$\nabla_i c = n_i \delta_\Gamma, \quad \partial_t c = -W\delta_\Gamma, \tag{7}$$

where $n_i = \nabla_i \phi / |\nabla \phi|$ is the normal unit vector of the interface, $W = -\partial_t \phi / |\nabla \phi|$ is the normal velocity, and $\delta_\Gamma = |\nabla \phi| \delta(\phi)$ is the surface delta function. Taking the gradient of the averaged velocity from Eq. (1) and using the above identities, the following relation is obtained

$$\nabla_i \bar{v}_j = \frac{\partial \bar{v}_j}{\partial c} \nabla_i c + c\nabla_i v_{1,j} + (1-c)\nabla_i v_{2,j},$$

$$= \frac{\partial \bar{v}_j}{\partial c} n_i \delta_\Gamma + \overline{\nabla_i v_j}. \tag{8}$$

:

A. Kinetics of the phase transformation

The system must satisfy fundamental conservation principles for the mass, momentum, energy and entropy. Let us denote the material time derivative with respect to the mass-averaged velocity by an over dot, i.e., $\dot{\Theta} = \partial_t \Theta + \bar{v}_i \nabla_i \Theta$. Then, the local mass conservation can be written in the form

$$\dot{\rho} = -\rho \nabla_i \bar{v}_i \tag{9}$$

and the local momentum balance can be written in the form

$$\rho \dot{\bar{v}}_i = \nabla_j \sigma_{ij}, \tag{10}$$

where σ_{ij} is the stress tensor.

The mass fraction of phase 1 satisfies the advection-reaction equation given by

$$\rho\dot{c} = Q\delta_\Gamma, \tag{11}$$

where the mass exchange rate Q is confined to the interface by the delta function (in the sharp interface limit). Mass transport by diffusion is negligible in the reaction dominated regime. This is a valid approximation when the characteristic length $l=\mathcal{D}/\mathcal{W}$, where $\mathcal{D}$ is the diffusion coefficient and W is the velocity of the interface, is small compared with other relevant microscopic length scales. That is material diffusion occurs on a time scale much longer than any other relevant time scale in the system or equivalently the characteristic length scale formed from the diffusion constant and solidification or precipitation rate is small compared to other relevant microscopic scales.

In the linear kinetics, the mass exchange rate is now derived from the requirement that the entropy production has a positive quadratic form. We start by expressing the conservation of specific energy density e in the form

$$\rho\dot{\bar{e}} = \sigma_{ij}\nabla_i\bar{v}_j, \tag{12}$$

where $\bar{v}^2 = cv_1^2 + (1-c)v_2^2$ since the cross term vanishes in the limit of a sharp interface.

At equilibrium

$$\bar{e} = \bar{f} + T\bar{s}, \tag{13}$$

where the free energy is assumed to be a function of the local strain and the composition, i.e., $\bar{f}=\bar{f}(\bar{\epsilon}_{ij},c)$. By inserting the energy conservation equation (12) into the time derivative of this equation, under constant temperature conditions, the expression

$$\rho T\dot{\bar{s}} = \sigma_{ij}\nabla_i\bar{v}_j - \rho\frac{\partial\bar{f}}{\partial\bar{\epsilon}_{ij}}\dot{\bar{\epsilon}}_{ij} - \rho\frac{\partial\bar{f}}{\partial c}\dot{c} \tag{14}$$

is obtained. The phase transformation is assumed to be slow and isothermal. From Eqs. (2) and (8) it follows that

$$\rho T\dot{\bar{s}} = \sigma_{nj}\frac{\partial\bar{v}_j}{\partial c}\delta_\Gamma + \sigma_{ij}\overline{\nabla_i v_j} - \rho\frac{\partial\bar{f}}{\partial\bar{\epsilon}_{ij}}\dot{\bar{\epsilon}}_{ij} - \frac{\partial f}{\partial c}\rho\dot{c}. \tag{15}$$

Given that the strain rate is $\dot{\epsilon}_{ij}=1/2(\nabla_i v_j+\nabla_j v_i)$ and using the symmetry of the stress tensor, we arrive at the expression

$$\rho T\dot{\bar{s}} = \sigma_{nj}\frac{\partial\bar{v}_j}{\partial c}\delta_\Gamma + \left(\sigma_{ij} - \rho\frac{\partial\bar{f}}{\partial\bar{\epsilon}_{ij}}\right)\dot{\bar{\epsilon}}_{ij} - \frac{\partial f}{\partial c}Q\delta_\Gamma, \tag{16}$$

where $\sigma_{nj}=\sigma_{ij}n_i$ is the stress vector at the interface. From Eqs. (8) and (9) and using an equation of state of the form $\rho(\bar{\epsilon}_{ij},c)=\rho^0(c)(1-\bar{\epsilon}_{ii})$ it follows that

$$\begin{aligned}
&\frac{\partial\rho}{\partial c}\dot{c} + \frac{\partial\rho}{\partial\bar{\epsilon}_{ij}}\dot{\bar{\epsilon}}_{ij} = -\frac{\partial v_n}{\partial c}\rho\delta_\Gamma - \rho\overline{\nabla_i v_i} \\
&\Rightarrow \frac{1}{\rho}\frac{\partial\rho}{\partial c}Q\delta_\Gamma - \rho^0\dot{\bar{\epsilon}}_{ii} \\
&= -\frac{\partial v_n}{\partial c}\rho\delta_\Gamma - \rho\overline{\nabla_i v_i} \\
&\Rightarrow \frac{\partial}{\partial c}\left(\frac{1}{\rho}\right)Q = \frac{\partial v_n}{\partial c}, \quad \rho^0\dot{\bar{\epsilon}}_{ii} \approx \rho\overline{\nabla_i v_i}.
\end{aligned}$$

Using Eq. (3) for the density, the jump in the material velocity is related to the reaction rate by

$$\frac{\partial v_n}{\partial c} = Q\frac{\partial}{\partial c}\left(\frac{1}{\rho}\right). \tag{17}$$

The direction of the kinetics is constrained by the second law of thermodynamics which can be expressed in the continuum form as

$$\dot{\bar{\rho s}} + \nabla_i J_i^s = \Pi_s, \tag{18}$$

where J_i^s is the entropy flux density and $\Pi_s \geqslant 0$ is the entropy production rate. We consider the case where the entropy flux is negligible (in the absence of mass and heat fluxes) and therefore set $J_s=0$. Combining Eqs. (16) and (18), it can be seen that the positive entropy production rate leads to the condition

$$\left[\sigma_{nn}\frac{\partial}{\partial c}\left(\frac{1}{\rho}\right) - \frac{\partial\bar{f}}{\partial c}\right]Q\delta_\Gamma + \left(\sigma_{ij} - \rho\frac{\partial\bar{f}}{\partial\bar{\epsilon}_{ij}}\right)\dot{\bar{\epsilon}}_{ij} = T\Pi_s \geqslant 0 \tag{19}$$

on the reaction rate. We now define a constitutive relation that couples the stress to the strain via the Helmholtz free energy

$$\sigma_{ij} = \rho\frac{\partial\bar{f}}{\partial\bar{\epsilon}_{ij}}. \tag{20}$$

From Eq. (19) we observe that the entropy is produced only at the interface, and in the linear kinetics regime the reaction rate is proportional to (see, e.g., Ref. [13]),

$$Q \approx K\left[\sigma_{nn}\frac{\partial}{\partial c}\left(\frac{1}{\rho}\right) - \frac{\partial\bar{f}}{\partial c}\right], \tag{21}$$

where $K>0$ is a system specific constant.

The normal velocity of a sharp interface is obtained by integrating Eq. (11) across the interface and taking the singular part of it

$$W \approx \bar{v}_n - \frac{K}{\rho}\left[\!\left[\sigma_{nn}\frac{1}{\rho} - f\right]\!\right]. \tag{22}$$

Here we introduce the jump in the quantity a from one phase to another $[\![a]\!] := a_1 - a_2$, where a_i is the value of a_i in phase i outside the interface zone as the interface is approached. The additional interfacial jump conditions of the total mass and force balance from Eqs. (9) and (10) are given by

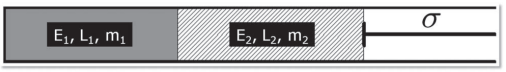

FIG. 3. One-dimensional system undergoing phase transformation.

$$[\![\rho(W-v_n)]\!]=0, \tag{23}$$

$$[\![\sigma_{ij}n_j]\!]=0. \tag{24}$$

In general, surface energy γ and surface stresses may have an important effect on the kinetics at the phase boundary with high curvature $\mathcal{K}$, therefore the expressions given above are modified to take this into account. For this purpose we utilize the Cahn-Hilliard formalism [14] of a diffuse interface. The surface energy is obtained by allowing the Helmholtz free energy density to be a function of the mass fraction gradients, i.e.,

$$\rho\bar{f}(\bar{\epsilon}_{ij},c,\nabla c)=\rho\bar{f}_0(\bar{\epsilon},c)+\frac{\kappa_1}{2}|\nabla c|^2, \tag{25}$$

where κ_1 is a small parameter related to the infinitesimal thickness of the interface and $\bar{f}_0$ is the homogenous free energy density introduced above. Because the composition gradient is small everywhere except for a thin zone at the interface, the free energy can be separated into bulk and surface contributions. If we now take the limit of vanishing surface thickness and follow the derivations in the appendixes we obtain the general jump condition for the normal force vector

$$[\![\sigma_{nn}]\!]=-2\mathcal{K}\gamma. \tag{26}$$

In the aforementioned expression of the interfacial velocity Eq. (22) the normal stress vector was continuous across the interface. In the presence of surface tension, the normal velocity is altered by an additional contribution from the surface energy

$$W\approx v_{1,n}+\frac{K}{\rho_1}([\![f]\!]-\langle\sigma_{nn}\rangle[\![\rho^{-1}]\!]+2\mathcal{K}\gamma\langle\rho^{-1}\rangle), \tag{27}$$

where we have used the interface average defined as $\langle a\rangle = 1/2(a_1+a_2)$.

B. Example: Phase transformation kinetics in a one-dimensional system

We start out considering the phase transformation kinetics of a one-dimensional system composed of two linear elastic solids separated by a single interface. A force σ is applied at the boundary of the system (see Fig. 3) and each solid phase is represented by its Young's modulus E_i $(i=1,2)$, undeformed density ρ_i^0, and length L_i^0. In the deformed state when the external force is applied the length becomes $L_i=L_i^0(1+\sigma/E_i)$ and the density $\rho_i=\rho_i^0L_i^0/L_i$. The specific free energy is given by

$$f=\frac{\sigma^2}{2}\left(\frac{c}{\rho_1(E_1+\sigma)}+\frac{1-c}{\rho_2(E_2+\sigma)}\right). \tag{28}$$

In the following, we do not allow new phases to nucleate within the solids and limit our considerations to the propagation of a single interface separating the solids. The system is assumed to be isothermal and no diffusion of mass takes place. The interface moves as one phase, slowly transforms into the other and an amount $\rho_1 dL_1$, of solid 1 is replaced by an amount $\rho_2 dL_2$ of solid 2, with conservation of the total mass. The phase transformation is assumed to be irreversible and to occur on time scales that are much larger than the time it takes for the system to relax mechanically under the deformational stresses.

In the one-dimensional setting the local mass exchange rate is given by a linear kinetic equation (21) of the form

$$\dot{m}_1=-K\left[\!\!\left[\frac{\sigma^2}{2\rho^0E}-\frac{\sigma}{\rho}\right]\!\!\right]=K\left[\!\!\left[\frac{\sigma^2}{2\rho^0E}+\frac{\sigma}{\rho^0}\right]\!\!\right], \tag{29}$$

with $K>0$. In most cases, the contribution from the jump in the elastic energy density will be small compared to the contribution from the work term (because $\sigma/E\ll 1$, within the linear elasticity regime). The change in the total length will in general follow the sign of the stress

$$\dot{L}=\dot{L}_1\left(1-\frac{\rho_1}{\rho_2}\right)=\dot{m}_1\left[\!\!\left[\frac{1}{\rho}\right]\!\!\right]=K\left[\!\!\left[\frac{\sigma^2}{2E\rho^0}+\frac{\sigma}{\rho^0}\right]\!\!\right]\left[\!\!\left[\frac{1}{\rho^0}+\frac{\sigma}{E\rho^0}\right]\!\!\right].$$

If the densities in the undeformed states are identical, $\rho_1^0=\rho_2^0$, the change in the total length is given by

$$\dot{L}=K\frac{\sigma^3}{2\rho^0}\left[\!\!\left[\frac{1}{E}\right]\!\!\right]^2, \tag{30}$$

whereas a jump in the referential densities $(\rho_1^0\neq\rho_2^0)$ will result in a work term given by

$$\dot{L}\approx K\sigma\left[\!\!\left[\frac{1}{\rho^0}\right]\!\!\right]^2. \tag{31}$$

Under a compressional load, the dense phase grows at the expense of the less dense phase (if the two phases have the same Young's modulus) and the soft phase grows at the expense of the hard phase (if the two phases have the same density), such that overall the system responds to the external force by shrinking. The one-dimensional model cannot predict the morphological stability of the propagating phase boundary in two dimensions. It turns out that the work term destabilizes the propagating boundary under a compressional load.

C. First- and second-order phase transitions: Equilibrium phase diagrams

In the above derivations, the reaction rate is determined by the jump in the Gibbs potential across the phase boundary. Whenever the system is stressed, only one of the two phases will be stable, i.e., the general two phase system will always evolve to an equilibrium state consisting of a single phase. In the absence of an external stress, it is possible for two phases to coexist without any phase transformation tak-

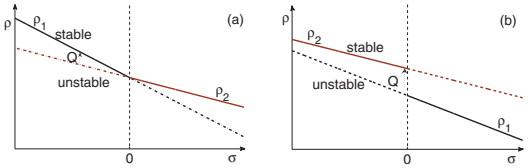

FIG. 4. (Color online) Part (a) illustrates the phase diagram for a second-order phase transition in the ρ-σ plane. The solid-solid kinetics will always be directed from the unstable phase (dashed line) to the stable phase as illustrated by reaction path Q marked by the dashed arrow. The slopes of the densities with respect to stress are Young's modules of the materials. Part (b) illustrates the equilibrium curves of the first order phase transition. For the first order phase transition one would in general expect to see hysteresis effects extending the continuous lines (stable regions) beyond the point $\sigma=0$. Here we have shown an idealized case where such effects are disregarded.

ing place. In the one-dimensional example, the relevant field variable is the stress σ applied to the system and the Gibbs potential is given by [follows from Eq. (29)]

$$g(\sigma) = \frac{\sigma^2}{2\rho^0 E} - \frac{\sigma}{\rho}. \tag{32}$$

In Fig. 4 we show an equilibrium phase diagram in the conjugate pair of variables σ and $1/\rho$. If the derivative of the Gibbs potential with respect to the external field σ is evaluated at the critical point $\sigma=0$, it can be seen that there are two possible scenarios. The first scenario is a first order phase transition, which occurs whenever there is a jump in the referential densities, i.e., the derivative of the Gibbs potential is discontinuous and the second derivative diverges at the critical point. The other scenario is a second-order phase transition, which occurs when the referential densities of the two phases are identical. We then have a jump in the second-order derivative whenever Young's modules of the two phases are dissimilar.

The order of the phase transition has a fundamental impact on the dynamics. In two dimensions a first-order phase transition kinetics will generally lead to morphological instabilities of the propagating phase boundary while a second order phase transition will either flatten or roughen the boundary depending on Poisson's ratios of the two materials. In the next section we analyze the different phase transitions by performing a linear stability analysis.

III. LINEAR PERTURBATION ANALYSIS

We now solve the elastostatic Eqs. (10) and (26) together with the kinetics Eqs. (22) and (27) in two dimensions for an arbitrary perturbation to an initially flat interface using the quasistatic version of momentum balance in Eq. (10). In addition to the translational dynamics observed in the one-dimensional system presented above, it turns out, that in two dimensions the interface dynamics is nontrivial and may lead to the formation of fingerlike structures. The general setup is shown in Fig. 2, where phase i, $i=1,2$, has material parameters μ_i, ν_i, and ρ_i, with μ_i being the shear modulus and ν_i being the Poisson's ratio. In general, the interface velocity depends on its morphology, the 6 material parameters and the external loading σ_∞. One degree of freedom is removed by rescaling the shear modulus of one phase with the external load.

A. Stress field around a perturbed flat interface

In order to evaluate the jump in Gibbs energy density, i.e., $[\![\mathcal{F}/\rho^0+\mathcal{W}]\!]$, we need to determine the stress field around the interface by solving the elastostatic equations. We have that under plane stress conditions, the local strain energy density can be written in the form

$$\mathcal{F} = \frac{1}{4\mu}\left(\sigma_{xx}^2 + \sigma_{yy}^2 - \frac{\nu}{1+\nu}(\sigma_{xx}+\sigma_{yy})^2 + 2\sigma_{xy}^2\right) \tag{33}$$

and the work term is defined as

$$\mathcal{W} = -\sigma_{nn}\rho_i^{-1} = -\sigma_{nn}\rho_{i,0}^{-1}[1+\mathrm{Tr}(\epsilon)]. \tag{34}$$

The trace of strain is given in terms of stress by

$$\mathrm{Tr}(\epsilon) = \frac{1-2\nu}{2\mu(1+\nu)}(\sigma_{xx}+\sigma_{yy}). \tag{35}$$

Note that we could as well have formulated the problem under plane strain conditions; however, the generic behavior in both plane stress and strain is the same although the detailed dependence on the material parameters is altered.

We solve the mechanical problem by finding the Airy stress function $U(x,y)$ [15] which satisfies the biharmonic equation $\Delta^2 U=0$. Once the stress function has been found, the stress tensor components readily follow from the relations

$$\sigma_{xx} = \frac{\partial^2 U}{\partial y^2}, \quad \sigma_{yy} = \frac{\partial^2 U}{\partial x^2}, \quad \sigma_{xy} = -\frac{\partial U}{\partial x \partial y}. \tag{36}$$

The biharmonic equation is solved under the boundary conditions of a normal load applied in the y direction at infinity, i.e., $\sigma_{yy} \to -|\sigma_\infty| < 0$ and $\sigma_{xy}=0$ for $y \to \pm\infty$. The continuity of the stress vector across the interface follows from force balance. In addition we require that $u_x(\pm\infty, y)=0$.

For a flat interface, the stress field is homogenous in space. This implies that the Airy stress function is quadratic in x and y, with coefficients determined by the boundary conditions. With the boundary conditions specified above, the stress function for the ith phase can be written in the form

$$U_i(x,y) = \frac{|\sigma_\infty|}{2}(x^2 + \nu_i y^2). \tag{37}$$

From this stress function we can calculate the Gibbs potential which in the case of dissimilar phases is discontinuous across the interface. The velocity of the phase transformation readily follows from the potential

$$W_0 \propto [\![\mathcal{F}_0/\rho^0 + \mathcal{W}_0]\!] = |\sigma_\infty|\left(\frac{1}{\rho_1^0} - \frac{1}{\rho_2^0}\right) - \frac{|\sigma_\infty|^2}{4}\left(\frac{1-3\nu_1}{\rho_1^0\mu_1} - \frac{1-3\nu_2}{\rho_2^0\mu_2}\right). \quad (38)$$

The subscript of the free energy density and the work term refers to an unperturbed interface. From the above equation, we see that when the lower phase is much denser than the upper phase, i.e., $\rho_1^0 \ll \rho_2^0$, the interface propagates uniformly into the upper phase with a velocity $W \approx |\sigma_\infty|[\![1/\rho]\!] > 0$, i.e., the denser phase grows into the softer. When the densities are identical or almost identical, $\rho_2/\rho_1 \approx 1$ and the shear modules significantly different, i.e., $\mu_1 \ll \mu_2$. When the two solids phases have identical Poisson's ratios ν, we see that the softer phase can only grow into the harder one when $\nu < 1/3$.

In the case of an arbitrarily shaped interface separating the two phases, the analytical solution to the stress field is in general far from trivial. In-plane problems can in some cases be solves using conformal mappings or perturbation schemes [15–17]. Here, we solve the stress field around a small undulation of flat interface employing a linear perturbation scheme [17]. In the linear stability analysis we now study the growth of an arbitrary harmonic perturbation with wavelength k, i.e., $h(x,t) = Ae^{\omega t}\cos(kx)$ with $A \ll 1$. In Appendix B, we derive expressions for a general perturbation. The Airy stress function can be written as a superposition of the solution to the flat interface and a small correction due to undulation $U(x,y) = U_0(x,y) + \Theta(x,y)$, where $\Theta(x,y)$ is determined from the interfacial constraints of continuous stress vector and displacement field. When the wave number k is much smaller than the cutoff introduced by the surface tension, we obtain the following expressions for the Airy stress functions:

$$\Theta_1(x,y) = \frac{-|\sigma_\infty|h(x)\exp(-ky)(\alpha_1 y + \beta)}{k(\mu_2\kappa_1 + \mu_1)(\mu_1\kappa_2 + \mu_2)},$$

$$\Theta_2(x,y) = \frac{|\sigma_\infty|h(x)\exp(ky)(\alpha_2 y - \beta)}{k(\mu_2\kappa_1 + \mu_1)(\mu_1\kappa_2 + \mu_2)}, \quad (39)$$

where $\kappa_i = \frac{3-\nu_i}{1+\nu_i}$ and we have introduced the material specific constants

$$\alpha_1 = k(1-\nu_1)(\mu_2 - \mu_1)(\mu_1\kappa_2 + \mu_2),$$

$$\alpha_2 = k(1-\nu_2)(\mu_1 - \mu_2)(\mu_2\kappa_1 + \mu_1),$$

and

$$\beta = 2\mu_1^2\frac{1-\nu_2}{1+\nu_2} - 2\mu_2^2\frac{1-\nu_1}{1+\nu_1} + 4\mu_1\mu_2\frac{\nu_1 - \nu_2}{(1+\nu_2)(1+\nu_1)}.$$

From the Airy stress functions, we then calculate the stress components using Eq. (36) and find the jumps in the Gibbs energy density from Eqs. (33) and (34). The evolution of the shape perturbation relative to a uniform translation of the flat interface is described by Eq. (27), namely,

$$\frac{\partial h(x,t)}{\partial t} \propto [\![\mathcal{F} + \mathcal{W}]\!] - W_0, \quad (40)$$

which in the linear regime corresponds to a dispersion relation given in the general form as

$$\omega \propto \frac{[\![\mathcal{F} + \mathcal{W}]\!] - W_0}{h}. \quad (41)$$

Below follows an evaluation of the growth rate for a small harmonic perturbation to a flat interface. For this perturbation, the general expression for the growth rate follows directly upon insertion of the Airy functions in Eq. (39) and then in Eq. (36), however, the growth rate is not easily expressed in a short and readable form and we have therefore limited our presentation to a few special cases. The growth rate is a function of the six material parameters (ν_i, μ_i, ρ_i) and the external stress. Naturally, the stability of the growing interface is invariant under the interchange of the solid phases and correspondingly the region of the stability diagram that we have to study is reduced.

B. First- and second-order phase transition: Stability diagrams

In the second-order phase transition when both solids have the same referential densities $\rho_1^0 = \rho_2^0 = \rho^0$ and when the Poisson's ratios $\nu_1 = \nu_2 = \nu$ are identical the dispersion relation assumes a simple form

$$\frac{\omega}{k} = \frac{(3\nu-1)(1-\nu)(\mu_1+\mu_2)(\mu_2-\mu_1)^2}{\rho^0\mu_1\mu_2(\mu_1+\mu_2\kappa)(\mu_2+\mu_1\kappa)(1+\nu)}, \quad (42)$$

where κ is the fraction introduced above and k the wave number of the perturbation. The expression reveals an interesting behavior where the interface is stable for Poisson's ratio less than $1/3$ and is unstable for Poisson's ratio larger than $1/3$. Figure 5 shows stability diagrams for the specific case where $\mu_1 = 1$ and $\rho_1^0 = 1$ (in arbitrary units). In panel (A) the diagram is calculated for two solids that have the same Poisson's ratio and with a value $\nu = 1/4$. The second-order phase transition occurs along the horizontal cut $\rho_2^0 = 1$ and is marked by a dashed grey line. We observe that ω/k is negative along this line and the interface is therefore stable. For ν larger than $1/3$ (not shown in the figure) the horizontal zero level curve will flip around and the grey dashed line will then be covered with unstable regions. In order to see this flip, we expand Eq. (41) around the point (1,1), i.e., in terms of $\rho_2^0 - 1$ and $\mu_2 - 1$, and achieve the following expression for the zero curve:

$$\rho_2^0 \approx 1 + \frac{(1-2\nu-3\nu^2)(\mu_2-1)}{\nu(7+\nu)}. \quad (43)$$

Note that the right-hand side is in units of ρ_1. We directly observe that the horizontal zero curve flips around at the critical point $\nu = 1/3$. In the case when the two solids are identical, i.e., at the point (1,1) in the stability diagram, all modes will as expected remain unchanged and the interface therefore remain unaltered. The other parts of the zero levels lead to marginal stability but will in general induce a growth

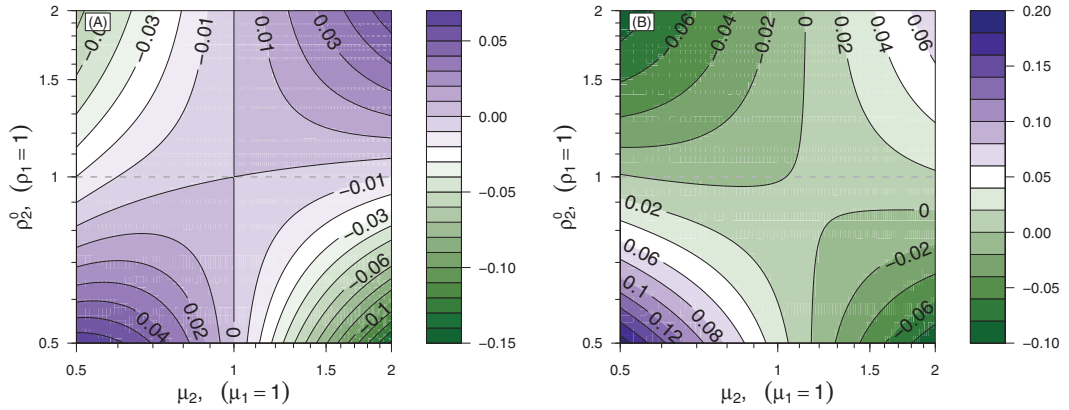

FIG. 5. (Color online) Panel (A), stability diagram for two solids materials with identical Poisson's ratio of ν=0.25. Panel (B), diagram for solids with Poisson's ratios of ν_1=0.45 and ν_2=0.40.

of the interface due to the unperturbed Gibbs potential (38). We now consider a cut in the stability diagram where the two solids have the same shear modules, $\mu_1=\mu_2=\mu$, but different densities and Poisson's ratios. For different Poisson's ratios the dispersion relation (41) becomes

$$\frac{\omega}{k} = \frac{(\nu_2 - \nu_1)[\nu_1\rho_2^0 - \nu_2\rho_1^0 + 2(\rho_2^0 - \rho_1^0)\mu]}{4\rho_1^0\rho_2^0\mu}. \tag{44}$$

From this expression we see that the vertical zero line observed in Eq. (42) and in Fig. 5 panel (A) only exists for identical Poisson's ratios. When the solids have different Poisson's ratios, the separatrix or intersection of the two zero curves located at (1,1) in panel (A) will split into two nonintersecting zero curves. In panel (B) we show a stability diagram for solids with Poisson's ratios ν_1=0.45 and ν_2 =0.40.

In general the stability diagram is characterized by four quadrants, two stable and two unstable, delimited by neutral zero curves. The physical regions would typically correspond to the quadrants I and II under the assumption that higher density implies higher shear modulus. In these quadrants the growth rate is typically positive (i.e., the interface is unstable) except for a thin region at the borderline between a first- and second-order phase transition, i.e., when $\rho_2 \simeq \rho_1$.

IV. NUMERICAL RESULTS AND DISCUSSIONS

The linear stability analysis revealed an intricate change in stability depending on the material properties and densities of the two solids. We explore this stability beyond the linear regime using numerical methods. The bulk elastostatic equation (10) is solved numerically on an unstructured triangular grid using the Galerkin finite element method and the surface tension force is converted to a body force in a narrow band surrounding the interface. The discontinuous jumps appearing in the dynamical Eq. (27) are computed at the outer border of the band. Periodic boundary conditions are used to minimize the possible influence of the finite system size in the x direction (parallel to the interface). The interface is tracked using a level set method (e.g., Ref. [18]) and propagated with the normal velocity calculated in Sec. II using Eq. (27). Several level set functions $\phi(x,t)$ can be used, however, most level set methods use the signed distance function [$|\phi(x,t)|$ is the shortest distance between x and the interface and the sign of $\phi(x,t)$ identifies the phase at position x]. Good numerical accuracy can be obtained by keeping $\phi(x,t)$ a signed distance function at all times, and this is achieved by frequent reinitialization of $\phi(x,t)$ according to the iterative scheme

$$\frac{\partial \phi}{\partial t'} + S(\phi_0)(|\nabla \phi| - 1) = 0, \tag{45}$$

where ϕ_0 is the level set function before the reinitialization, t' is a fictitious time, and $S(\phi_0)=\phi_0/\sqrt{\phi_0^2+(\Delta x)^2}$, where Δx is the grid size. Generally only a couple of iterations are needed at each time step, to obtain a good approximation to a signed distance function, and it is only necessary to update the level set function in a narrow band around the interface.

In Figs. 6 and 7 we present numerical simulations of the phase transformation kinetics using parameter regions where the interface is either stable or unstable. The simulations presented in Fig. 6 [panels (A) and (B)] represent interface snap shots of a first-order phase transition dynamics and panels (C) and (D) simulations of a second order, respectively. In panel (A), the values of the parameters were chosen in a region of the stability diagram where the interface is predicted to roughen and in panel (B) we have used parameters corresponding to a stable evolution of the interface. Note that the interface in both cases is moving from the dense phase into the soft phase independent of its stability. This is in agreement with the one dimensional calculation performed in Sec. II. Panel (C) shows a case of a second-order phase transition where the interface is unstable, while panel (D) shows a stable case. We notice that, for second order phase transitions, the overall translation of the interface is changed in unison with its stability. In Eq. (43) we saw that the stability

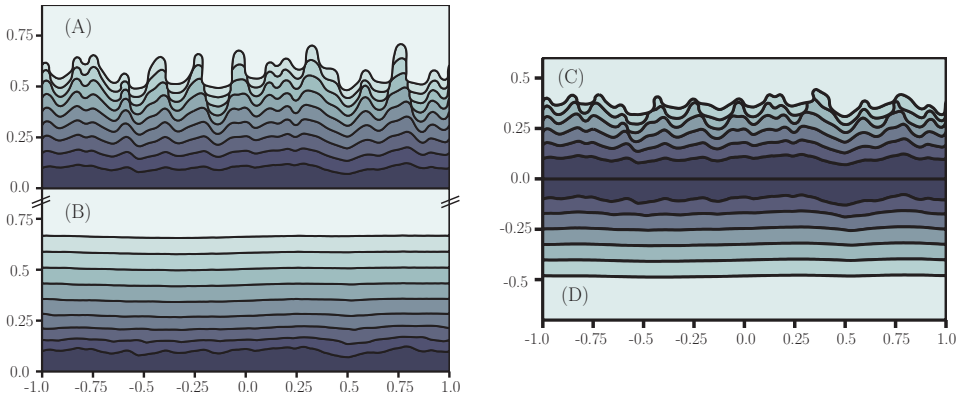

FIG. 6. (Color online) Simulations of the temporal evolution of solid-solid interfaces for first-order [panels (A) and (B)] and second-order [panels (C) and (D)] phase transitions. Panel (A) shows a simulation using $\rho_1=1.0$, $\mu_1=1.0$ and $\rho_2=1.05$, $\mu_2=2.0$. Both phases have identical Poisson's ratio $\nu_1=\nu_2=0.45$. Panel (B) is a simulation run with densities and shear modules similar to panel (A) but with a different Poisson's ratios $\nu_1=\nu_2=0.25$. Panel (C) is a simulation run with $\rho_1=1.0$, $\mu_1=1.0$ and $\rho_2=1.0$, $\mu_2=2.0$. Both phases have identical Poisson's ratios $\nu_1=\nu_2=0.45$. Panel (D) shows a simulation run with densities and shear modules similar to panel (C) but with different Poisson's ratios $\nu_1=\nu_2=0.25$. The color code represents a time arrow pointing from the darker regions (early stage) to the lighter regions (final stage).

of the second-order phase transition is dictated by the values of Poisson's ratios. For Poisson's ratio smaller than $1/3$, the kinetics is stable and the phase of small shear modulus grows into the phase of higher shear modulus while for higher values of Poisson's ratio the behavior is reversed and the interface roughens with time. This also follows from Eq. (38). In Fig. 7, we have plotted the mean velocity as a function of time for the simulations presented in Fig. 6.

V. CONCLUDING REMARKS

In conclusion, it has been shown that the phase transformation of one solid into the another across a thin interface may lead to a morphological instability, as well as the development of fingers along the propagating interface. We have presented a stability analysis based on the Gibbs potential for nonhydrostatically stressed solids and have established a linear relationship between the rate of entropy production at the interface and the rate of mass exchange between the solid phases. The solids are compressed transverse to the interface and corresponding stability diagrams reveal an intricate dependence of the stability on the material density, Poisson's ratio and Young's modulus. With the density as order parameter, two types of phase transitions were considered, a first and a second order, respectively.

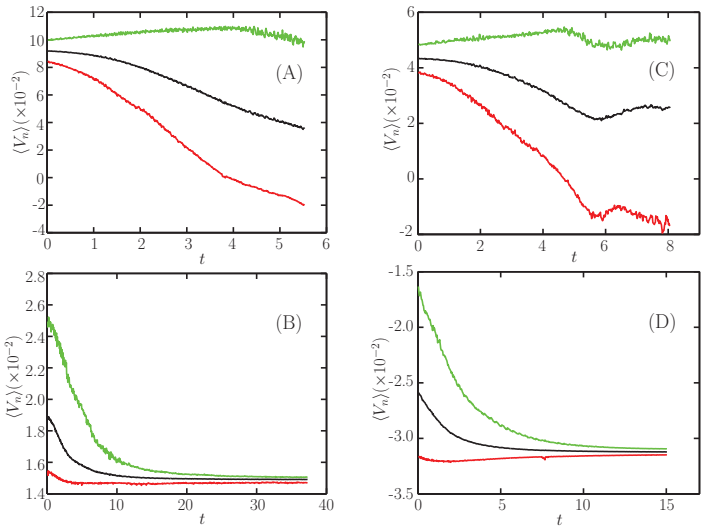

FIG. 7. (Color online) Normal velocity as a function of time in first-order [panels (A) and (B)] and second-order [panels (C) and (D)] phase transitions. The simulations presented in the individual panels are identical to the corresponding panels in Fig. 6. The color code of the curves reference to the mean velocity (in black), the mean of lowest 10% (lower curve) and the mean of the highest 10% (upper curve).

For both types of transitions we find expressions for the curves separating the stable and unstable regions in the stability diagram. For most material parameters the first-order phase transition, i.e., when the two solids have different referential densities, destabilizes the interface by allowing fingers to grow from the denser phase into the other. When the solids have identical or almost identical densities, i.e., a second-order phase transition, we find that the stability depends on Poisson's ratios of the two solids. If the two solids have Poisson's ratios less than $1/3$, the phase transition dynamics of the two solids will lead to a flattening of the interface, i.e., any perturbation of a flat interface will decay and ultimately the interface will propagate uniformly from the soft phase (low Young's modulus) into the hard phase (high Young's modulus). We believe that our classification of the phase transition order together with the stability analysis may find application in many natural systems, since the morphological stability directly provide information about the order of the underlying phase transformation process and the material parameters.

ACKNOWLEDGMENTS

This project was funded by *Physics of Geological Processes*, a Center of Excellence at the University of Oslo. The authors are grateful to R. Fletcher, P. Meakin, Y.Y. Podladtchikov, and F. Renard for fruitful discussions and comments.

APPENDIX A: SURFACE TENSION

In this appendix we present additional details on the derivation of the reaction rate (27) including the interfacial free energy. Let us consider a diffuse interface characterized by a small thickness over which the concentration field varies smoothly between the constant values in the bulk of the two phases. In the Cahn-Hilliard formalism, the free energy is introduced as a function of both the concentration and concentration gradients, and has the form

$$\rho\bar{f}(\bar{\epsilon}_{ij},c,\nabla c)=\rho\bar{f}_0(\bar{\epsilon}_{ij},c)+\frac{\kappa_1}{2}|\nabla c|^2, \tag{A1}$$

where the first term is the free energy in the bulk and the second term is associated with the interfacial free energy. Here κ_1 is a small parameter related to the thickness of the interface.

In this case, the calculation of the reaction rate Q proceeds as in Sec. II. We apply the total time derivative of the local equilibrium equation (13), where the free energy is given by Eq. (A1) and then obtain the following expression:

$$\dot{\bar{e}}=\frac{\partial\bar{f}}{\partial\bar{\epsilon}_{ij}}\dot{\bar{\epsilon}}_{ij}+\frac{\partial\bar{f}}{\partial c}\dot{c}+\frac{\partial\bar{f}}{\partial\nabla_i c}(\nabla_i\dot{c}-\nabla_j c\nabla_i\bar{v}_j)+T\dot{\bar{s}}, \tag{A2}$$

where the commutation relation $\frac{d}{dt}\nabla_i c=\nabla_i\dot{c}-\nabla_i v_j\nabla_j c$ has been used [12]. Combining the above equation with the conservation of energy from Eq. (12) and the entropy balance from Eq. (18) an expression for the entropy production rate is obtained:

$$\begin{aligned}T\Pi_s&=\left(\sigma_{ij}+\rho\nabla_j c\frac{\partial\bar{f}}{\partial\nabla_i c}\right)\nabla_i\bar{v}_j-\rho\left(\frac{\partial\bar{f}}{\partial c}-\nabla_i\frac{\partial\bar{f}}{\partial\nabla_i c}\right)\dot{c}-\rho\frac{\partial\bar{f}}{\partial\bar{\epsilon}_{ij}}\dot{\bar{\epsilon}}_{ij}\\&=n_i\left(\sigma_{ij}+\rho\nabla_i c\frac{\partial\bar{f}}{\partial\nabla_j c}\right)n_jQ\delta_\Gamma\frac{\partial}{\partial c}\left(\frac{1}{\tilde{\rho}}\right)\\&\quad-\left(\frac{\partial\bar{f}}{\partial c}-\nabla_i\frac{\partial\bar{f}}{\partial\nabla_i c}\right)Q\delta_\Gamma+\left(\sigma_{ij}+\rho\nabla_i c\frac{\partial\bar{f}}{\partial\nabla_j c}-\rho\frac{\partial\bar{f}}{\partial\bar{\epsilon}_{ij}}\right)\dot{\bar{\epsilon}}_{ij}.\end{aligned}$$

We observe that Π_s satisfies the second law of thermodynamics provided that the last term vanishes and the rest of the terms are brought into a quadratic form. This implies a constitutive equation for the stress given by

$$\sigma_{ij}=\rho\frac{\partial\bar{f}}{\partial\bar{\epsilon}_{ij}}-\rho\nabla_i c\frac{\partial\bar{f}}{\partial\nabla_j c}, \tag{A3}$$

and a linear kinetics law with the reaction rate being proportional to

$$Q\approx K\left[\rho\frac{\partial\bar{f}_0}{\partial\bar{\epsilon}_{ij}}n_in_j\frac{\partial}{\partial c}\left(\frac{1}{\rho}\right)-\frac{\partial\bar{f}}{\partial c}+\nabla_i\frac{\partial\bar{f}}{\partial\nabla_i c}\right], \tag{A4}$$

where K is a positive local constant of proportionality and σ_{ij}^0 is the elastic stress in the absence of surface tension.

Using Eq. (A1), the two constitutive laws may be expressed as

$$\sigma_{ij}=\sigma_{ij}^0-\kappa_1\nabla_i c\otimes\nabla_j c, \tag{A5}$$

$$Q=K\left[\sigma_{nn}^0\frac{\partial}{\partial c}\left(\frac{1}{\rho}\right)-\frac{\partial\bar{f}_0}{\partial c}+\kappa_1\rho^{-1}\nabla^2 c\right], \tag{A6}$$

where σ_{ij}^0 is the elastic stress obtained in Sec. II without the surface stress.

In the sharp interface limit, i.e., the thickness goes to zero, the surface free energy becomes

$$\rho f^{\mathrm{surf}}=\kappa_1|\nabla c|^2\to\gamma\delta_\Gamma, \tag{A7}$$

and surface stress is related to the surface energy by

$$\sigma_{ij}^{\mathrm{surf}}=\kappa_1|\nabla c|^2\left(1-\frac{\nabla_i\phi}{|\nabla\phi|}\otimes\frac{\nabla_j\phi}{|\nabla\phi|}\right)\to\gamma(1-n_i\otimes n_j)\delta_\Gamma. \tag{A8}$$

The divergence of the surface stress is then calculated as

$$\nabla_i\sigma_{ij}^{\mathrm{surf}}=2\mathcal{K}\gamma n_j\delta_\Gamma, \tag{A9}$$

where $\mathcal{K}$ is the local curvature.

APPENDIX B: GOURSAT FUNCTIONS AROUND A PERTURBED FLAT INTERFACE

In this appendix, we explain in details how to calculate the Airy stress functions around the perturbed flat interface introduced in Sec. III. All the detailed calculations were carried out in MAPLE in order to handle the lengthy algebraic expressions.

The Airy stress function satisfies the biharmonic equation $\partial_z^2\partial_{\bar{z}}^2 U=0$. This equation has a general solution which can be written in the Goursat form $U(z,\bar{z})=\mathrm{Re}\{\bar{z}\phi(z)+\chi(z)\}$, where $\varphi(z)$ and $\chi(z)$ are complex functions determined by the boundary conditions. Combining Eq. (36) with the Goursat solution, stress components are related to these functions by the following expressions:

$$\sigma(z)=\sigma_{xx}(x,y)+\sigma_{yy}(x,y)=2\{\varphi'(z)+\overline{\psi'}(z)\}, \quad \text{(B1)}$$

$$\Sigma(z)=\sigma_{yy}(x,y)-\sigma_{xx}(x,y)+2i\sigma_{xy}(x,y)=2\{\bar{z}\varphi''(z)+\psi(z)\}, \quad \text{(B2)}$$

where $\varphi(z)=\chi'(z)$. The solution to the biharmonic equation is determined up to a linear gauge transformation

$$\varphi(z)\mapsto\varphi(z)+Ciz+p, \quad \text{(B3)}$$

$$\psi(z)\mapsto\psi(z)+q, \quad \text{(B4)}$$

where C is a real number and p, q are arbitrary complex numbers.

The boundary conditions are given by the far-field stresses and the constraints at the interface. Here we consider that the system is loaded by a uniaxial compression in the y direction, $\sigma_{yy}(x,\infty)=-|\sigma_\infty|<0$. Whenever the two phases are different an interface is introduced at which we require force balance and continuous displacement field. The force balance is expressed by the following jump condition:

$$[\![\sigma_{xx}n_x+\sigma_{xy}n_y+i(\sigma_{yx}n_x+\sigma_{yy}n_y)]\!]=-\gamma\mathcal{K}(n_x+in_y),$$

where $\mathcal{K}$ is the local curvature and γ is the surface tension. From Eqs. (B1) and (B2) we find that the force balance leads to the following condition on the Goursat functions:

$$[\![\varphi+z\overline{\varphi'}+\bar{\psi}]\!]=i\int_0^s\gamma\mathcal{K}(n_x+in_y)ds, \quad \text{(B5)}$$

where s is a point at the interface. The continuity of the displacement field across the interface introduces an additional jump condition given by

$$\left[\!\!\left[\frac{1}{\mu}(-\kappa\varphi+z\overline{\varphi'}+\bar{\psi})\right]\!\!\right]=0, \quad \text{(B6)}$$

where μ is the shear modulus and $\kappa=\frac{3-\nu}{1+\nu}$ is a constant for in-plane stress-elasticity determined by the Poisson's ratio.

The two jump conditions (B5) and (B6) combined with the far-field boundary conditions $\varphi_\infty(z)=-\frac{1}{4}(1+\nu)|\sigma_\infty|z$ and $\psi_\infty(z)=-\frac{1}{2}(1-\nu)|\sigma_\infty|z$ are sufficient to determine the fields $\varphi_1(z)$, $\psi_1(z)$, $\varphi_2(z)$, and $\psi_2(z)$. Superimposing an arbitrary perturbation with amplitude $h(x)$ on the flat interface, the Goursat functions are slightly altered. They can be expanded to linear order in $h(x)$ as follows [17]:

$$\varphi(x)\approx\varphi_0(x)+ih(x)\varphi_0'(x)+\Phi(x), \quad \text{(B7)}$$

$$\psi(x)\approx\psi_0(x)+ih(x)\psi_0'(x)+\Psi(x). \quad \text{(B8)}$$

$\Phi(x)$ and $\Psi(x)$ are functions of $h(x)$. Inserting this expansion into Eqs. (B6) and (B5), we obtain that the corresponding jump conditions for the perturbation fields

$$[\![\Phi(x)+x\overline{\Phi'}(x)+\bar{\Psi}(x)]\!]=ih(x)[\![\overline{\Sigma_0}(x)]\!]+f(x), \quad \text{(B9)}$$

$$\left[\!\!\left[\frac{-\kappa\Phi(x)+x\overline{\Phi'}(x)+\bar{\Psi}(x)}{\mu}\right]\!\!\right]=ih(x)\left[\!\!\left[\frac{\overline{\Sigma_0}(x)}{\mu}\right]\!\!\right], \quad \text{(B10)}$$

where $f(x)=i\int_0^x\gamma\mathcal{K}(n_x+in_y)ds$. To linear order we find that $f(x)\approx-\gamma\int_0^x h''(s)ds$. Eqs. (B9) and (B10) can be rewritten equivalently as

$$\Phi_1(x)-\Omega(x\overline{\Phi_1'(x)}+\overline{\Psi_1(x)})-(1+\Lambda)\Phi_2(x)=-i\Omega h(x)\bar{\Sigma}_{01}(x)+\frac{1+\Lambda}{1+\kappa}f(x), \quad \text{(B11)}$$

$$\Phi_2(x)-\Pi(x\overline{\Phi_2'(x)}+\overline{\Psi_2(x)})-(1+\Delta)\Phi_1(x)=-i\Pi h(x)\bar{\Sigma}_{02}(x)-\frac{1+\Delta}{1+\kappa}f(x). \quad \text{(B12)}$$

The constants appearing above are expressed in terms of the elastic moduli. Adopting the notation of Ref. [17], these are given by

$$\Lambda=\kappa\frac{1/\mu_2-1/\mu_1}{1/\mu_2+\kappa/\mu_1}, \quad \Pi=\frac{1/\mu_2-1/\mu_1}{\kappa/\mu_2+1/\mu_1}, \quad \text{(B13)}$$

$$\Delta=\kappa\frac{1/\mu_1-1/\mu_2}{\kappa/\mu_2+1/\mu_1}, \quad \Omega=\frac{1/\mu_1-1/\mu_2}{\kappa/\mu_1+1/\mu_2}. \quad \text{(B14)}$$

Equations (B11) and (B12) are solved at an arbitrary point z in the complex plane by applying the Cauchy integral and using the analytic continuation of each function [15]. Let us denote the Cauchy integral over the perturbation amplitude

$$H_1(z)=\frac{1}{2\pi i}\int\frac{h(x)}{x-z}dx, \quad \text{with } \mathrm{Im}(z)>0, \quad \text{(B15)}$$

$$H_2(z)=\frac{1}{2\pi i}\int\frac{h(x)}{x-z}dx, \quad \text{with } \mathrm{Im}(z)<0. \quad \text{(B16)}$$

Notice that the two functions satisfy the following relations:

$$\overline{H_1(\bar{z})}=-H_2(z), \quad \overline{H_2(\bar{z})}=-H_1(z)$$

$$\mathrm{Im}(H_1(x))=\mathrm{Im}(H_2(x)), \quad \mathrm{Re}(H_1(x))=-\mathrm{Re}[H_2(x)],$$

where the principal value of the Cauchy integral is considered when x is a point on the real axis.

Thus, by applying the Cauchy integral with $\mathrm{Im}(z)>0$ in Eq. (B11) and $\mathrm{Im}(z)<0$ in Eq. (B12), Φ_1 and Ψ_2 are determined in the integral form as follows:

$$\Phi_1(z) = -i\Omega\Sigma_{0,1}H_1(z) + \frac{1+\Lambda}{1+\kappa}F_1(z)$$

$$\Phi_2(z) = i\Pi\Sigma_{0,2}H_2(z) + \frac{1+\Delta}{1+\kappa}F_2(z),$$

where

$$F'(z) = \frac{1}{2\pi i}\int \frac{f'(x)}{x-z}dx \approx -\gamma\frac{d^2}{dz^2}H(z). \quad \text{(B17)}$$

$\Psi_1(z)$ is calculated from the complex conjugation of Eq. (B11) when the Cauchy integral is applied on both sides of the equation and $\mathrm{Im}(z)>0$. In a similar manner, $\Phi_2(z)$ is derived from Eq. (B12). The final expressions for the two functions then follow:

$$\Psi_1(z) = -i\Sigma_{0,1}H_1(z) - \frac{1+\Lambda}{1+\kappa}\left(-i\Pi\Sigma_{0,2}H_1(z) - \frac{1+\Delta}{1+\kappa}F_1(z)\right) - \frac{1+\Lambda}{\Omega(1+\kappa)}F_1(z) - z\Phi_1'(z),$$

$$\Psi_2(z) = i\Sigma_{0,2}H_2(z) - \frac{1+\Delta}{\Pi}\left(i\Omega\Sigma_{0,1}H_2(z) - \frac{1+\Lambda}{1+\kappa}F_2(z)\right) - \frac{1+\Delta}{\Pi(1+\kappa)}F_2(z) - z\Phi_2'(z).$$

For a cosine perturbation of the interface, $h(x)=A\cos(kx)$, with $A \ll 1$ the Airy stress function, $U(x,y)=\mathrm{Re}\{\bar{z}\phi(z)+\chi(z)\}$ is obtained explicitly.

[1] R. J. Asaro and W. A. Tiller, Metall. Trans. **3**, 1789 (1972).
[2] M. A. Grinfeld, Dokl. Akad. Nauk SSSR **290**, 1358 (1986).
[3] H. Gao and W. D. Nix, Annu. Rev. Mater. Sci. **29**, 173 (1999).
[4] D. J. Srolovitz, Acta Metall. **37**, 621 (1989).
[5] W. Mullins, J. Appl. Phys. **28**, 333 (1957).
[6] P. Meakin, *Fractals, Scaling and Growth Far From Equilibrium* (Cambridge University Press, Cambridge, 1998).
[7] P.-Y. Robin, Am. Mineral. **59**, 1286 (1974).
[8] F. C. Larche and J. W. Cahn, Acta Metall. **26**, 1579 (1978).
[9] W. B. Kamb, J. Geology **67**, 153 (1959).
[10] R. C. Fletcher, J. Geophys. Res. **78**, 7661 (1973).
[11] L. Angheluta, E. Jettestuen, J. Mathiesen, F. Renard, and B. Jamtveit, Phys. Rev. Lett. **100**, 096105 (2008).
[12] J. Lowengrub and L. Truskinovsky, Proc. R. Soc. London, Ser. A **454**, 2617 (1998).
[13] M. E. Gurtin, Arch. Ration. Mech. Anal. **123**, 305 (1993).
[14] J. W. Cahn and J. E. Hilliard, J. Chem. Phys. **28**, 258 (1958).
[15] N. I. Muskhelishvili, *Some Basic Problems of the Mathematical Theory of Elasticity*, 3rd ed. (Noordhoff, Groningen, 1953).
[16] J. Mathiesen, I. Procaccia, and I. Regev, Phys. Rev. E **77**, 026606 (2008).
[17] H. Gao, Int. J. Solids Struct. **28**, 703 (1991).
[18] J. A. Sethian, *Level Set Methods and Fast Marching Methods*,2nd ed. (Cambridge University Press, Cambridge, 1999).

Appendix C

Paper III

Morphological instabilities of stressed and reactive geological interfaces

---

submitted to Journal of Geophysical Research

Morphological instabilities of stressed and reactive geological interfaces

Luiza Angheluta,[1] Joachim Mathiesen,[1,2] Chaouqi Misbah,[3] and François Renard[1,4]

Luiza Angheluta, Physics of Geological Processes, University of Oslo, box 1047, *0316* Blindern, Norway

Joachim Mathiesen, Physics of Geological Processes, University of Oslo, box 1047, *0316* Blindern, Norway

Chaouqi Misbah, University Joseph Fourier - Grenoble I / CNRS, LSP, BP *53*, *F-38041* Grenoble, France

François Renard, University Joseph Fourier - Grenoble I / CNRS / OSUG, LGCA, BP *53*, *F-38041* Grenoble, France

[1]Physics of Geological Processes, University of Oslo, Norway.

[2]Niels Bohr Institute, University of Copenhagen, Denmark

[3]University Joseph Fourier - Grenoble I / CNRS, LSP, Grenoble, France.

[4]University Joseph Fourier - Grenoble I / CNRS / OSUG, LGCA, Grenoble, France.

Abstract. Interfaces between contacting rocks of the Earth's crust are shown to be unstable, corrugating, and develop roughness at various scales when submitted to non-hydrostatic stress. This instability may occur in various geological settings as long as a coherent deformation of the interface is allowed and the bodies that the interface separates have different material properties (i.e. viscosity, density, or elastic moduli). Relevant examples include fault planes, dissolution interfaces, or grain boundaries. Performing a two-dimensional linear stability analysis, we consider two cases: one solid in contact with a viscous layer and two solids separated by a thin viscous layer. In both cases either shear and/or normal loads are imposed on the interface and thermodynamical conditions for the initiation of roughening are established. Applied on several geological patterns (grain contacts, stylolites, fault planes), we propose that our analysis can explain how complex patterns may emerge at rock-rock interfaces. Finally, we provide an analysis of the evolution of the static friction coefficient along sheared interfaces. The evolution is shown to depend solely on Poisson's ratio of the solid and the ratio of the shear and normal stresses along the interface.

Appendix D

Paper IV

Kolmogorov scaling from random force fields

Europhysics Letters 84 *(2008)*

A Letters Journal Exploring the Frontiers of Physics

October 2008

EPL, **84** (2008) 10011 www.epljournal.org
doi: 10.1209/0295-5075/84/10011

Kolmogorov scaling from random force fields

M. H. Jensen[1(a)], K. Sneppen[1(b)] and L. Angheluta[2(c)]

[1] *Niels Bohr Institute - Blegdamsvej 17, Dk 2100, Copenhagen, Denmark, EU*[(d)]
[2] *Center for Physics of Geological Processes, University of Oslo - Oslo, Norway*

received 11 April 2008; accepted in final form 25 August 2008
published online 24 September 2008

PACS 05.20.Jj – Statistical mechanics of classical fluids
PACS 05.40.-a – Fluctuation phenomena, random processes, noise, and Brownian motion
PACS 47.27.-i – Turbulent flows

Abstract – We show that the classical Kolmogorov and Richardson scaling laws in fully developed turbulence are consistent with a random Gaussian force field. Numerical simulations of a shell model for turbulence suggest that the fluctuations in the force (acceleration) field are scale independent throughout the inertial regime. We find that Lagrangian statistics of the relative velocity in a turbulent flow is determined by the typical force field, whereas the multiscaling is associated to extreme events in the force field fluctuations.

In studies of fully developed turbulence, two discoveries are highly noticeable as fundamental and seminal. One regards Richardson's study of the enhanced dispersion of particles advected by a turbulent flow [1]. The other result is Kolmogorov's fundamental derivation, essentially based on dimensional arguments, of the energy spectrum in fully developed turbulence [2]. Both theories employ the energy cascade, from the integral scale down to the dissipation scale, as the paradigmatic physical picture of the energy dissipation flow. Indeed, pair-particles passively advected by turbulence exhibit a superdiffusive behavior with their relative distance given by Richardson's scaling as observed both experimentally [3], analytically [4], and in direct numerical simulations [5,6]. In the velocity space no superdiffusive behavior is needed to substantiate superdiffusion in real space.

In this letter, we show that the velocity increments generated by a white-noise force field are sufficient to generate the superdiffusive behavior, as well as the Kolmogorov energy spectrum. To put it in very simple terms: integrating "up" from the random acceleration field to the velocity field and subsequently to the displacement is enough to reproduce the well-known scaling laws.

To clarify the underlying physical picture, we consider a simple stochastic model of relative dispersion in a white-noise acceleration field given by

$$\frac{\mathrm{d}\Delta v}{\mathrm{d}t} = \Delta F(t), \tag{1}$$

$$\langle \Delta F(t')\Delta F(t'')\rangle = 6\epsilon^*\,\delta(t'-t''), \tag{2}$$

where $\Delta v(t) = v_1(t) - v_2(t)$ is the velocity difference between the two particles moving along the two trajectories $r_1(t)$ and $r_2(t)$, and $\Delta F(t) = F_1(t) - F_2(t)$ is the relative force. The prefactor 6 instead of the usual factor 2 appearing in the force correlation is due to the parametrization of the relative dispersion in terms of the diffusion constant ϵ^* for a single particle in the velocity space. The δ-function may have, in principle, a finite width given by the time correlation of the relative random field along the two trajectories. This width will be determined both by the time it takes to pass a correlation length for a given force realization, and the time it takes to change the force in a certain point of the system.

In this set up, the relative velocity field, $\Delta v(t) = \int_0^t \Delta F(s)\mathrm{d}s$, is a Wiener process with a Gaussian distribution, which leads to

$$\begin{aligned}\langle \Delta v(t_1)\Delta v(t_2)\rangle &= \int_0^{t_1}\int_0^{t_2}\langle \Delta F(t')\Delta F(t'')\rangle \mathrm{d}t'\mathrm{d}t'' \\ &= 6\epsilon^*\int_0^{t_1}\int_0^{t_2}\delta(t'-t'')\mathrm{d}t'\mathrm{d}t'' \\ &= 6\epsilon^*\int_0^{\min(t_1,t_2)}\mathrm{d}t' \\ &= 6\epsilon^*\min(t_1,t_2),\end{aligned} \tag{3}$$

(a) E-mail: mhjensen@nbi.dk
(b) E-mail: sneppen@nbi.dk
(c) E-mail: luiza.angheluta@fys.uio.no
(d) URL: http://cmol.nbi.dk.

implying that the mean square velocity difference is

$$\langle \Delta v^2(t) \rangle = 6\epsilon^* t. \tag{4}$$

The relative separation is described by a non-Gaussian distribution with the second moment satisfying Richardson's scaling, that is

$$\begin{aligned} \langle \Delta r^2(t) \rangle &= \int_0^t \int_0^t \langle \Delta v(t_1) \Delta v(t_2) \rangle \mathrm{d}t_1 \mathrm{d}t_2 \\ &= 6\epsilon^* \int_0^t \int_0^t \min(t_1, t_2) \mathrm{d}t_1 \mathrm{d}t_2 \\ &= 12\epsilon^* \int_0^t \int_0^{t_2} t_1 \mathrm{d}t_1 \mathrm{d}t_2 \\ &= 2\epsilon^* t^3. \end{aligned} \tag{5}$$

By eliminating the time dependence of the relative velocity and distance, we obtain the exact Kolmogorov scaling,

$$\langle \Delta v^2(t) \rangle = 2^{2/3} 3 \epsilon^{*2/3} \langle \Delta r^2(t) \rangle^{1/3}, \tag{6}$$

in the Lagrangian framework (for the higher moments see footnote [1]). Thus, Kolmogorov scaling is consistent with the assumption that the dispersion is driven by sufficiently random and uncorrelated acceleration fields.

In deriving eq. (6) we assumed that the relative velocity is obtained by following the Lagrangian trajectories, which in a real turbulent flow may differ from the typical velocity increments separated by the distance r (Eulerian measurement of the velocity differences) [7]. Many other stochastic models for relative dispersion have been proposed in the literature. Several of these models were based on Markov processes with some functional assumptions of the velocity profiles [8–12]. Other models were based on Langevin dynamics to various approximations of the Navier-Stokes equations [13].

Equation (4) implies that $2\epsilon^*$ is the diffusion constant for the relative velocity. For a Lagrangian stochastic flow generated by the white-noise acceleration field, ϵ^* can be estimated as

$$\begin{aligned} \langle \Delta \vec{v}(t) \Delta \vec{F}(t) \rangle &= \left\langle \int_0^t \mathrm{d}s \Delta \vec{F}(s) \cdot \Delta \vec{F}(t) \right\rangle \\ &= \int_0^t \mathrm{d}s \langle \Delta \vec{F}(s) \cdot \Delta \vec{F}(t) \rangle \\ &= 6\epsilon^* \int_0^t \delta(t-s) \mathrm{d}s = 6\epsilon^*. \end{aligned} \tag{7}$$

From dimensional considerations, ϵ^* has the same units [length^2/time^3] as the standard energy dissipation rate ϵ characterizing the turbulence cascade.

To examine how the Lagrangian white-noise acceleration relates to the anomalous scaling laws in a more realistic turbulent field, we consider the kinematics of pair particles advected by the homogeneous turbulent flow obtained by a real-space transformation of the GOY shell model [14,15]. This model proposed originally by Gledzer, Yamada and Ohkitani [16,17] provides a description of the turbulent motion embodied in the Navier-Stokes equations. The GOY model is formulated on a N-discrete set of wave numbers, $k_n = 2^n$, with the associated Fourier modes u_n evolving according to

$$\begin{aligned} \left(\frac{\mathrm{d}}{\mathrm{d}t} + \nu k_n^2 \right) u_n &= i\, k_n \Big(a_n u_{n+1}^* u_{n+2}^* + \frac{b_n}{2} u_{n-1}^* u_{n+1}^* \\ &\quad + \frac{c_n}{4} u_{n-1}^* u_{n-2}^* \Big) + f \delta_{n,1}, \end{aligned} \tag{8}$$

for $n = 1 \cdots N$. The coefficients of the non-linear terms are constrained by two conservation laws, namely the total energy, $E = \sum_n |u_n|^2$, and the helicity (for 3-D), $H = \sum_n (-1)^n k_n |u_n|$, or the enstrophy (for 2-D), $Z = \sum_n k_n^2 |u_n|^2$, in the inviscid limit, *i.e.* $f = \nu = 0$ [18]. Therefore, they may be expressed in terms of a free parameter only $\delta \in [0, 2]$, $a_n = 1$, $b_{n+1} = -\delta$, $c_{n+2} = -(1-\delta)$. As observed by Kadanoff [19], one obtains the canonical value $\delta = 1/2$, when the 3d-helicity is conserved. The set (8) of N-coupled ordinary differential equations can be numerically integrated by standard techniques [20]. We have used standard parameters in this paper $N = 19$, $\nu = 10^{-6}$, $k_0 = 2 \cdot 10^{-4}$, $f = 5 \cdot 10^{-3}$.

The GOY model is defined in k-space but we study particle dispersion in direct space obtained by an inverse Fourier transform [14] of the form

$$\vec{v}(\vec{r}, t) = \sum_{n=1}^{N} \vec{c}_n [u_n(t) e^{i \vec{k}_n \cdot \vec{r}} + \text{c.c.}]. \tag{9}$$

Here the wave vectors are $\vec{k}_n = k_n \vec{e}_n$ where $\vec{e}_n$ is a unit vector in a random direction, for each shell n and $\vec{c}_n$ are unit vectors in random directions. We ensure that the velocity field is incompressible, $\nabla \cdot \vec{v} = 0$, by constraining $\vec{c}_n \cdot \vec{e}_n = 0, \forall n$. In our numerical computations we consider the vectors $\vec{c}_n$ and $\vec{e}_n$ quenched in time but averaged over many different realizations of these.

As an example of the motion in this field, fig. 1 shows the trajectories of two passively advected particles. As the relative distance diverges in time, the two particles experience different force fields, which in turn typically increase the difference in the relative velocities of the two particles. The figure shows the individual particles as they are advected, first together and later diverging away from each other when they are encased in different eddies.

Figure 2 examines the noise in the effective force field $\langle \Delta F \Delta F \rangle$ for the relative motion of the two advected particles. In fig. 2 we use viscosity $\nu = 10^{-6}$, with a Kolmogorov scale $\Delta r \sim 1.0 \cdot 10^{-4}$. The noise amplitude is plotted *vs.* the average square distance between the particles $\langle \Delta r^2 \rangle = \langle (\mathbf{r}_1(t) - \mathbf{r}_2(t))^2 \rangle$, with the time as parametrization of the curves, as in eq. (6). The average is over independent trials of the two advected particles. One observes that both the

[1] Using Wick's theorem we obtain the $2n$-th moment of the velocity difference at time t: $\langle \Delta v^{2n}(t) \rangle = \frac{(2n)!}{2^n n!} (48\epsilon^{*2})^{n/3} \langle \Delta r^2(t) \rangle^{n/3}$.

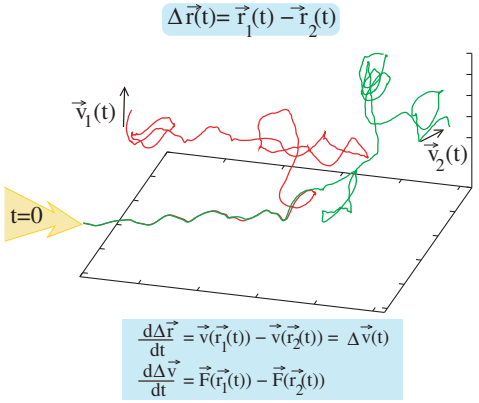

Fig. 1: Two particles being advected in a random force field, generated by the GOY shell model.

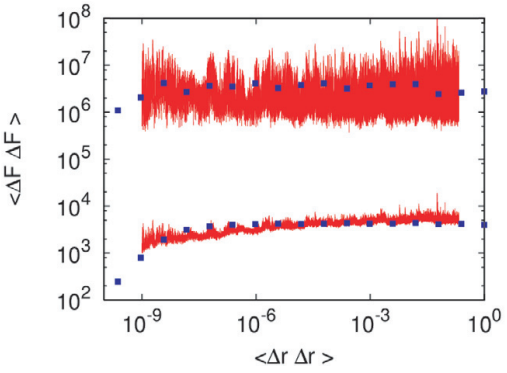

Fig. 2: The squared relative acceleration $\Delta F \Delta F$ and its infinite moment versus Δr^2. The thin lines are for the Lagrangian trajectories where distances and accelerations are parameterized by the time of advection. The squares represent the corresponding Eulerian measures of the same quantities.

typical value of the squared noise and its infinite moment ($\max_t\{\Delta F \Delta F\}$) at any distance is constant throughout the inertial range, *i.e.* above the Kolmogorov scale.

We conclude that the force field is equivalent to Gaussian white noise, and therefore the structure function of this turbulent field should be close to the one predicted by eq. (6). This is confirmed in fig. 3 where we show the deviations in velocity as a function of the square distance between the particles, that is the plot is parametrized through the time t as indicated in eq. (6). One indeed sees that $\langle \Delta v^2(t) \rangle$ *vs.* $\langle \Delta r^2(t) \rangle$ scales with an exponent close to 1/3 in agreement with our expectations. Concerning the Richardson scaling law eq. (6), we observe in the GOY simulations a long Batchelor regime ($\langle \Delta v^2(t) \rangle \sim t^2$) before it reaches the Richardson law in agreement with recent experimental

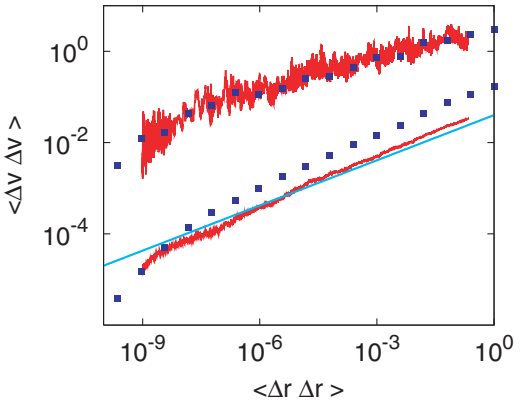

Fig. 3: The squared relative velocity $(\Delta v)^2$ and its infinite moment $(\max_t\{\Delta v^2(t)\})$ *vs.* $(\Delta r)^2$ (*i.e.* a representation of the structure function). The thin lines are for the Lagrangian trajectories where distances and velocities are parametrized by the time of advection. The filled squares represent are the corresponding Eulerian measures. The straight line represents standard Kolmogorov scaling $\langle \Delta v^2 \rangle \propto \langle \Delta r^2 \rangle^{1/3}$.

observations [21]. To study pair particle dispersion, we thus advocate to perform the scaling plot eq. (6) with time as parameter and believe this is why we observe similar behavior for both Lagrangian and Eulerian measurements. For completeness, we in fig. 3 also show the infinite moment of the velocity, and remark that this higher moment scales with an exponent close to 0.23. This signals multidiffusion [22] where extreme velocity differences sometimes, but rarely, are reached after short separations. In the current context, we see these extreme deviations as a measure of very unlikely and intermittent events which only add little to the typical behavior of the flow. Indeed also the Eulerian statistics shows clear multiscaling as expected [14].

While our intuition has been based on the Lagrangian picture of advected particles, it is interesting that the corresponding Eulerian quantities behave similarly. This is demonstrated in simulations where we now fix the distance between two points, and then calculate, respectively, the difference in velocity and acceleration. The squares in figs. 2 and 3 show how $\langle \Delta F^2(r) \rangle$ and $\langle \Delta v^2(r) \rangle$ vary with the square relative distance between the investigated points. From fig. 2 we see that the value of the plateau for the random force field is a direct consequence of its random expectation at any large distance. Therefore, there is nothing special about the selection of advected points in the Lagrangian case. In fact the onset of the plateau is slightly sharper in the Eulerian case, presumably reflecting averaging associated to the underlying time parameter in the Lagrangian advection. Similarly, there is no significant difference for the structure functions shown in fig. 3. That the Lagrangian and Eulerian quantities behave similarly

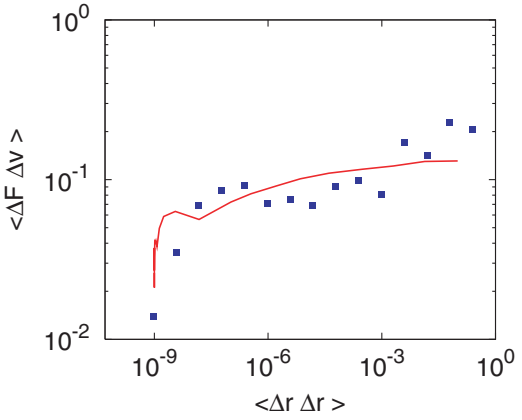

Fig. 4: A measure of an effective diffusion constant in velocity: $\langle \Delta v \Delta F \rangle$ *vs.* Δr^2. As in the previous figures the thin line describes Lagrangian trajectories parametrized by the time of advection. The filled squares correspond to the Eulerian case.

for relative velocity differences have also been observed in previous studies, see for instance [23,24].

Using eq. (7) we estimate $\langle \Delta v \Delta F \rangle \sim 0.1$ throughout the inertial range in the GOY model simulations, see fig. 4. This value of the effective velocity diffusion constant is larger than the average energy dissipation at the Kolmogorov scale, estimated from the energy input $\mathrm{Re}\langle u_1^* \cdot f \rangle = 0.001$ in the GOY model. This discrepancy in the effective diffusion terms we attribute to the huge contributions from the maybe unrealistically huge spikes in the acceleration of the GOY model. Spikes which of course are absent in the simple white noise calculation of eq. (7). These spikes also gives rise to multidiffusion, as discussed above.

We believe that the acceleration field as shown in fig. 2 should be experimentally accessible either by particle tracking in a 3-D flow [25,26] or from probe measurements in channel flows employing the Taylor hypothesis. In the first case the acceleration is easily estimated from the temporal variations in the velocity field of the 3-D advected particles. In fact [25] investigated fluctuations in single path accelerations, which were found to be larger than Gaussian expectations. More interestingly, in relation to our work, [25] also reports accelerations that are independent of the Reynolds number, resembling our findings of an acceleration difference that is independent of scale.

Overall we have seen that the variance of the force field reaches an average value that is independent of the distance between the advected points in the turbulent fluid. Already at distances slightly above the Kolmogorov scale the two particles often receive random "kicks" which are as large at small scales as they are at the integral scale. Thus, huge accelerations are associated to the very small scales, presumably to the core of eddies at the verge of their destruction by dissipation. The acceleration between two particles is primarily dependent on how close each of them are to the center of an eddy. Since accelerations are largest at the core of eddies, the relative acceleration will be dominated by the one particle that circles fastest around its eddy [27].

When examining the distribution of the accelerations at a fixed distance, the GOY shell model simulations predict a broad power law like behavior with a cutoff which is independent of the distance (as demonstrated by the constant max norm). The size of the cutoff is determined by the size of the forcing and the scale at which this foricing is acting (in our simulations, the scale is $\Delta r = 1$). In experiments the single particle acceleration has broad tails, characterized by a stretched exponential [25]. Thus already the fat tails are narrower than a power law and thus also much narrower than the GOY model results. Thus a Gaussian assumption is fairly reasonable, with limitations only imposed by time correlations. The extreme events in the tails of the single particle acceleration are presumably correlated [25], reflecting fast circulation around the core of a vortex as seen in DNS simulation [27]. In that case the repeated circulation of large accelerations contribute less to the velocity drift than a non-correlated acceleration of same magnitude would do. Also the effective ϵ^* would be lower than the one deduced directly from the width of the single-particle acceleration distribution measured in [25]. In real turbulence, the trapping of particles in vortex cores becomes less important with increasing Reynolds number [28], in which case ϵ^* estimated from eq. (7) would be close to the effective diffusion constant for the velocity field.

In conclusion, the motion associated with the relatively slow turn-over dynamics of the large eddies is not needed for obtaining Richardson or Kolmogorov statistics. These two seminal laws can be deduced from the simple assumption of a random force field that fluctuates with an amplitude set by the system size and with a correlation time set by the Kolmogorov scale. Obviously these assumptions are not realistic, but to some extent the fat tails and time correlations are coupled in a way that reduces the effect of both on the velocity dispersion. However, correlations can definitely have other effects on the space time structure of the overall flow as demonstrated by the multifractal models [29]. Our objectives have been to demonstrate that the motion of two particles in a turbulent motion can be captured by simple assumptions of an effectively random force field.

* * *

We are grateful to E. Bodenschatz, H. Nakanishi, S. Pigolotti and Y. Pomeau for valuable discussions. We thank the Danish National Research Foundation for support through the Center for Models of Life.

REFERENCES

[1] Richardson L. F., *Proc. R. Soc. London, Ser. A*, **110** (1926) 709.
[2] Kolmogorov A. N., *C. R. Acad. Sci. USSR*, **30** (1941) 301; **32** (1941) 16.
[3] Berg J., Lüthi B., Mann J. and Ott S., *Phys. Rev. E*, **74** (2006) 016304.
[4] Falkovich G., Gawedzki K. and Vergassola M., *Rev. Mod. Phys.*, **73** (2001) 1.
[5] Boffetta G. and Sokolov I. M., *Phys. Fluids*, **14** (2002) 9.
[6] Boffetta G. and Sokolov I. M., *Phys. Rev. Lett.*, **88** (2002) 9.
[7] Mordant N., Delour J., Léveque E., Michel O., Arnéodo A. and Pinton J.-F., *J. Stat. Phys.*, **113** (2003) 5/6.
[8] Durbin P. A., *J. Fluid Mech.*, **100** (1980) 279.
[9] Thomson D. J., *J. Fluid Mech.*, **210** (1990) 113.
[10] Borgas M. S. and Sawford B. L., *J. Fluid Mech.*, **279** (1994) 69.
[11] Pedrizzetti G. and Novikov E. A., *J. Fluid Mech.*, **280** (1994) 69.
[12] Borgas M. S. and Yeung P. K., *J. Fluid Mech.*, **503** (2004) 125.
[13] Heppe B. M. O., *J. Fluid Mech.*, **357** (1998) 167.
[14] Jensen M. H., *Phys. Rev. Lett.*, **83** (1999) 76.
[15] Bohr T., Jensen M. H., Paladin G. and Vulpiani A., *Dynamical Systems Approach to Turbulence* (Cambridge University Press, Cambridge) 1998.
[16] Gledzer E. B., *Sov. Phys. Dokl.*, **18** (1973) 216.
[17] Yamada M. and Ohkitani K., *J. Phys. Soc. Jpn.*, **56** (1987) 4210; *Prog. Theor. Phys.*, **79** (1988) 1265.
[18] Biferale L. and Kerr R. M., *Phys. Rev. E*, **52** (1995) 6.
[19] Kadanoff L., Lohse D., Wang J. and Benzi R., *Phys. Fluids*, **7** (1995) 617.
[20] Pisarenko D., Biferale L., Courvoisier D., Frisch U. and Vergassola M., *Phys. Fluids A*, **5** (1993) 10.
[21] Bourgoin M., Ouellette N. T., Xu H., Berg J. and Bodenschatz E., *Science*, **311** (2006) 835.
[22] Sneppen K. and Jensen M. H., *Phys. Rev. E*, **49** (1994) 919.
[23] Nicolleau F. and Vassilicos J. C., *Phys. Rev. Lett.*, **90** (2003) 024503.
[24] Nicolleau F. and Yu G., *Phys. Fluids*, **16** (2004) 2309.
[25] La Porta A., Voth G. A., Crawford A. M., Alexander J. and Bodenschatz E., *Nature*, **409** (2001) 1017.
[26] Lüthi B., Berg J., Ott S. and Mann J., *Phys. Fluids*, **19** (2007) 045110.
[27] Toschi F., Biferale L., Boffetta G., Celani A., Devenish B. J. and Lanotte A., *J. Turb.*, **6** (2005) N15; Biferale L., Boffetta G., Celani A., Lanotte A. and Toschi F., *Phys. Fluids*, **17** (2005) 021701.
[28] Yeung P. K., Pope S. B., Kurth E. A. and Lamorgese A. G., *J. Fluid Mech.*, **582** (2007) 399.
[29] Arnèodo A. *et al.*, *Phys. Rev. Lett.*, **100** (2008) 254504.